Preparation and investigation of intrinsic electronic and optical properties of individual structure-identified nanostructures: double-wall carbon nanotubes and two-dimensional atomic layers

（単一ナノ物質の作製と構造・物性評価：二層カーボンナノチューブおよび原子層物質）

A dissertation presented

by

Sihan Zhao

to

Department of Chemistry

in partial fulfillment of the requirements
for the degree of
Doctor of Philosophy

Nagoya University

November 2015

Preparation and investigation of intrinsic electronic and optical properties of

individual structure-identified nanostructures: double-wall carbon nanotubes

and two-dimensionale atomic layers

<u>Abstract</u>

Ever since the exciting discoveries of Buckyballs (C_{60} fullerene) and carbon nanotubes (CNTs) in the 1980s and 1990s, the study of nanomaterials and nanoscience has been attracting considerable research interest in the field of material science. In 2004, researchers at the University of Manchester successfully isolated the first one-atom-thick two-dimensional (2D) material, graphene, which opened new avenues of extensive research on the properties of 2D materials.

In this dissertation, I will provide a very general introduction to nanomaterials by presenting some representative examples while emphasizing on the intriguing and unique properties of those materials that are qualitatively distinct from conventional three-dimensional (3D) materials. The nanomaterials that will be discussed in this dissertation include one-dimensional (1D) CNTs, 2D graphene, and 2D layered transition metal dichalcogenides (TMDCs). The properties of nanomaterials are sensitive to the specific physical structures and environments. Consequently, to investigate the intrinsic physical and chemical properties, it is essential to prepare discrete nanomaterials with well-defined structures while simultaneously controlling the environment.

In order to understand the properties of nanomaterials more thoroughly, I have been working on the preparation of individual nanostructures (*e.g.*, CNTs, TMDCs) and probing the fundamental relationship between structure and function. The elucidation of one-to-one structure–property correlations enables us to more clearly understand the fundamental underlying mechanisms that lead to the unique properties. Here, I will present the details of my primary research results from the past several years in the following chapters: Probing the

effect of van der Waals interaction on the electronic structures in individually suspended double-wall carbon nanotubes, direct growth on hexagonal boron nitride (hBN), optical identification and transport properties of 2D layered metallic TMDCs (NbS_2). Finally, an introduction and progress report of my ongoing research project will be briefly described.

Acknowledgements

First and foremost, I would like to give my sincerest thanks to Prof. Hisanori Shinohara, who is my supervisor from the past five years, as well as a very distinguished researcher in the community of nanocarbons. I am very much indebted to him for offering me a chance studying in Department of Chemistry in Nagoya University since late 2010. I benefited greatly from his instruction on my research progress, as well as on life experiences for future development.

I would like to show my greatest gratitude to Assoc. Prof. Ryo Kitaura for his five-year consecutive instructions on my research work and cultivations on my research characters. I have been making big progress in my research capability and knowledge level thanks to his consistently patient instructions and strict treatment. I respect his exceptionally high-level knowledge and research abilities. I admire his incredible passion and love for researches. I enjoyed and will always cherish the wonderful teamwork that we have done and student–professor colleagueship that we have created.

I am also very much grateful to Prof. Kazunari Matsuda (Kyoto Univ.), Assoc. Prof. Yuhei Miyauchi (Kyoto Univ.), and Prof. Shigeo Maruyama (Tokyo Univ.) for their instructions, encouragements and friendship.

I would like to thank all the people in Shinohara' group from the past five years for their help and kindness. I also would like to thank all the office staffs in Nagoya University who have kindly offered me help and smiles. I would like to thank all the Chinese members who have worked and studied in Shinohara's group: Dr. J. Zhang, Dr. Z. Wang, Dr. Y. Sun, Chen Zhao, Dr. Q. Wang, and Dr. H. E. Lim. I will never forget the every wonderful moments living in Nagoya and in Japan from the past five years, which has been a pivot time for my future life development.

Special thanks to the JSPS fellowship and IGER program for the financial support that

covers my daily expense in Japan, as well as offers me opportunities for attending many international conferences abroad.

Last but not least, it would not have been able to successfully complete my five-year study, without getting support from my families. Thanks to my mum, my dad, my twin brother, and many other family members. You are the ones for whom I have been fighting.

Glossary of terms

3D	three-dimensional
2D	two-dimensional
1D	one-dimensional
0D	zero-dimensional
CNTs	carbon nanotubes
SWCNTs	single-wall carbon nanotubes
DWCNTs	double-wall carbon nanotubes
TMDCs	transition metal dichalcogenides
hBN	hexagonal boron nitride
CVD	chemical vapor deposition
MBE	molecular-beam epitaxy
LL	Luttinger-liquid
SC	superconductivity
CDW	charge-density-wave
DOF	degree of freedom
BZ	Brillouin zone
DOS	density of states
TRS	time reversal symmetry
E_F	Fermi level
CT excitons	charge transfer excitons
VHE	valley-Hall effect
e–e	electron–electron
e–ph	electron–phonon
e–h	electron–hole
AFM	atomic force microscopy
SEM	scanning electron microscopy
TEM	transmission electron microscopy
XPS	X-ray photoelectron spectroscopy
EELS	electron energy loss spectroscopy
SAD	selected area diffraction
CW	continuous wave
EBL	electron beam lithography

Epigraphs

"The first principle is that you must not fool yourself and you are the easiest person to fool."

"Poets say science takes away from the beauty of the stars - mere globs of gas atoms. I, too, can see the stars on a desert night, and feel them. But do I see less or more?"

Richard P. Feynman (an American theoretical physicist in fields of particle physics, quantum electrodynamics, *etc.* who is hailed as the father of nanoscience; winner of Nobel Prize in Physics in 1965)

"Doing what others have not done demands a great deal of motivation."

Sumio Iijima (a Japanese physicist and microscopist who pioneered the discovery and understanding of carbon nanotubes; winner of Kavli Prize in 2008)

Table of Contents

Chapter 1 | General introduction

1.1 Uniqueness of nanomaterials

1.1.1 Reduced size of nanomaterials

Following the exciting discoveries of Buckyballs (C_{60} fullerene) and carbon nanotubes (CNTs) in the 1980s[1] and 1990s[2], the development of nanoscience has been attracting increasing amounts of research interest. In 2004, researchers at the University of Manchester successfully isolated the first one-atom-thick two-dimensional (2D) material, graphene, opening up new
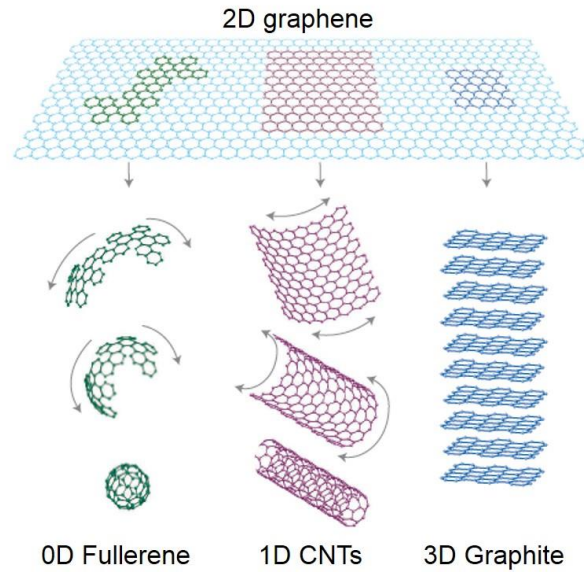
Figure 1. 2D graphene as a building block for carbon materials with other dimensions (adapted from ref. 4)

avenues of intensive research into 2D materials[3]. The sp²-bonded nanocarbon allotropes[4] (**see Figure 1**), particularly CNTs and graphene, exhibit ≈ 100 times higher carrier mobility than that of silicon (making them ≈ 100 times faster) and are believed to represent excellent electronic building blocks for the next generation of highly integrated electronics. In fact, a simple computer made of CNTs has very recently been constructed and reported by a Stanford research group[5].

What is the key factor that is responsible for the difference in the properties of nanomaterials compared with conventional bulk materials (3D)? The answer is the size or dimensions. As the size of materials gets smaller along one, two, or three directions, certain materials are reduced into 2D, 1D, and 0D materials, respectively. For example, graphene is a

typical 2D material with only one-atom thickness along the direction vertical to the basal plane, whereas CNTs and fullerene molecules are regarded as 1D and 0D materials.

1.1.2 Quantization of electronic states

One of the most obvious consequences of size confinement in nanomaterials is the quantization of electronic states, which may result in drastic changes in electronic structures, and thus the properties of the materials. One famous example is the 0D quantum dots whose properties such as optical absorption and emission wavelengths demonstrate strong dependence on size[6]. This offers a new possibility to modify the electronic and optical properties of the material by controlling the size of the dots. Another
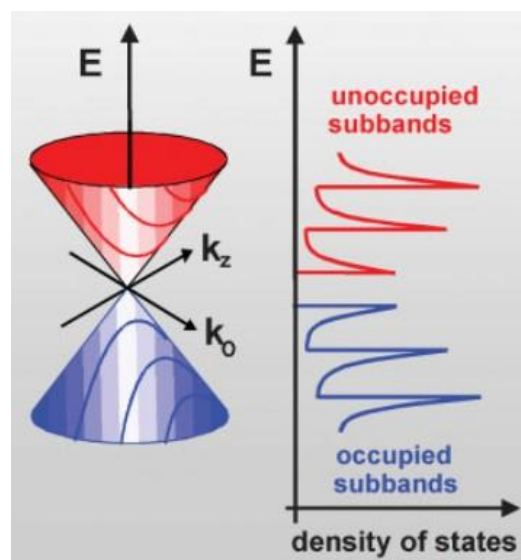
Figure 2. Schematic illustration of the quantization of electronic states in CNTs (adapted from ref. 8). The left part shows the scheme of cutting lines (allowed states) for CNTs on graphene cone-like band dispersion. The right part shows the corresponding DOS of CNTs exhibiting van Hove singularities that are unique for 1D materials.

representative example is the 1D CNTs, which can be regarded as rolled graphene sheets with seamless junctures; on account of this relation, the electronic band structure of CNTs can be well-described by discrete cutting lines on the contour of the graphene band dispersion resulting from the quantization of electronic states along the circumferential direction of tubes (**see Figure 2**)[7-8]. Depending on the dimensions, the resultant density of states (DOS), number of states at certain energy, are distinctive (**see Figure 3**); for example, the DOS in a 2D material is a step function ($\propto E$) with changing energy in contrast to that of 3D materials, where the DOS fall on a parabolic line ($\propto E^{1/2}$).
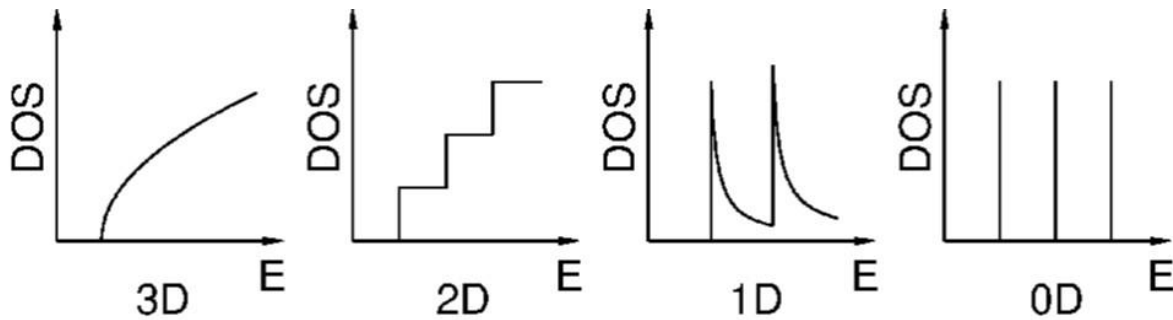
Figure 3. Typical and distinctive electronic DOS for 3D, 2D, 1D and 0D systems, respectively.

1.1.3 Enhanced many-body effects

In general, many-body effects take into account the quantum mechanical corrections of the simple one-electron quasiparticle physical picture for the description of electron motion in solids. In this description, the electrons are considered to be independent quasiparticles that experience an average electrical potential from all the other electrons. The entities that may be present in the many-body effects in solids are interactions of electron–electron (e–e) and/or electron–hole (e–h). In electronic systems with reduced dimensions, such interactions are significantly enhanced in comparison with the conventional 3D materials, resulting in the emergence of new electronic properties.

For example, in 1D systems, e–e interactions become so strong that the Fermi electron gas model, which assumes the electrons are non-interacting particles, breaks down. The new behavior of 1D electronic systems with strong e–e correlations, instead, are modeled as Tomonaga–Luttinger liquids (LL)[9-10], wherein separate charge and spin collective waves are the meaningful excitations that are induced by external stimuli. In these cases, the electron tunneling rate into LL and the conductance are suppressed to zero at zero temperature and zero voltage bias with a rise of power law in increasing temperature and voltage (**see Figure 4a**)[11]. This LL is stable at room temperature, indicating anomalous strong e–e interactions in the

systems of 1D metallic CNTs (**see figure 4b**)[12]. The e–ph interactions in 2D electronic systems are also significantly enhanced. For example, the phase transition temperature into a charge-density-wave (CDW) in the monolayer $NbSe_2$ increases from 33 K in the bulk to 145 K[13-14].
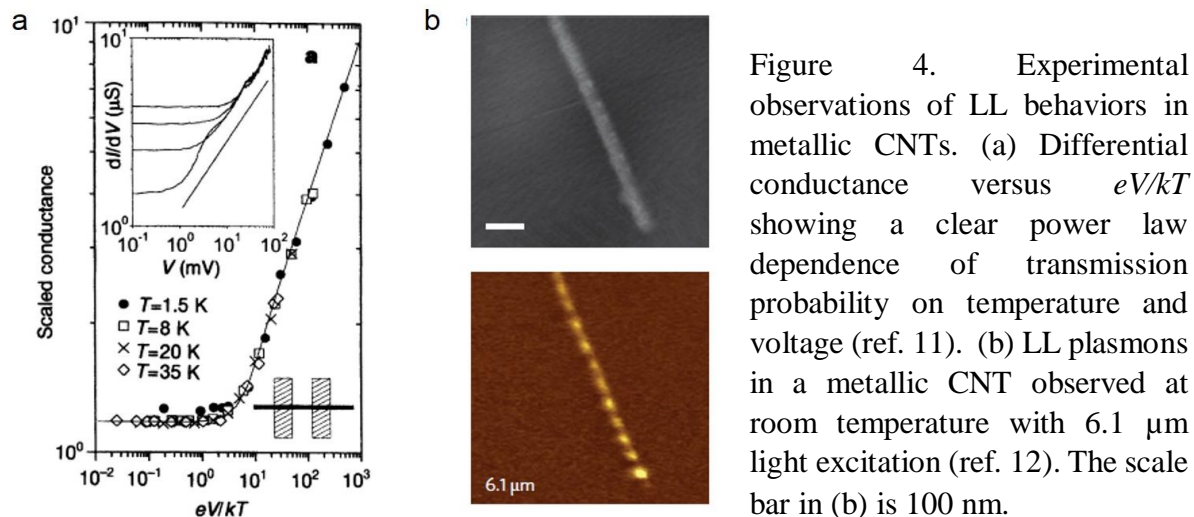
Figure 4. Experimental observations of LL behaviors in metallic CNTs. (a) Differential conductance versus *eV/kT* showing a clear power law dependence of transmission probability on temperature and voltage (ref. 11). (b) LL plasmons in a metallic CNT observed at room temperature with 6.1 μm light excitation (ref. 12). The scale bar in (b) is 100 nm.

Due to the strong Coulomb interactions in nanomaterials with a largely reduced dielectric screening effect, photo-excited charge carriers can form bound states of excitons (e–h pairs), trions (charged excitons), and bi-excitons with large binding energies E_b, resulting in a large energy change in the optical excitation compared with that of a simple one-particle bandgap excitation. Examples are 1D semiconducting CNTs (**see Figure 5**) and monolayer 2D semiconducting TMDCs, both of which have been found to have $\approx$ 0.5 eV E_b in the excitonic states[15-18], which is one order of magnitude larger than those found in conventional semiconductors such as GaAs quantum wells (tens of milli electron-volts)[19]. Metallic systems
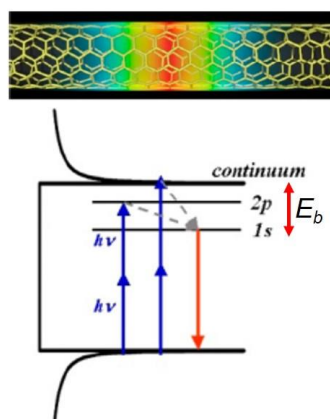
Figure 5. Bound exciton in CNTs. Two-photon absorption accesses 2p excitonic state and photoluminescence occurs from the lowest 1s state. Binding energy *Eb* is defined as the energy difference between continuum state (free electron and hole) and excitonic 1s state and estimated to be $\approx$ 0.5 eV. The figure is adapted from refs. 15 and 22.

in reduced dimensions can even form excitonic bound states[20]. Investigating and understanding

the many-body excitonic effects in nanomaterials is of significant importance for their potential

applications in optoelectronics[21-22].

1.1.4 Environmental effect and tunability
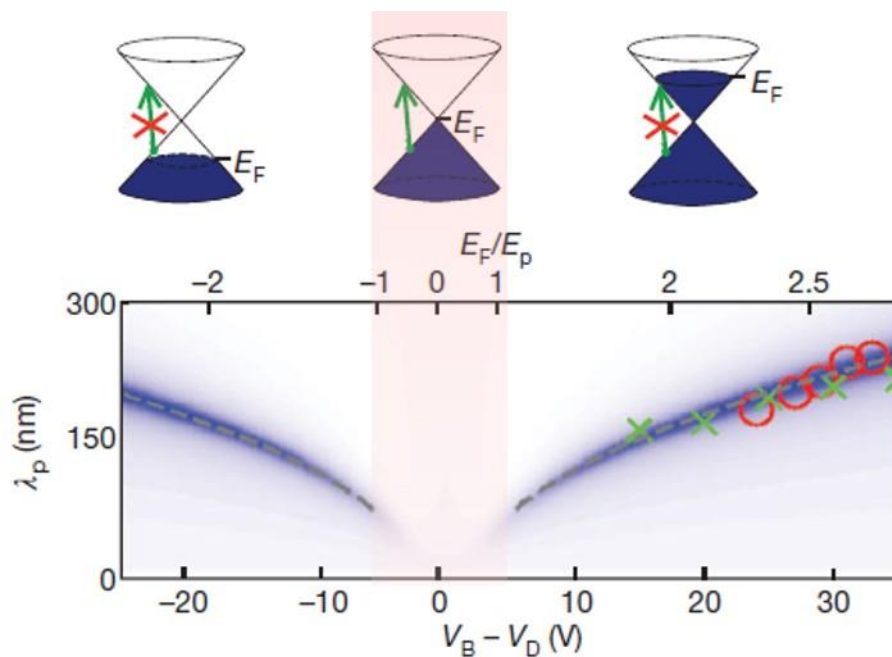
Figure 6. Switching and active control of plasmon wavelength (λ_p) in graphene nanostructures. The bottom panel shows the extracted plasmon wavelength as a function of gate voltage also as a function of Fermi energy (E_F). The upper penal shows the corresponding position of E_F in different gating conditions. When the E_F is in close vicinity of Dirac point, plasmons are damped out by the excitation of inter-band transitions, and no plasmon features were observed (red shading). As changing the E_F away from the Dirac point, the plasmons were switched on, and its wavelength can be continuously tuned. Note that the wavelength of illuminating photons is 11.06 μm which is significantly confined by more than 40 times in the graphene plasmons. The figure is adapted from ref. 25.

Nanomaterials generally demonstrate significant chemical reactivity, making them

susceptible to changes in their chemical environment. This reactivity offers an additional

method for tuning and controlling the properties of the materials, a method that is not possible

with conventional 3D materials. In nanomaterials, the external stimuli such as electric and

magnetic fields or interactions with substrates can effectively couple with all the atoms in the materials, thereby enabling greater control of the optical and electronic properties. Recently, substantial research efforts have been invested in the realization of this kind of control, which has significantly advanced the understanding of the underlying physics and development of nanotechnology.

Unlike the chemical doping that is used in 3D semiconducting materials, electrostatic gating is one of the most popular ways to precisely control the carrier densities and position of the Fermi level (E_F) in nanomaterials. This unique property of nanomaterials arises from the effectively coupled field-effect, which is largely screened out in 3D materials. Numerous research endeavors have taken advantage of
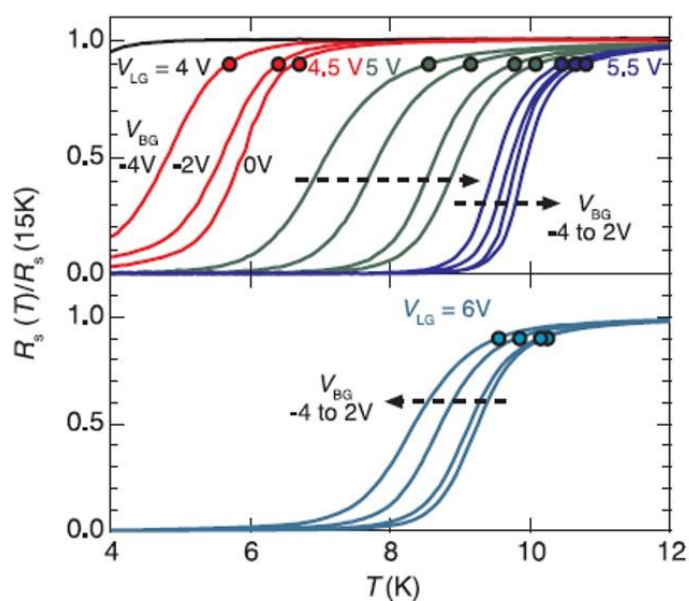
Figure 7. Gate-tunable transition temperature (T_c) of SC in few-layered MoS$_2$ (adapted from ref. 29). Two electrostatic gates are applied to tune the carrier densities and T_c: liquid gate (V_{LG}) and bottom gate (V_{BG}).

this idea to realize functional nanodevices in electronics, optics, and optoelectronics. For example, graphene has been exploited for use as 2D transparent metal contacts in place of metal leads. This application takes advantage of the ability to tune the E_F to reduce the height of the Schottky barriers by using an electrostatic gate[23-24]. The same idea was also applied to 2D graphene plasmons (**see Figure 6**), where the wavelength of a strongly confined optical field in graphene (more than 40 times smaller than the illuminated photons) was tunable by an electrostatic gate[25-26]. In monolayer MoS$_2$ or WS$_2$, the technique of electrostatic gating has been successfully applied for the effective tuning of the oscillator strength between different

bright excitonic states[27] and for the control of the emission of second harmonic generations[28]. Induced superconductivity (SC) by electrostatic doping was also demonstrated in semiconducting TMDCs like MoS_2[29] (**see Figure 7**) and WS_2[30], and the transition temperature (T_c) can be tuned by varying the amount of doping. Phase transitions such as CDW also show good gate-tunable behavior in layered metallic TMDCs[31-32].
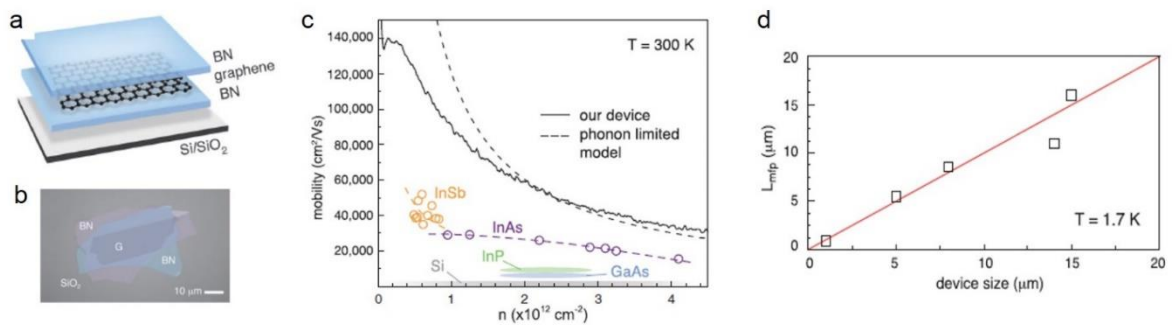
Figure 8. Mobility enhancement in graphene devices sandwiched by hBN (adapted from ref. 33). (a) Schematic of BN/Graphene/BN sandwiched structure. (b) Optical image of BN/Graphene/BN structure prior to the device process. (c) Room temperature mobility of a BN/Graphene/BN device as a function of carrier densities with comparison with various semiconductors such as Si, GaAs, *etc*. The dashed line shows the calculation results of acoustic phonon-limited carrier mobility of graphene. (d) Extracted carrier mean free path of so-prepared graphene devices with different channel lengths, which exhibits a clear ballistic transport behavior at low temperature.

The substrate effect (one of the environmental effects) can play an essential role in the properties of nanomaterials. The substrate effect has only a minor effect on conventional bulk materials, however, this effect is magnified in nanomaterials, because most of the atoms are subject to the direct influence from the substrate (except for suspended ones). As a result, the optical and electrical properties of nanomaterials are largely influenced by the coupling with underlying substrates. For example, by careful selection of good substrates and dielectric materials for

graphene[33] (**see Figure 8**) and TMDCs[34] devices, carrier mobility can be significantly increased. The mechanism of the recently discovered 2D SC and the enhanced T_c (**see Figure 9**), although not yet clear, may be associated with substrate doping and the direct coupling of substrate

phonons with electrons in the materials. This offers a new, exciting possibility to find novel

2D superconductors through the careful selection of substrate materials[35-37].
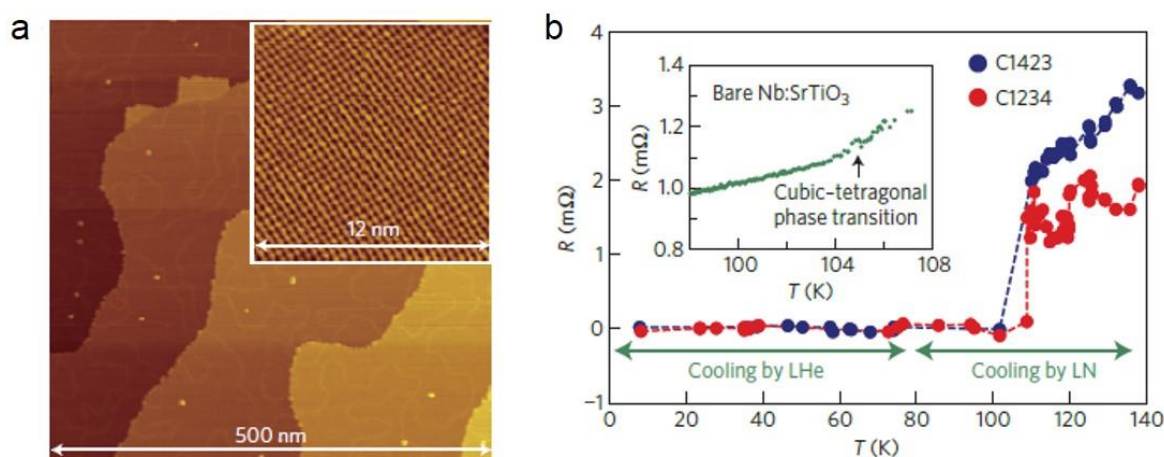
Figure 9. Superconductivity above 100 K of single-layer FeSe on doped $SrTiO_3$ substrate (adapted from ref. 36). (a) Scanning tunneling microscope (STM) image of as grown FeSe thin films on $SrTiO_3$ by molecular beam epitaxy (MBE). Inset shows a close-up view of single-layer FeSe. (b) A enhanced T_c (> 100 K) was found by a four-probe electrical measurement for a single-layer FeSe on $SrTiO_3$.

1.1.5 Importance of symmetry

The concept of symmetry plays a universal and essential role in determining the physical properties of molecules and crystalline solids; often many of the related physics can be largely, at least in a qualitative level, predicted and explained from the symmetry point of view[38]. A well-known example in nonlinear optics is the phenomenon of second harmonic generation (manifested by the doubling of a photon's frequency), which only appears in solid materials that do not have an inversion center (breaking inversion symmetry)[39]. A change in symmetry is a necessary consequence when the dimensions of materials are reduced from 3D to 2D and 1D. As a result, new and different physics may exist in nanomaterials owing to the symmetry changes.
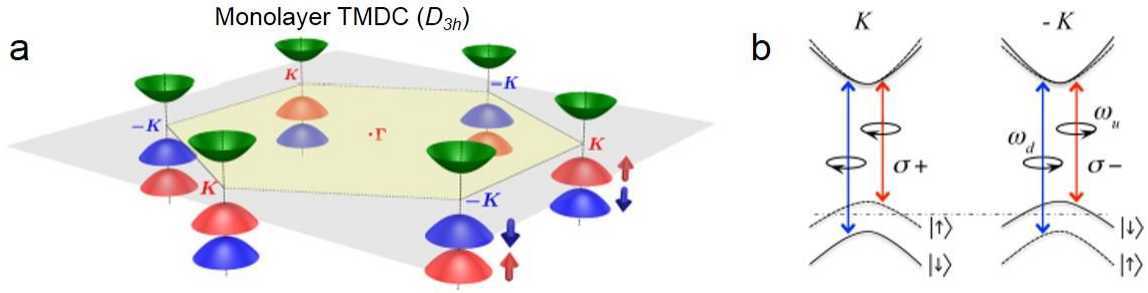
Figure 10. Schematic illustration of valley physics in monolayer TMDCs that are lacking in inversion symmetry (adapted from ref. 44). (a) Scheme of the electronic band structure of a monolayer TMDC. K and −K points at corners of the first Brillouin zone are called valleys which are energetically degenerate. States at K and −K are transformed via time reversal symmetry (TRS). Thanks to the breaking inversion symmetry in monolayers, valley-contrasting physically observable quantities such as magnetic moments, Berry curvature are finite (non-zero) at K and −K. The spin and valley states are coupled in K and −K. (b) Schematic showing the opposite optical transition rules at K and −K valleys: left-hand ($\sigma+$) circularly polarized light only couples with optical excitation and/or emission in K valley, whereas right-hand ($\sigma-$) circularly polarized light only interacts with that in −K valley.

Additionally, the symmetry (or environmental symmetry) of low-dimensional materials can be effectively modified by applying an electric or magnetic field[40-43]. All of these combined properties, in principle, can provide nanomaterials with the ability to explore new physics as well as a way to manipulate them. In the following text, I will present several representative examples to emphasize the important roles and implications of symmetry in nanomaterials that can be utilized to manipulate and control physics, from a symmetry point of view.

The symmetry point group in monolayer TMDCs (*e.g.*, MoS_2, WS_2) is *D_{3h}*, which has been reduced from *D_{6h}* in bulk (or even layer numbers); the critical difference between the monolayer and bulk is the lacking of inversion symmetry in the monolayers. As a result of this break of symmetry, in addition to the real spin and charges, a new degree of freedom (DOF) for carriers, called valley (or pseudospins) appears in these 2D electronic systems. This new DOF for carriers has contrasting physical properties in K and −K valleys such as opposite optical selection rules and opposite Berry phases or curvatures[44] (**see Figure 10**). These
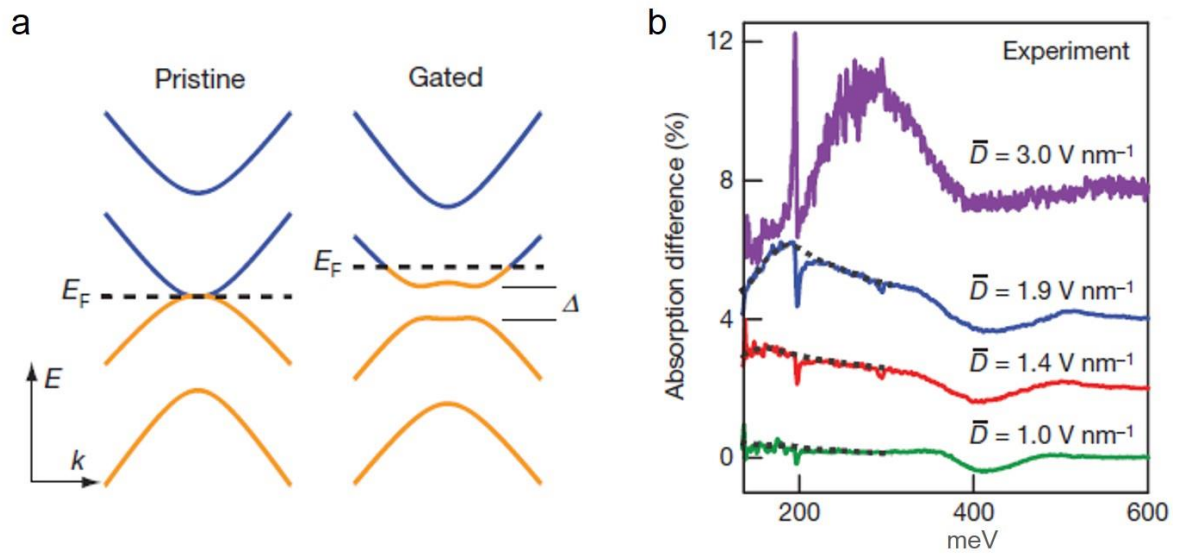
Figure 11. Bandgap opening in bilayer graphene by breaking the electric potential symmetry of the two graphene layers via a vertical electrical field (adapted from ref. 47). (a) Pristine bilayer graphene has no bandgap; however, gated by vertical electrical field, the bandgap Δ can be opened while E_F is shifted. (b) Bandgap opening in bilayer graphene under different electrical displacements that is probed by infrared optical absorption spectroscopy. As large as ~ 250 meV gap was opened at a displacement of 3.0 V nm^{-1} (purple curve).

emerging 2D materials provide a novel possibility for the study of the interplay between the DOF for carriers in individual single materials and hold a new and promising potential towards the development and realization of 2D spintronics[45-46].

Intrinsic bilayer graphene (Bernal stacking) has no bandgap due to possession of an inversion point in the middle of the two graphene layers. However, a bandgap of hundreds of milli electron-volts can be induced by breaking the electrostatic potential symmetry between the two constituent layers by applying a static electric field vertical to the bilayer planes[47-48] (**see Figure 11**). On the basis of this induced bandgap, topology-protected chiral valley currents in bilayer domain boundaries have been observed[49]. Similarly, breaking the inversion symmetry of graphene by placing it on top of hBN results in the detection of topological currents from different valleys (K and −K), without breaking time reversal symmetry (TRS)[50]. This effect can be exploited for information processing based on the valley DOF, similar to that of information holding in monolayer TMDCs.
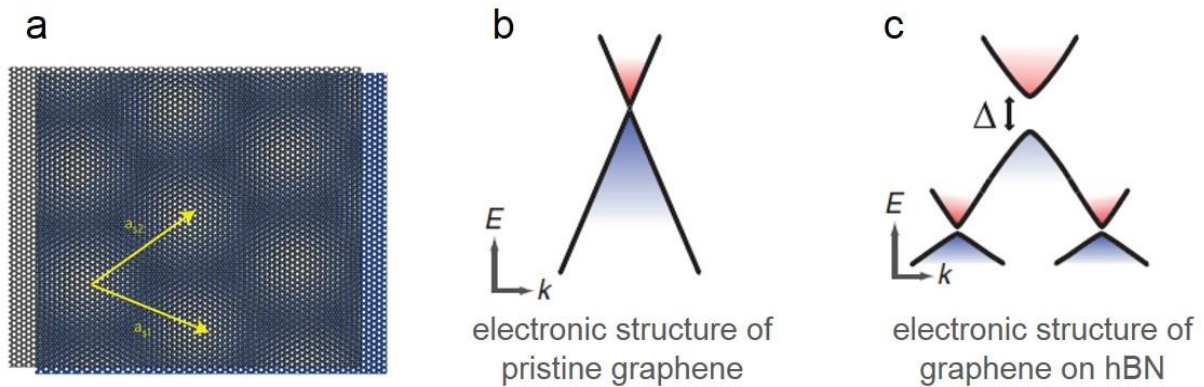
Figure 12. Bandgap engineering of graphene on hBN (adapted from ref. 52). (a) Structure model of graphene on top of hBN with a mutual twisted angle of 0°. Yellow arrows show the lattice vectors of Moiré pattern formed; length of the vectors is ≈ 14 nm which is more than 50 times longer than that of pristine graphene. One important consequence is that the symmetry of gaphene sublattice (two carbon atoms in unit cell) breaks in the graphene-hBN heterostructure. (b) Pristine band structure of graphene with zero bandgap. (c) Band structure of graphene-hBN heterostructure in which the bandgap Δ was opened due to the induced asymmetry between graphene sublattice in potential by underlying hBN. Additional cone-like features in the valence band side are due to electron scattering from the periodical Moiré potential.

Not only does the global symmetry play an essential role in determining properties, but local symmetry is also important for the determination of the physical properties of nanomaterials. For example, resulting from the very close lattice constant between graphene and hBN (only 1.8% mismatch), graphene on BN with nearly 0° rotation forms Moiré patterns with a large period (≈ 14 nm). The asymmetry between two carbon atoms inside each graphene unit cell (A–B asymmetry) is induced by the difference in potential between the underlying boron and nitrogen atoms in hBN. As a result, the bandgap in graphene is opened[51-52] (**see Figure 12**).

Artificially made van der Waals-coupled 2D heterostructures[53] also offer a unique opportunity to probe the elementary problems that were not previously accessible using bulk materials. For example, the "Hofstadter butterfly," which has been theoretically predicted in 1976 but never experimentally observed in magnetotransport due to the enormous magnetic field required[54], was recently observed in the graphene–hBN heterostructure[51-52]. The titanic

size of the graphene supperlattice ($\approx$ 14 nm) enabled the quantum flux per unit cell to easily access and extend the previous limitation (to achieve $\Phi/\Phi_0 > 1$, where Φ_0 is the magnetic flux quantum) at a moderate magnetic field, thereby leading to the first observation of the "Hofstadter butterfly."

1.2 Importance of the study of individual nanomaterials with known structures

As reviewed above, many of the unique properties of nanomaterials and their active control result from the effect of size confinement. In order to accurately define the physical structures of nanomaterials, parameters such as diameter, thickness, mutual orientation, and stacking orders need to be known. The need to understand the exact structure of nanomaterials is magnified because their synthesis frequently gives a mixture of materials with different physical structures that can exhibit distinctive properties. This has led to an enormous effort in the selective and controllable synthesis of nanomaterials[55-60], as well as in post separation and purification[61-65] to obtain a single species with a well-defined structure. However, even if synthesis of a pure nanomaterial was achieved, this would still be insufficient for the studies of the fundamental properties of nanomaterials. Individually isolated nano-objects are required to probe the intrinsic physical properties of the nano-object without the impact of interactions from other materials[66]. In the following text, I will present two examples that demonstrate the necessity and importance of investigating individual nano-objects with known structures.

As-grown, single-wall carbon nanotubes (SWCNTs) samples always contain a mixture of different species with a variety of physical structures or chiralities (n, m); the electronic band structure of SWCNTs strongly depends on the detailed chirality (n, m)[7, 67]. A SWCNT can be regarded as a single graphene sheet rolled along a vector C_h ($C_h = na_1 + ma_2$, where a_1 and a_2 are unit vectors of a 2D graphene sheet), as shown in **Figure 13a**. Depending on the direction and length (namely diameter) of C_h, tubes with different physical structures are formed, which are uniquely defined by different sets of (n, m). More importantly, the electronic states can only assume discrete values owing to the finite size of C_h. **Figure 13b** shows the corresponding BZ of graphene, where a series of parallel equidistant cutting lines represent the available states for a SWCNT with chirality (4, 2). The location of these parallel equidistant cutting lines on the graphene BZ relies on the specific chirality (n, m); as a result, the electronic band structure

of a SWCNT relies on the specified chirality (n, m). Depending on the (n, m), SWCNTs can be either metals (m-) or semiconductors (s-), and the bandgap of the semiconducting species decreases with increasing tube diameter.
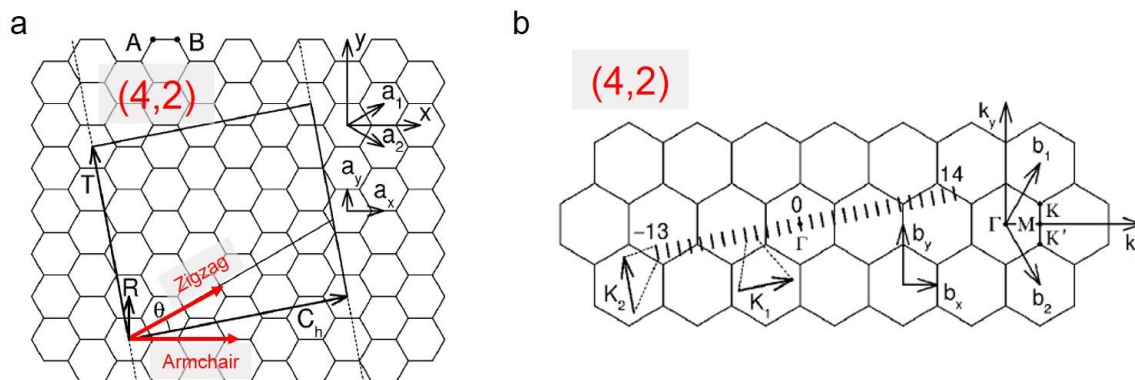
Figure 13. Definition of detailed physical structure (chirality) of a SWCNT (4,2) and the scheme of cutting lines for understanding the electronic band structure of SWCNTs (adapted from ref. 67). (a) A CNT with a chirality (4,2) is constructed by rolling a single graphene sheet along $C_h = 4a_1 + 2a_2$. The region enclosed by two vectors C_h and T is the unit cell of this CNT and θ is its chiral angle. Depending on the value of θ, so-constructed CNTs can be armchair ($\theta = 30°$), zigzag ($\theta = 0°$) and chiral tubes ($0° < \theta < 30°$). (b) Scheme of cutting lines (available states) of this (4,2) tube on graphene BZ (constructing unit vectors b_1 and b_2). K_1 and K_2 correspond to vectors of C_h and T defined in the reciprocal space. The equidistant cutting lines parallel to K_2 are the available states for the (4,2) carbon nanotube resulting from state quantization along K_1 (C_h).

Figure 14 shows a simple schematic illustrating the electronic band structure (close to E_F) and the corresponding DOS of an s-SWCNT obtained from the concept of cutting lines on graphene band dispersion. The intimate structure–property correspondence present in SWCNTs indicates that an exploration of the fundamental physical properties requires to understand wall structures at the individual tube level; else, the charity-dependent physics and underlying mechanism will be elusive because of the involvement of different distinctive species. For example, the 1D transport nature (*e.g.,* ballistic transport due to the lack of back-scatterings) could not be observed and revealed in the electrical measurement of SWCNT networks or thin films[68], compared with the individual cases[69]. The optical properties of SWCNTs were best elucidated only when looking at individual nanotubes with known structures[12,70-71].

The thickness or layer numbers of the layered 2D semiconducting (s-) TMDCs (restricting our discussion to the most common and stable 2H-phase), which are van der Waals-coupled between different constituent layers, plays an essential role in the electronic band structure, and thus in all the relevant optical and electronic properties. Both theoretical
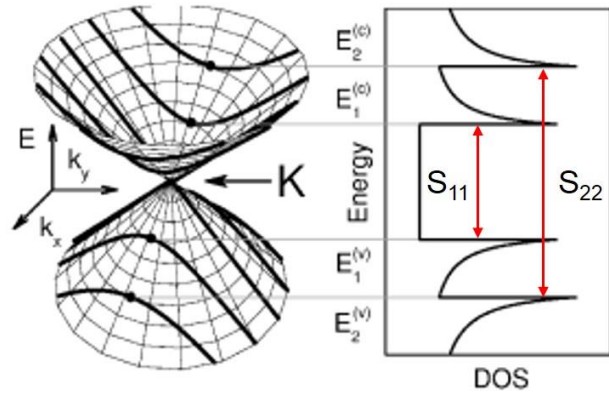
Figure 14. Schematic of electronic band structure of an s-SWCNT derived from the scheme of cutting lines on the graphene band dispersion and the corresponding DOS. Two of the dipole-allowed optical transitions donated as S_{11} and S_{22} are also shown.

calculations and experimental results (**see Figure 15**) show that monolayer s-TMDCs become direct bandgap semiconductors with a conduction band minimum and a valence band maximum at the corners (K or −K) of the first BZ, whereas samples with two or more layers possess indirect bandgaps[72-75]. Direct bandgaps lying inside the visible light range in monolayers result in great potential for their applications in optoelectronics. This has strongly driven significant research interests and effort in the development of and improvement in layer-number-controlled synthesis of 2D s-TMDCs atomic layers[76-77]. In addition to the type of bandgaps, only s-TMDCs with an odd number of layers show intrinsic valley-related physics due to break in the inversion symmetry. For example, monolayer MoS_2 samples can show selective valley optical absorption and emission, the valley-Hall effect, while no such phenomena are observed in the bilayers[78-81].
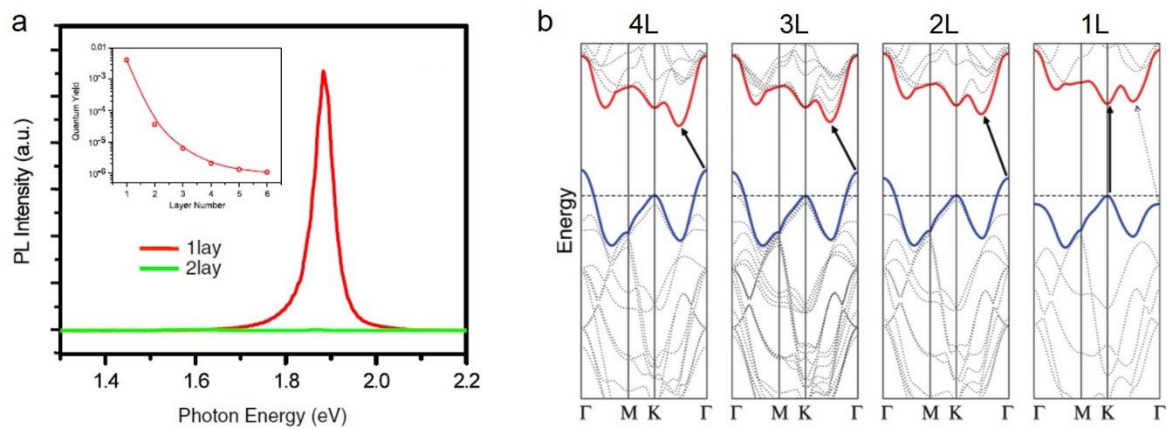
Figure 15. Direct bandgap in monolayer MoS$_2$. (a) Photoluminescence (PL) from monolayer and bilayer MoS$_2$ nanoflakes (ref. 73). PL from monolayer MoS$_2$ is very strong in contrast with bilayer 2H-MoS$_2$. Inset shows the layer-number-dependence of PL quantum yield. (b) Calculated band structure for 4L, 3L, 2L and 1L MoS$_2$ in which a transition from indirect bandgap to direct bandgap occurs as the sample thickness decreases to 1L (ref. 74).

1.3 Overview of this study

Our research interest lies in probing the intrinsic physical properties of nanomaterials with a focus on investigation of the electronic and optical properties of discrete nano-objects with defined structures.

(1) Probing the effect of van der Waals interaction on the electronic structures in double-wall carbon nanotubes (DWCNTs) (**Chapter 2**). In this project, we found out that the van der Waals interaction, which is normally considered a weak interaction, can be fairly strong such that the electronic structures of each constituent SWCNTs are changed. We directly probe this modification of electronic structures by simultaneously determining the physical structure of individual DWCNTs (chirality of each tubes) and the optical transition energies of the DWCNTs. By comparison with the optical transition energies in isolated SWCNTs with the same chirality, the degree of shifts of optical transition energies in DWCNTs are determined and used for estimating the coupling strength resulting from the van der Waals interactions between two SWCNTs. We found that most of the transitions in DWCNTs show redshifts (decreased transition energies), and the energy shifts can be as large as 0.2 eV (that is around 10% of the original transition energies) depending on the electronic types of constituent tubes. We explain these experimental observations in the context of dielectric screening. In addition, we emphasize that the effect of direct orbital coupling may also widely exist in the 1D van der Waals-coupled systems to account for the observed blue shifts and new transitions that are found in our study. Further works are definitely needed to contribute to full understanding of the physical mechanism on the issue of effect of 1D van der Waals interactions on the electronic structures.

(2) Direct growth of individual thickness-identified ultra-thin metallic TMDCs (NbS$_2$) on hBN substrates by CVD (**Chapter 3**). Owing to the enhanced e–e and/or e-ph interactions

and strong influence from the substrate effect, 2D metals are ideal platforms to study the rich physics resulting from such interplay. Novel 2D superconductors with tunable T_c may be found in new 2D metals; effective and efficient control of light−matter interaction may also be achieved by the plamons in 2D metals with expected low-loss and tunable wavelength. However, it has been remaining a challenge for the synthesis and isolation of 2D metallic layers presumably because of the strong metallic bonds between layers. By utilization of a triple-furnace CVD scheme and hBN as a growth substrate, we have successfully grown ultra-thin NbS_2 atomic layers down to the monolayer limit. We provided fundamental structural and spectroscopic characterizations on the newly-prepared 2D metallic layered system. Sample characterizations by microscopy such as AFM, TEM, SEM, as well as by spectroscopy such as Raman, XPS, EELS have been performed to show the phase purity and high crystallinity of so-prepared 2D NbS_2. Our transport data (with temperature-dependence) have confirmed the metal nature of the 2D NbS_2, which is consistent with theoretical calculations. We have demonstrated that the epitaxial growth mode is the growth mechanism of NbS_2 on hBN with a very clean interface between them. We concluded that growth substrates play an essential role in the successful growth of 2D metallic TMDCs (NbS_2) for the first time. This developed synthetic route can be generalized to the growth of other 2D metals, thereby opening up a new avenue to explore rich physics that may exist in them. We hope that this study can lead us to find novel 2D superconductors, with high T_c, by a careful selection of substrates and subsequent high-quality growth of 2D metals on top of them.

(3) I will report the recent progress of my ongoing work in **Chapter 4**.

1.4 References

1. Kroto, H. W. *et al*. C_{60}: buckminsterfullerene. *Nature* ***318,*** 162-163 (1985).

2. Iijima, S. Helical microtubules of graphitic carbon. *Nature* ***354,*** 56-58 (1991).

3. Novoselov, K. S. *et al*. Electric field effect in atomically thin carbon films. *Science* ***306,*** 666-669 (2004).

4. Geim, A. K. and Novoselov, K. S. The rise of graphene. *Nature Mater.* ***6,*** 183-191 (2007).

5. Shulaker, M.M. *et al*. Carbon nanotube computer. *Nature* ***501,*** 526-+ (2013).

6. Poznyak, S. K. *et al*. Size-dependent electrochemical behavior of thiol-capped CdTe nanocrystals in aqueous solution. *J. Phys. Chem. B* ***109,*** 1094-1100 (2005).

7. Saito, R., Dresselhaus, G., and Dresselhaus, M. S. Physical properties of carbon nanotubes. *World Scientific* (1998).

8. Burghard, M., Klauk, H., and Kern, K. Carbon-based field-effect transistors for nanoelectronics. *Adv. Mater.* ***21,*** 2586-2600 (2009).

9. Tomonaga, S. Remarks on blochs method of sound waves applied to many-fermion problems. *Prog. Theor. Phys.* ***5,*** 544-569 (1950).

10. Luttinger, J. M. An exactly soluble model of a many-fermion system. *J. Math. Phys.* ***4,*** 1154-& (1963).

11. Bockrath, M. *et al*. Luttinger-liquid behaviour in carbon nanotubes. *Nature* ***397,*** 598-601 (1999).

12. Shi, Z. W. *et al*. Observation of a Luttinger-liquid plasmon in metallic single-walled carbon nanotubes. *Nature Photon.* ***9,*** 515-519 (2015).

13. Xi, X. X. *et al*. Strongly enhanced charge-density-wave order in monolayer NbS_2. *Nature Nanotech.* doi:10.1038/nnano.2015.143

14. Calandra, M., Mazin, I.I., and Mauri, F. Effect of dimensionality on the charge-density

wave in few-layer 2H-NbSe$_2$. *Phys. Rev. B 80,* (2009).

15. Wang, F., Dukovic, G., Brus, L. E., and Heinz, T. F. The optical resonances in carbon nanotubes arise from excitons. *Science 308,* 838-841 (2005).

16. Maultzsch, J. *et al*. Exciton binding energies in carbon nanotubes from two-photon photoluminescence. *Phys. Rev. B 72,* (2005).

17. He, K. L. *et al*. Tightly bound excitons in monolayer WSe$_2$. *Phys. Rev. Lett. 113,* (2014).

18. Hill, H. M. *et al*. Observation of excitonic Rydberg states in monolayer MoS$_2$ and WS$_2$ by photoluminescence excitation spectroscopy. *Nano Lett. 15,* 2992-2997 (2015).

19. Fu, Y. and Chao, K. A. Exciton binding-energy in GaAs/Al$_x$Ga$_{1-x}$ as multiple quantum-wells. *Phys. Rev. B 43,* 12626-12629 (1991).

20. Wang, F. *et al*. Observation of excitons in one-dimensional metallic single-walled carbon nanotubes. *Phys. Rev. Lett. 99,* (2007).

21. Avouris, P., Freitag, M., and Perebeinos, V. Carbon-nanotube photonics and optoelectronics. *Nature Photon. 2,* 341-350 (2008).

22. Brus, L. Size, dimensionality, and strong electron correlation in nanoscience. *Acc. Chem. Res. 47,* 2951-2959 (2014).

23. Wang, J. I. J. *et al*. Electronic transport of encapsulated graphene and WSe2 devices fabricated by pick-up of prepatterned hBN. *Nano Lett. 15,* 1898-1903 (2015).

24. Avsar, A. *et al*. Air-stable transport in graphene-contacted, fully encapsulated ultrathin black phosphorus-based field-effect transistors. *ACS Nano 9,* 4138-4145 (2015).

25. Chen, J. N. *et al*. Optical nano-imaging of gate-tunable graphene plasmons. *Nature 487,* 77-81 (2012).

26. Fei, Z. *et al*. Gate-tuning of graphene plasmons revealed by infrared nano-imaging. *Nature 487,* 82-85 (2012).

27. Mak, K. F. *et al*. Tightly bound trions in monolayer MoS$_2$. *Nature Mater. 12,* 207-211

(2013).

28. Seyler, K. L. *et al*. Electrical control of second-harmonic generation in a WSe$_2$ monolayer transistor. *Nature Nanotech.* **10,** 407-411 (2015).

29. Ye, J. T. *et al*. Superconducting dome in a gate-tuned band insulator. *Science* **338,** 1193-1196 (2012).

30. Jo, S., Costanzo, D., Berger, H., and Morpurgo, A. F. Electrostatically induced superconductivity at the surface of WS$_2$. *Nano Lett.* **15,** 1197-1202 (2015).

31. Yu, Y. J. *et al*. Gate-tunable phase transitions in thin flakes of 1T-TaS$_2$. *Nature Nanotech.* **10,** 270-276 (2015).

32. Yoshida, M. *et al*. Controlling charge-density-wave states in nano-thick crystals of 1T-TaS$_2$. *Sci. Rep.* **4,** (2014).

33. Wang, L. *et al*. One-dimensional electrical contact to a two-dimensional material. *Science* **342,** 614-617 (2013).

34. Radisavljevic, B. et al. Single-layer MoS$_2$ transistors. *Nature Nanotech.* **6,** 147-150 (2011).

35. Zhang, T. *et al*. Superconductivity in one-atomic-layer metal films grown on Si (111). *Nature Phys.* **6,** 104-108 (2010).

36. Ge, J. F. *et al*. Superconductivity above 100 K in single-layer FeSe films on doped SrTiO$_3$. *Nature Mater.* **14,** 285-289 (2015).

37. Calandra, M., Zoccante, P., and Mauri, F. Universal increase in the superconducting critical temperature of two-dimensional semiconductors at low doping by the electron-electron interaction. *Phys. Rev. Lett.* **114,** (2015).

38. Dresselhaus, M. S., Dresselhaus, G., and Jorio, A. Group Theory: Application to the Physics of Condensed Matter. *Springer* (2008)

39. Shen, Y. R. The principles of Nonlinear Optics. *Wiley* (1984)

40. Kim, J. *et al*. Ultrafast generation of pseudo-magnetic field for valley excitons in WSe$_2$ monolayers. *Science 346,* 1205-1208 (2014).

41. Sie, E. J. *et al.* Valley-selective optical stark effect in monolayer WS$_2$. *Nature Mater. 14,* 290-294 (2015).

42. Aivazian, G. *et al.* Magnetic control of valley pseudospin in monolayer WSe$_2$. *Nature Phys. 11,* 148-152 (2015).

43. Srivastava, A. *et al.* Valley Zeeman effect in elementary optical excitations of monolayer WSe$_2$. *Nature Phys. 11,* 141-147 (2015).

44. Xiao, D. *et al.* Coupled spin and valley physics in monolayers of MoS$_2$ and other group-VI dichalcogenides. *Phys. Rev. Lett. 108,* (2012).

45. Xu, X. D., Yao, W., Xiao, D., and Heinz, T. F. Spin and pseudospins in layered transition metal dichalcogenides. *Nature Phys. 10,* 343-350 (2014).

46. Liu, G. B. *et al.* Electronic structures and theoretical modelling of two-dimensional group-VIB transition metal dichalcogenides. *Chem. Soc. Rev. 44,* 2643-2663 (2015).

47. Zhang, Y. B. *et al.* Direct observation of a widely tunable bandgap in bilayer graphene. *Nature 459,* 820-823 (2009).

48. Mak, K. F., Lui, C. H., Shan, J., and Heinz, T. F. Observation of an electric-field-induced band gap in bilayer graphene by infrared spectroscopy. *Phys. Rev. Lett. 102,* (2009).

49. Ju, L. *et al*. Topological valley transport at bilayer graphene domain walls. *Nature 520,* 650-655 (2015).

50. Gorbachev, R. V. *et al.* Detecting topological currents in graphene superlattices. *Science 346,* 448-451 (2014).

51. Ponomarenko, L. A. *et al*. Cloning of Dirac Fermions in graphene superlattices. *Nature 497,* 594-597 (2013).

52. Hunt, B. *et al.* Massive Dirac Fermions and Hofstadter butterfly in a van der Waals

heterostructure. *Science* **340,** 1427-1430 (2013).

53. Geim, A. K. and Grigorieva, I. V. van der Waals heterostructures. *Nature* **499,** 419-425 (2013).

54. Hofstadter, D. R. Energy-levels and wave-functions of Bloch electrons in rational and irrational magnetic-fields. *Phys. Rev. B* **14,** 2239-2249 (1976).

55. Wang, Z. Y. *et al*. Missing small-bandgap metallofullerenes: their isolation and electronic properties. *Angew. Chem. Int. Ed. Engl.* **52,** 11770-11774 (2013).

56. Yang, F. *et al*. Chirality-specific growth of single-walled carbon nanotubes on solid alloy catalysts. *Nature* **510,** 522-524 (2014).

57. Sanchez-Valencia, J. R. *et al*. Controlled synthesis of single-chirality carbon nanotubes. *Nature* **512,** 61-64 (2014).

58. Zhao, P. *et al*. Equilibrium chemical vapor deposition growth of Bernal-stacked bilayer graphene. *ACS Nano* **8,** 11631-11638 (2014).

59. Ji, Q. Q. *et al*. Epitaxial monolayer MoS_2 on mica with novel photoluminescence. *Nano Lett.* **13,** 3870-3877 (2013).

60. Heo, H. *et al*. Rotation-misfit-free heteroepitaxial stacking and stitching growth of hexagonal transition-metal dichalcogenide monolayers by nucleation kinetics controls. *Adv. Mater.* **27,** 3803-3810 (2015).

61. Akiyama, K. *et al*. Non-HPLC rapid separation of metallofullerenes and empty cages with $TiCl_4$ Lewis acid. *J. Am. Chem. Soc.* **134,** 9762-9767 (2012).

62. Arnold, M. S. *et al*. Sorting carbon nanotubes by electronic structure using density differentiation. *Nature Nanotech.* **1,** 60-65 (2006).

63. Tu, X. M., Manohar, S., Jagota, A., and Zheng, M. DNA sequence motifs for structure-specific recognition and separation of carbon nanotubes. *Nature* **460,** 250-253 (2009).

64. Collins, P. C., Arnold, M. S., and Avouris, P. Engineering carbon nanotubes and

nanotube circuits using electrical breakdown. *Science 292,* 706-709 (2001).

65. Jin, S. H. *et al*. Using nanoscale thermocapillary flows to create arrays of purely semiconducting single-walled carbon nanotubes. *Nature Nanotech. 8,* 347-355 (2013).

66. Wang, F. *et al*. Interactions between individual carbon nanotubes studied by Rayleigh scattering spectroscopy. *Phys. Rev. Lett. 96,* (2006).

67. Samsonidze, G. G. *et al*. The concept of cutting lines in carbon nanotube science. *J. Nanosci. Nanotechnol. 3,* 431-458 (2003).

68. Sun, D. M. *et al*. Flexible high-performance carbon nanotube integrated circuits. *Nature Nanotech. 6,* 156-161 (2011).

69. Javey, A. *et al*. Ballistic carbon nanotube field-effect transistors. *Nature 424,* 654-657 (2003).

70. Liu, K. H. *et al*. An atlas of carbon nanotube optical transitions. *Nature Nanotech. 7,* 325-329 (2012).

71. Liu, K. H. *et al*. Systematic determination of absolute absorption cross-section of individual carbon nanotubes. *Proc. Natl. Acad. Sci. U.S.A. 111,* 7564-7569 (2014).

72. Kuc, A., Zibouche, N., and Heine, T. Influence of quantum confinement on the electronic structure of the transition metal sulfide TS_2. *Phys. Rev. B 83,* (2011).

73. Mak, K. F. *et al*. Atomically thin MoS_2: A new direct-gap semiconductor. *Phys. Rev. Lett. 105,* (2010).

74. Splendiani, A. *et al*. Emerging photoluminescence in monolayer MoS_2. *Nano Lett. 10,* 1271-1275 (2010).

75. Zhang, Y. *et al*. Direct observation of the transition from indirect to direct bandgap in atomically thin epitaxial $MoSe_2$. *Nature Nanotech. 9,* 111-115 (2014).

76. Ji, Q. Q., Zhang, Y., Zhang, Y. F., and Liu, Z. F. Chemical vapour deposition of group-VIB metal dichalcogenide monolayers: Engineered substrates from amorphous to

single crystalline. *Chem. Soc. Rev.* *44,* 2587-2602 (2015).

77. Shi, Y. M., Li, H. N., and Li, L. J. Recent advances in controlled synthesis of two-dimensional transition metal dichalcogenides via vapour deposition techniques. *Chem. Soc. Rev.* *44,* 2744-2756 (2015).

78. Zeng, H. L. *et al*. Valley polarization in MoS_2 monolayers by optical pumping. *Nature Nanotech.* *7,* 490-493 (2012).

79. Mak, K. F., He, K. L., Shan, J., and Heinz, T. F. Control of valley polarization in monolayer MoS_2 by optical helicity. *Nature Nanotech.* *7,* 494-498 (2012).

80. Jones, A. M. *et al*. Optical generation of excitonic valley coherence in monolayer WSe_2. *Nature Nanotech.* *8,* 634-638 (2013).

81. Mak, K. F., McGill, K. L., Park, J., and McEuen, P. L. The valley Hall effect in MoS_2 transistors. *Science* *344,* 1489-1492 (2014).

Chapter 2 | Rayleigh scattering studies on interlayer interactions in structure-defined individual double-wall carbon nanotubes

2.1 Introduction

2.1.1 Interlayer interactions in van der Waals-coupled systems

There are numerous layered materials in nature that are coupled by van der Waals force. Since van der Waals force is a weak force, it is generally believed that it should have small effect on the electronic properties in layered systems which are coupled by van der Waals force between layers. However, recent studies on 2D materials has revealed that interlayer van der Waals coupling may also play an essential role in determining the electronic structures, and thus electronic and optical properties, of layered 2D materials. Experimental studies on bilayer graphene, for example, have shown that the coupling strength between two graphene layers depends on the mutual orientation; the energy at which van Hove singularities appear in the band dispersions relies on the twisted angles between two layers[1-2]. Notable changes in graphene electronic spectra have been observed in van der Waals graphene/hBN heterostructures, where a global bandgap is opened in graphene by break of A-B sublattice symmetry[3-4]. Interlayer interaction that has been believed weak in van der Waals system has also led to a drastic indirect-to-direct bandgap transition when the number of layers in molybdenum disulfide (MoS_2), tungsten disulfide (WS_2), *etc.* changes from two to monolayer, making these new layered materials very attractive and promising in photonic and optoelectronic applications[5-6].

Interlayer coupling by van der Waals interaction also widely exists in 1D systems. For example, carbon nanotubes[8], boron nitride nanotubes[9], and MoS_2 nanotubes[10] are 1D multilayer nanostructures in which interaction between component layers is van der Waals force by nature. Strong mechanical coupling (phonon coupling) has been recently reported in

double-wall carbon nanotubes (DWCNTs), that are composed of two carbon nanotubes nesting in a concentric manner, where the zone-center phonon frequencies (*e.g.*, radial breathing modes) have been drastically modified compared with those in each original tubes on account of the interlayer van der Waals coupling[11-12]. By the same token, electronic structures, and thus electronic properties of DWCNTs, should also be strongly affected by the van der Waals interaction. Although interlayer coupling is essential to understand the properties of multilayer one-dimensional systems, experimental study on the interlayer coupling effect on the electronic properties has so far been limited, and the coupling effect is still elusive.

DWCNTs are one of the most ideal and fundamental systems to explore such interlayer coupling in 1D systems[13]. Furthermore, DWCNTs are the simplest multilayer CNTs, where each CNT has well-defined structure known as chirality (n,m); therefore, the physical structure of a DWCNT can be represented by $(n_i,m_i)@(n_o,m_o)$, where (n_i,m_i) represents the chirality for inner tube and (n_o,m_o) denotes that for outer tube. Since an individual single-wall carbon nanotube can be either a metal or a semiconductor depending on the specified chirality, DWCNTs can be categorized into 4 groups: semiconducting@semiconducting (S@S), metallic@semiconducting (M@S), semiconducting@metallic (S@M) and metallic@metallic (M@M) (**see Figure 1**). To date, no detailed spectroscopic experiments have been reported on individual chirality-defined DWCNTs, and the effect of the interlayer coupling on electronic structures has remained elusive[14-16].
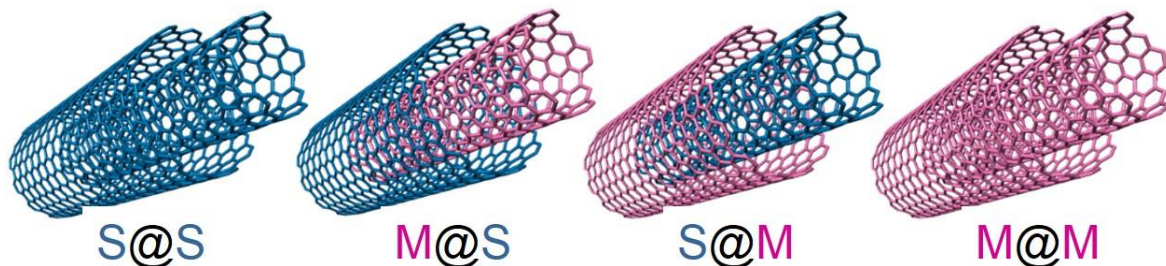
Figure 1. Structure model for DWCNTs that are categorized into four types.

2.1.2 Electron microscopy and Rayleigh scattering spectroscopy on individual CNTs

Electron microscopy (diffraction) is a very powerful technique for the chirality determination of individual isolated CNTs with high precision and being applicable to large diameter tubes[17-20]. Schematic in **Figure 2** illustrates a typical simulated diffraction pattern for a SWCNT with denoting important features and parameters for chirality assignment. Two sets of hexagons arising from diffraction patterns from graphene hexagonal lattice are oriented with an angle, which corresponds to the chiral angle of the tube. The intensity distributions for oscillation lines are different-order Bessel functions (Fourier transform for cylindrical coordinate) as donated; for example, intensity distributions along the equatorial line, l_2, and l_1 are the zero-order (approximated), n-th order and m-th order Bessel functions. The oscillation period D along equatorial line is approximated to be the inverse of tube diameter $1/d$. By measuring the distances between equatorial line with l_1 and $l2$, that is D_1 and D_2, together with the oscillation period D, we can obtain the value of n and m by the following relations:

$$D_1 = \frac{2n+m}{\sqrt{3}\pi} D \ (\textbf{Eq. 1}),$$
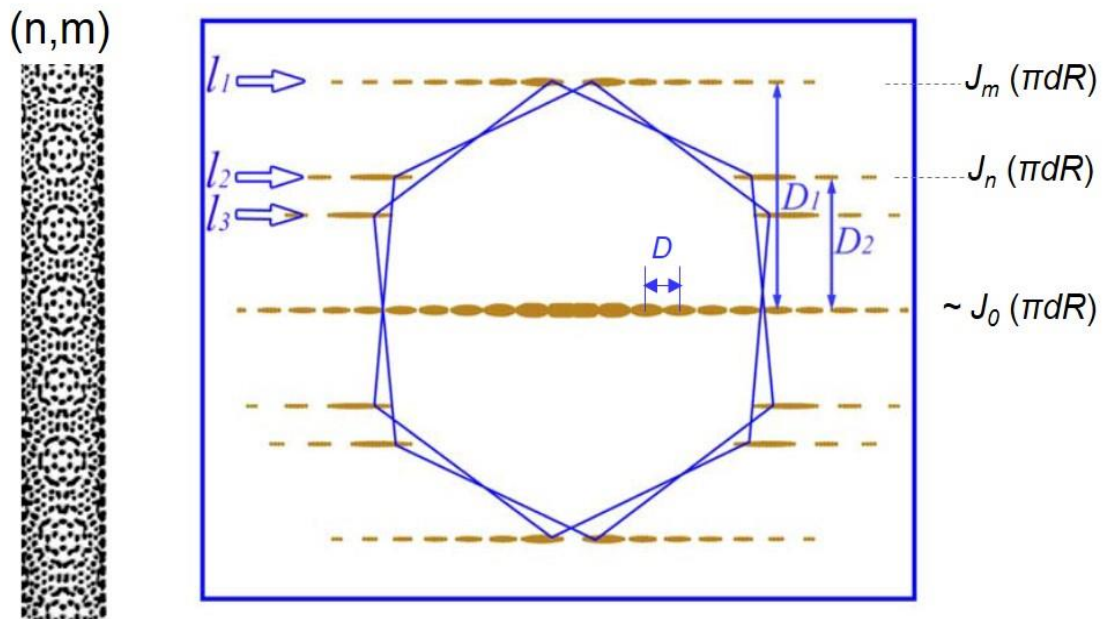
Figure 2. A typical electron diffraction pattern (simulated) from an individual SWCNT (n,m) (adapted from ref. 17).

$$D_2 = \frac{2m+n}{\sqrt{3}\pi} D \text{ (\textbf{Eq. 2})}.$$

Similarly, chirality assignment of DWCNTs can be achieved. In this case, two oscillation periods e and E present along the equatorial line in the diffraction patterns (**see Figure 3**). The diffraction intensity from outer tube is stronger than that form inner tube, which can readily be used to differentiate two tubes. By measuring the d_{o2}, d_{o3}, d_{i2}, d_{i3}, e and E, we can obtain the chirality $(n_i,m_i)@(n_o,m_o)$ of an isolated DWCNT the following by relations:

$$n_o = \frac{\pi}{\sqrt{3}}(2d_{o3} - d_{o2})(\frac{1}{e} + \frac{1}{E}) \text{ (\textbf{Eq. 3})},$$

$$m_o = \frac{\pi}{\sqrt{3}}(2d_{o2} - d_{o3})(\frac{1}{e} + \frac{1}{E}) \text{ (\textbf{Eq. 4})},$$

$$n_o = \frac{\pi}{\sqrt{3}}(2d_{i3} - d_{i2})(\frac{1}{e} - \frac{1}{E}) \text{ (\textbf{Eq. 5})},$$

$$n_o = \frac{\pi}{\sqrt{3}}(2d_{i3} - d_{i2})(\frac{1}{e} - \frac{1}{E}) \text{ (\textbf{Eq. 6})}.$$
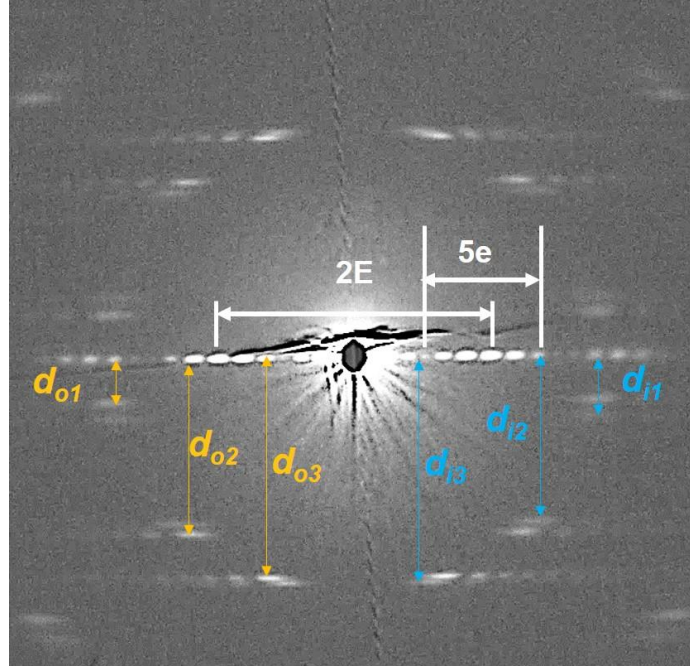
Figure 3. Experimental electron diffraction pattern for an individual DWCNT whose chirality is assigned to be (16,6)@(22,11).

Through the pattern analysis, the chirality of this DWCNT is determined to be (16,6)@(22,11). The assigned chirality can be directly compared with simulated pattern to further confirm the results.

Rayleigh scattering spectroscopy was first developed and applied to probing the optical transitions of individual carbon nanotubes in 2004 by groups in Columbia University[21-22]. **Figure 4** shows the optical set-up for Rayleigh scattering measurements on individual free-standing carbon nanotubes[23]. The spectra were taken over a broad range of photon energy from 1.2 eV – 2.7 eV enabled by sample illumination by a continuous wave (CW) supercontinuum laser beam. In this range, we usually probe optical transitions of S_{33}, S_{44} and M_{22}, *etc.* for tubes with medium diameters (for example, 1.5 nm – 2.5 nm). The measured intensity (or cross-section σ) is proportional to $\omega^3|\chi(\omega)|^2$, where $\chi(\omega)$ is the complex electric susceptibility of CNTs. For an excitonic transition $\chi(\omega)$ can be modelled by a Lorentianz profile

$$\chi(\omega) \sim [(\omega_0 - \omega) - i\gamma/2]^{-1} \ (\textbf{Eq. 7}),$$

where ω_0 is the resonant frequency, γ is a phenomenological width[24]. Therefore, the resonant transition energies and the corresponding peak widths can be extracted by fitting the experimental spectra by $\omega^3|\chi(\omega)|^2$. Non-resonant contributions to χ (away from ω_0), *e.g.*, from the tails of neighboring resonances, or the onset of free-carrier transitions are responsible for the typical asymmetric line shapes as shown in the figure. Rayleigh scattering spectroscopy is a spectroscopic probing technique that enables individual CNT spectroscopy with a broadband energy resolution and noninvasive nature. For convenience and consistency of discussion throughout the thesis, we respectively denote the i-th order optical transition from semiconducting and metallic CNTs by S_{ii} and M_{ii}; M_{ii}^- and M_{ii}^+ represent the i-th order low- and high-energy transitions of metallic tubes resulting from the trigonal wrapping effect[25].
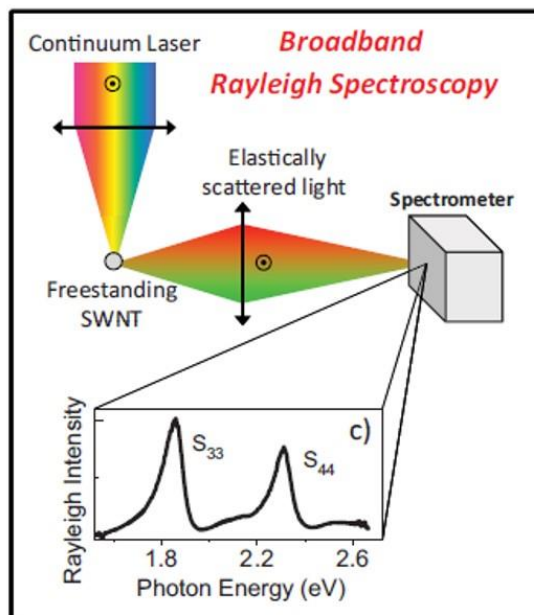
Figure 4. Rayleigh optical set-up and typical Rayleigh spectrum from an individual CNT (16,12) (adapted from ref. 23).

2.2 Experimental
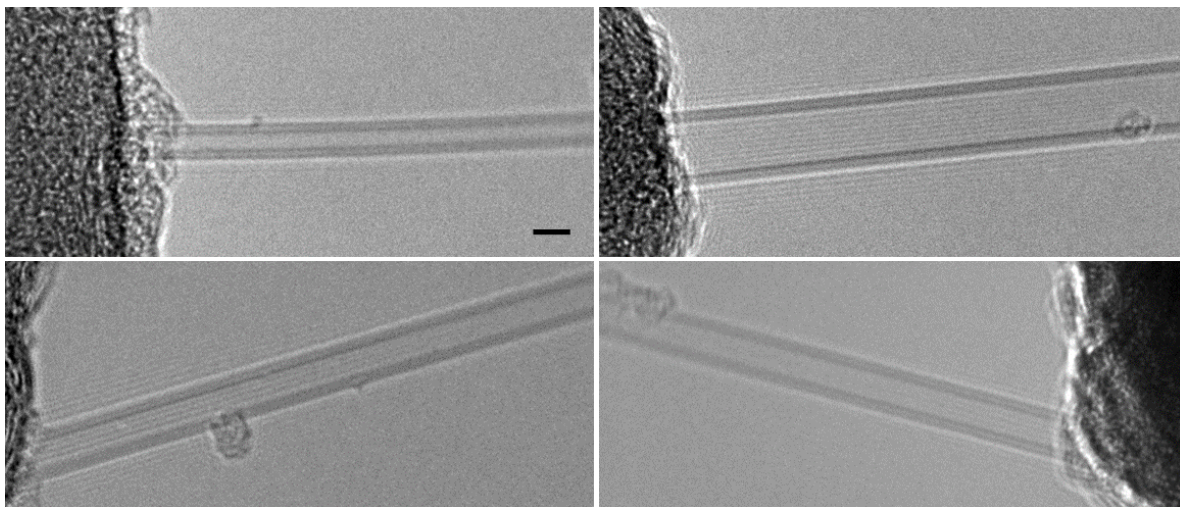
Figure 5. TEM images of air-suspended individual DWCNTs grown by alcohol catalytic CVD across an open slit. Note that the so-grown tubes are very clean with minimal amount of impurities such as amorphous carbons. The scale bar shown in the first image is 2 nm.

A direct chemical vapor deposition (CVD) method has been developed for the preparation of air-suspended long and clean individual DWCTNs for probing the effect of interlayer interactions on electronic structures in DWCNT systems. As shown in **Figure 5**, very clean air-suspended individual DWCNTs on an open slit with a width of ~ 30 μm can be
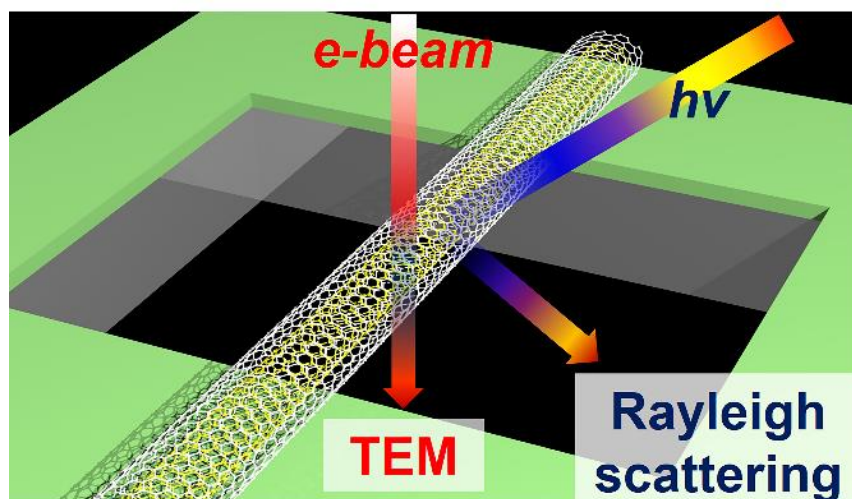
Figure 6. Schematic showing experimental configuration for simultaneous structural indexing and spectroscopy characterization for an individual free-standing DWCNT.

prepared. Here, we used the CVD method with alcohol as the carbon source and Fe as the

catalyst. We then directly apply two experimental techniques, Rayleigh scattering spectroscopy and transmission electron microscopy, on the same individual DWCNTs that are prepared in a suspended manner without being effected by the underlying supporting materials as depicted in a schematic in **Figure 6**. We thus can achieve a simultaneous determination of the optical transition energies and precise chiral indices of the same individual DWCNTs by the combination of Rayleigh scattering spectroscopy and electron diffraction.
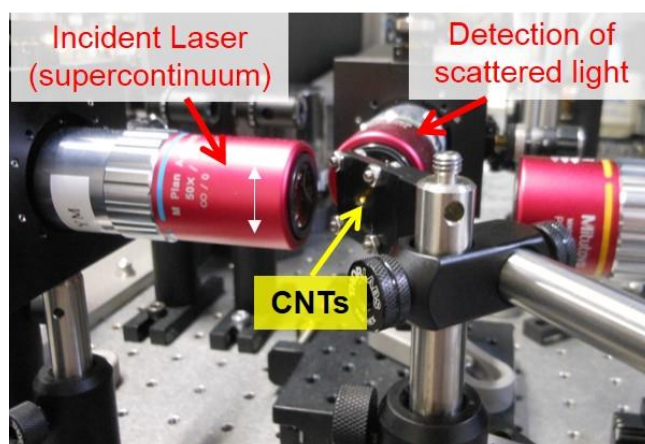
Figure 7. Photo of Rayleigh set-up in the vicinity of sample position used in this study.

Figure 7 shows the photo of part of the Rayleigh set-up used in this study (collaboration with Prof. Kazunari Matsuda and Assoc. Prof. Yuhei Miyauchi in Kyoto University). **Figure 8** shows the schematic representation for the optical Rayleigh set-up used in this study.
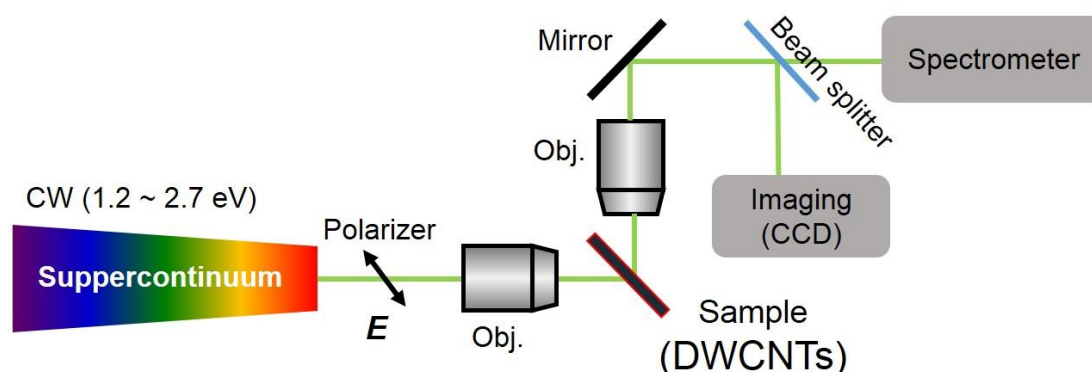
Figure 8. Schematic representation for the optical Rayleigh set-up used in this study. We used CW supercontinuum white light as illumination source (1.2 eV – 2.7 eV) which enabled a broadband spectroscopy measurement. We used a polarized light to illuminate samples with the polarization in concert with the tube axis (as shown in the figure). We used a beam splitter to image suspended tubes and to measure the spectroscopy.
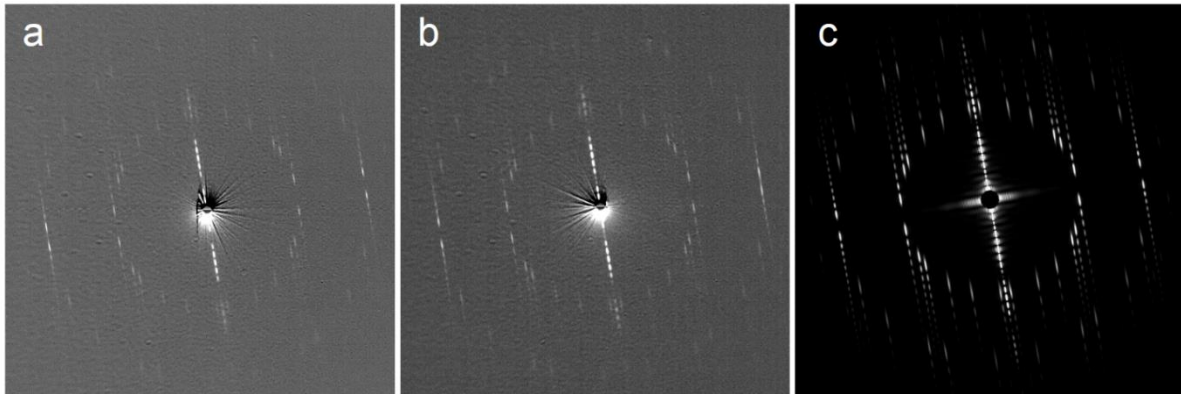
Figure 9. An example showing the structure rigidity of a free-standing DWCNT (no alteration of chiral indices). (a) An electron diffraction pattern taken close to one edge of the slit. (b) Electron diffraction pattern of the same tube taken close to the other edge of the slit. The two places are ~ 30 μm apart. (c) A diffraction simulation pattern of a (23, 4)@(22, 18) DWCNT which is identical with experimental patterns shown in (a) and (b).

Electron diffraction was performed on tubes in the vicinity of edge of slit, whereas suppercontinuum laser beam was focused on the center of the suspended tubes to avoid the effect of electron-beam-induced damages on the Rayleigh scattering spectra. The so-prepared DWCNTs have shown the same wall structures without alternations over long range (at least ~ 30 μm) which enables us to directly correlate the Rayleigh spectra for individual DWCNTs to
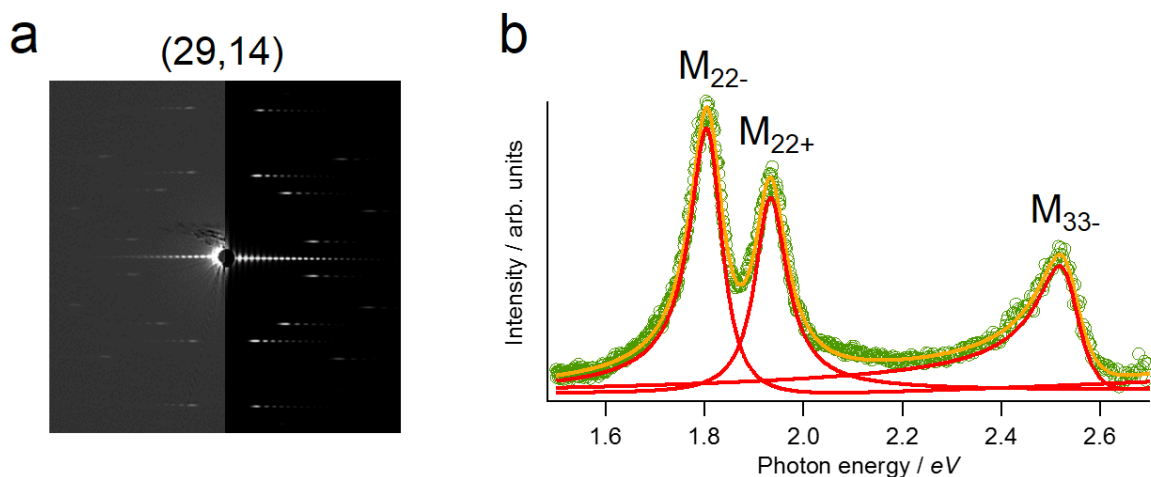
Figure 10. Electron microscopy and Rayleigh scattering spectroscopy characterization on a suspended SWCNT. (a) Electron diffraction pattern and diffraction simulation of a SWCNT (29,14). (b) Corresponding Rayleigh spectrum with peak fitting. Note that the intensity ratio M_{22}^+/M_{22}^- is smaller than 1.

the chiral indices determined by electron diffraction. One of the confirmation results is shown in **Figure 9.** Prior to probing the interlayer coupling effect in DWCNT systems, we confirmed

the validity and precision of the combinational Rayleigh scattering spectroscopy and electron microscopy on individual SWCNTs. One of the typical results is presented in **Figure 10**, where experimental electron diffraction pattern, simulated pattern, and corresponding Rayleigh spectrum are shown. By careful pattern analysis based on **Eq. 1** and **Eq. 2**, the chirality of this SWCNT was determined to be (29,14), which is a metallic tube. This chirality assignment was further corroborated through detailed comparison with simulated patterns in which the experimental result is in excellent agreement with the simulated (29,14) SWCNT. All the measured optical transition energies at 1.81 eV, 1.93 eV and 2.53 eV probed by Rayleigh scattering measurements, were successfully assigned to M_{22}^{-}, M_{22}^{+} and M_{33}^{-} transitions of (29, 14) SWCNT, respectively, which are well-consistent with the previous results[26].

2.3 Results and discussion

2.3.1 Rayleigh spectroscopy on S@S DWCNTs

Figure 11a shows the Rayleigh spectrum for the chirality-identified DWCNT (16, 6)@(22, 11), in which three distinct transitions peaked at 1.63, 1.90, and 2.05 eV are identified by fitting each peaks using relation $\omega^3|\chi(\omega)|^2$ and (**Eq. 7**) introduced in 2.1.2. The origin of small peaks at 1.81 and 2.25 eV is assigned to be the phonon sideband[27]. Figure 11c is the TEM image of the same DWCNT with showing clear a double wall structures. Through pattern analysis by using the **Eq. 3 – Eq. 6** introduced in 2.1.2, the chirality of this DWCNT is uniquely determined to be (16,6)@(22,11); the experimental result is in very good accordance with the simulated pattern with a chirality of (16,6)@(22,11) as shown in **Figure 11b**. The optical transitions from inner- and outer tubes have successfully been assigned as shown in **Figure 11a**; the three peaks are S_{33} and S_{44} transitions of outer tube and S_{33} transition of inner tube, respectively. As clearly seen in **Figure 11a**, good fitting of each peak by a single asymmetric Lorentzian profile indicates that optical transition in DWCNTs is also an excitonic process.
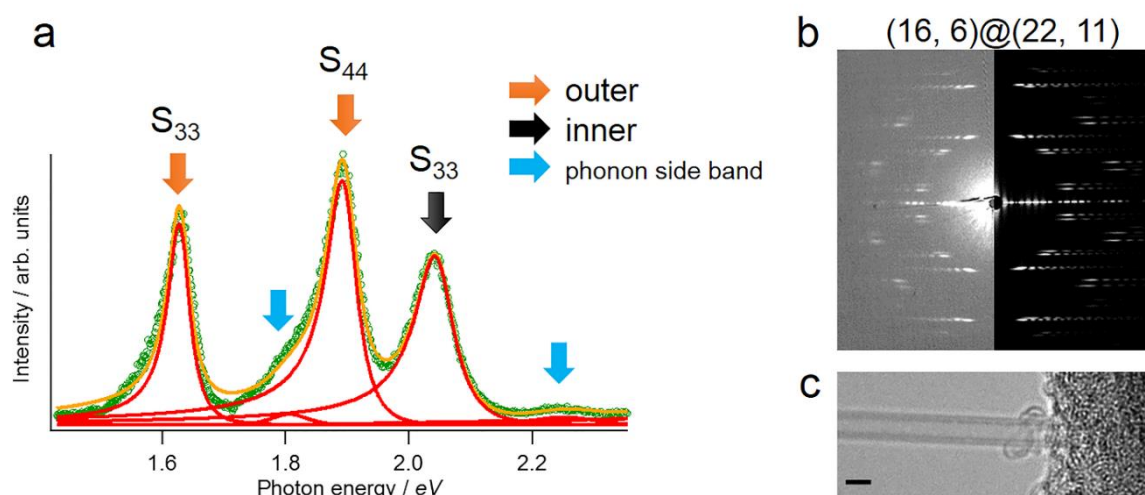
Figure 11. (a) Rayleigh spectrum for a DWCNT (16, 6)@(22, 11) which is a S@S DWCNT. Green circles are experimental data that can be fitted well by asymmetric Lorentzian profiles for each peaks (overall fit data is shown by orange curve). (b) Electron diffraction pattern and simulated pattern. (c) TEM image of the exactly same DWCNT (scale bar is 2 nm).

The peak fitting gives information on dephasing time (τ) of excitons since the full width at half maximum (FWHM γ defined in **Eq. 7**) of each transition is inversely proportional to τ. The observed γ for S_{33} and S_{44} of outer tube and for S_{33} of inner tube are 0.055, 0.079 and 0.078 eV, respectively, which are larger than typical FWHMs of S_{11} in SWCNTs[28]. We observed comparable γ and thus the dephasing time for DWCNTs (S_{33} and S_{44}) and for SWCNTs. Decay time of a few fs and a few tens of fs were reported by Hertel *et al.* and Lauret *et al.*, respectively[29-30], which are much shorter than the reported decay time in energy transfer between inner- and outer tube (time constant is ca. 150 fs)[31]; these experimental facts explain the comparable dephasing time observed here.

Optical transition energies of each SWCNTs (16, 6) and (22, 11) in the DWCNT (16, 6)@(22, 11) show red shifts in energy when comparing with those of isolated SWCNTs that were reported in previous work under similar experimental conditions[26]. The values of red shifts are 0.07, 0.04 eV for S_{33} and S_{44} of outer (22, 11) tube and 0.09 eV for S_{33} of inner (16, 6) tube, respectively. The error is estimated to be ca. 6 meV, which is rather small relative to the shift values. The average redshift in transition energies for S tubes is ca. 0.06 eV for S@S DWCNTs (total 15 transitions).

2.3.2 Rayleigh spectroscopy on S@M DWCNTs

The redshifts in transition energies in S@M DWCNTs are significantly larger when comparing with S@S DWCNTs. **Figure 12** shows a typical Rayleigh spectrum for an individual S@M DWCNT. **Figures 13a** and **13b** show the corresponding TEM image and electron diffraction pattern with simulated pattern for the same DWCNT. The chiral index of this DWCNT is uniquely determined to be (26, 25)@(42, 18). All the observed optical transitions in the spectrum are successfully assigned: M_{22}^-, M_{22}^+, M_{33}^-, M_{44}^-, and M_{44}^+ for outer

metallic CNT and S_{55}, S_{66} and S_{77} for inner semiconducting CNT. Fitting by asymmetric

Lorentizan profiles gives rise to redshifts of each transitions of 0.19, 0.16 and 0.09 eV for S_{55},

S_{66} and S_{77} for inner tube and 0.05, 0.01, 0.08, 0.05 and 0.07 eV for M_{22}^{-}, M_{22}^{+}, M_{33}^{-}, M_{44}^{-}, and

M_{44}^{+} for outer tube, respectively.   As we can see, the energy redshifts of M_{22}^{-}, M_{22}^{+}, M_{33}^{-},

M_{44}^{-}, and M_{44}^{+} are comparable to those in S@S. However, the energy redshifts of S_{55}, S_{66} and
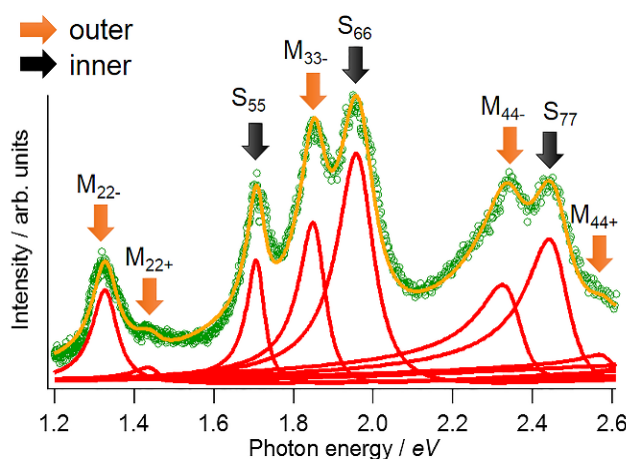
Figure 12. Rayleigh spectrum for a S@M DWCNT that is determined to be (26, 25)@(42, 18).

S_{77} are significantly larger than those in S@S. The average redshift in transition energy of S_{ii}

in S@M DWCNTs (total 14 transitions) is 0.13 eV. We realize that observed intensities of

M_{ii}^{+} transitions are always weaker than those of low-energy counterparts M_{ii}^{-}. This observation

in DWCNTs in conjunction with that in metallic SWCNTs (**see Figure 10**) is consistent with

previous Rayleigh scattering cross-section calculation results[32].
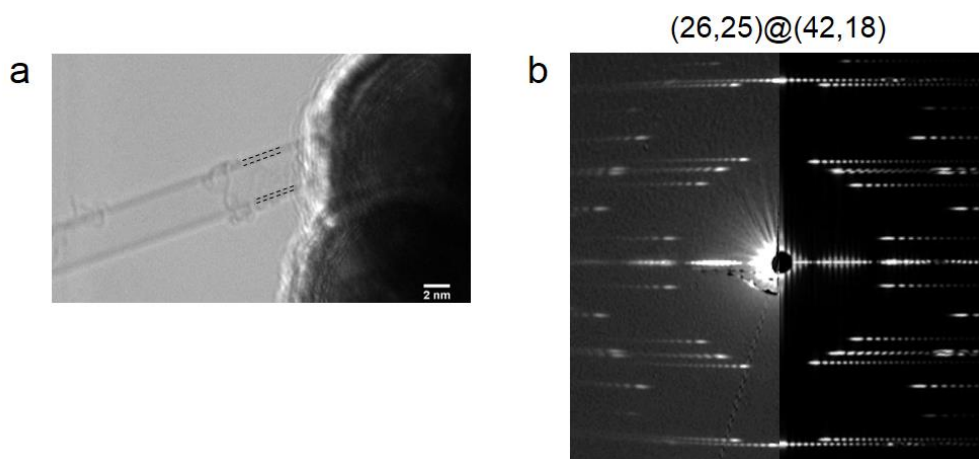
Figure 13. (a) TEM image of an isolated DWCNT that is assigned as (26, 25)@(42, 18). (b) Electron diffraction pattern (left) with comparison to the simulated one (right).

2.3.3 Discussion on redshifts in transition energies

Total 29 optical transitions in chirality-identified individual air-suspended DWCNTs are examined very carefully. The experimental results are summarized in **Figure 14**, **Figure 15**, and **Table 1**. **Figure 14** summarizes the shifts in optical transition energies for semiconducting tubes (total 21 transitions) in both S@S and S@M configurations, and **Figure**
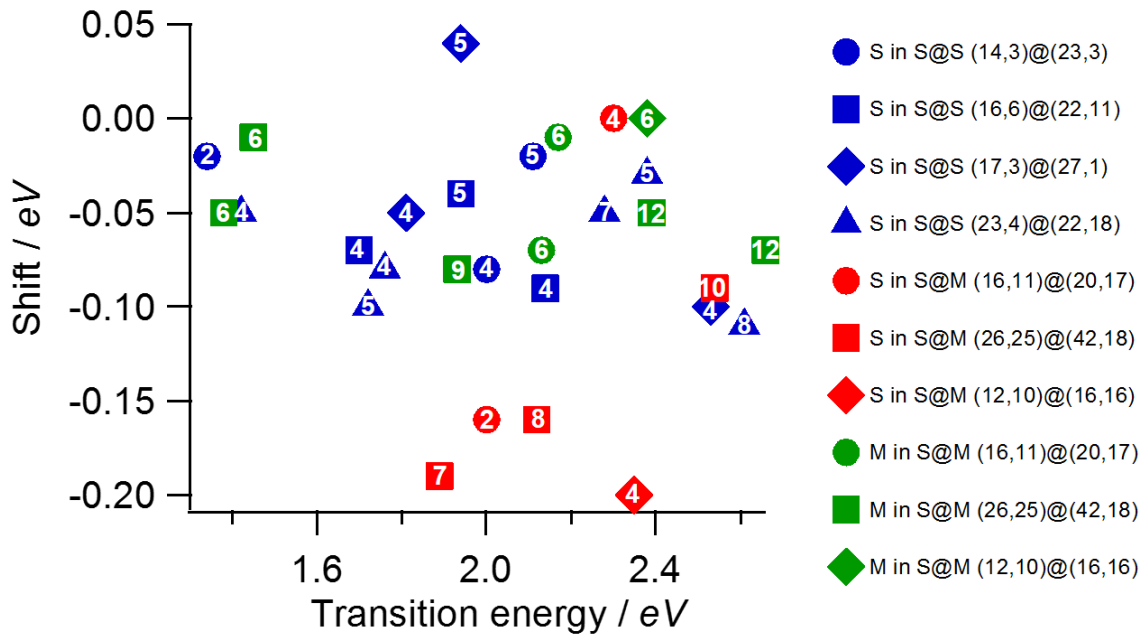
Figure 15. Shift profile for all the 29 optical transitions that were investigated in this study. The numbers donate the p values, where p= 2, 4, 5, 6, 7, 8, 9, 10 and 12 for S_{22}, S_{33}, S_{44}, M_{22}, S_{55}, S_{66}, M_{33}, S_{77} and M_{44}, respectively.

15 summarizes the shifts in transition energies for all the tubes investigated, which includes the metallic species. Details for each transitions, such as order of transitions, diameter, transition energies, *etc.* are tabulated in **Table 1**. The integer numbers in **Fig. 14, Fig. 15,** and **Table 1** donate the p values that can index the optical transitions in both semiconducting and metallic nanotubes. For example, p = 1, 2, 3, 4, 5, 6, 7. 8, 9, 10 represent optical transitions for S_{11}, S_{22}, M_{11}, S_{33}, S_{44}, M_{22}, S_{55}, S_{66}, M_{33}, S_{77}. As shown in **Figs. 14** and **15**, all the optical transitions (except for one data) display redshifts in energy relative to those in isolated SWCNTs.
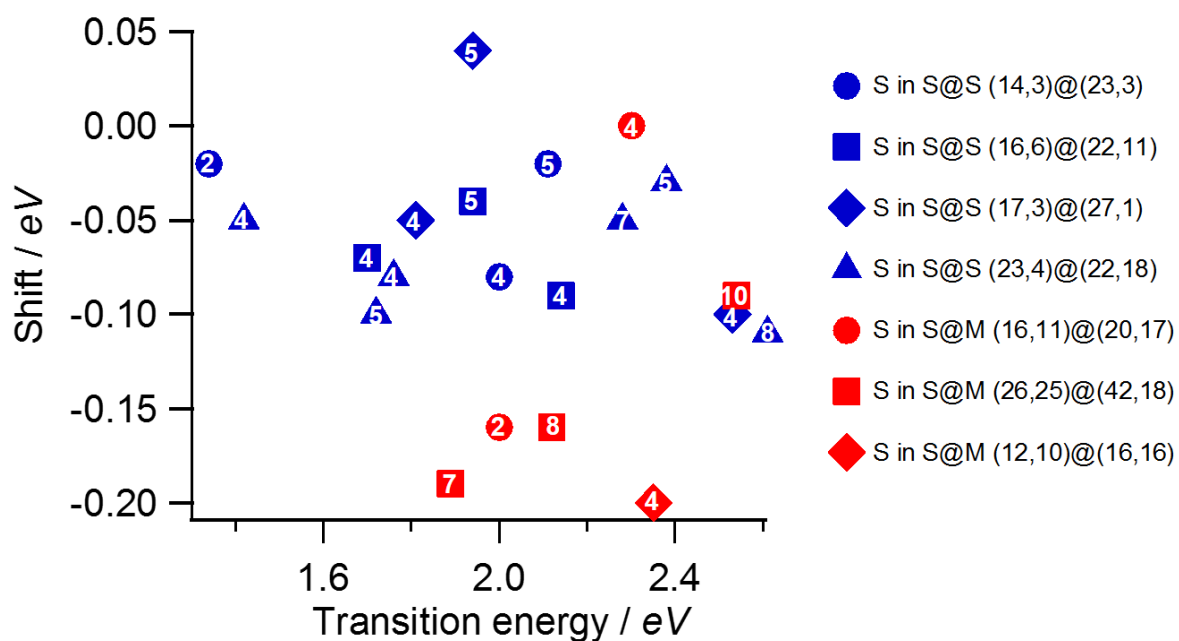
Figure 14. Summary of shifts in transition energies for semiconducting tubes in DWCNTs. The numbers donate the p values, where p = 2, 4, 5, 7, 8 and 10 are for S_{22}, S_{33}, S_{44}, S_{55}, S_{66} and S_{77} transitions, respectively.

Table 1. Database for optical transitions in DWCNTs investigated in this study.

	Transition	p	diameter (nm)	p/diameter (1/nm)	Transition energy of DWCNT_exp. (eV)	Transition energy of SWCNT_ref. (eV)	shift (eV)
Inner	S_{22}	2	1.841	1.086	1.84	2	-0.16
(16,11)	S_{33}	4	1.841	2.173	2.3	2.3	0
Outer	M_{22-}	6	2.512	2.389	2.06	2.13	-0.07
(20,17)	M_{22+}	6	2.512	2.389	2.16	2.17	-0.01
Inner	S_{55}	7	3.459	2.024	1.7	1.89	-0.19
	S_{66}	8	3.459	2.313	1.96	2.12	-0.16
(26,25)	S_{77}	10	3.459	2.891	2.45	2.54	-0.09
	M_{22-}	6	4.176	1.437	1.33	1.38	-0.05
	M_{22+}	6	4.176	1.437	1.44	1.45	-0.01
Outer	M_{33-}	9	4.176	2.155	1.85	1.93	-0.08
(42,18)	M_{44-}	12	4.176	2.874	2.34	2.39	-0.05
	M_{44+}	12	4.176	2.874	2.59	2.66	-0.07
Inner (12,10)	S_{33}	4	1.494	2.677	2.15	2.35	-0.2
Outer (16,16)	M_{22}	6	2.17	2.765	2.38	2.38	0
Inner (14,3)	S_{22}	2	1.231	1.625	1.32	1.34	-0.02
Outer (23.3)	S_{33}	4	1.929	2.074	1.92	2	-0.08
	S_{44}	5	1.929	2.592	2.09	2.11	-0.02
Inner (16,6)	S_{33}	4	1.542	2.594	2.05	2.14	-0.09
Outer (22,11)	S_{33}	4	2.279	1.755	1.63	1.7	-0.07
	S_{44}	5	2.279	2.194	1.9	1.94	-0.04
Inner (17,3)	S_{33}	4	1.463	2.734	2.43	2.53	-0.1
Outer (27,1)	S_{33}	4	2.154	1.857	1.76	1.81	-0.05
	S_{44}	5	2.154	2.321	1.98	1.94	0.04
Inner (23,4)	S_{33}	4	1.976	2.024	1.68	1.76	-0.08
	S_{44}	5	1.976	2.530	2.35	2.38	-0.03
	S_{33}	4	2.717	1.472	1.37	1.42	-0.05
	S_{44}	5	2.717	1.840	1.62	1.72	-0.1
Outer (22,18)	S_{55}	7	2.717	2.576	2.23	2.28	-0.05
	S_{66}	8	2.717	2.944	2.5	2.61	-0.11

Note 1: p is 2, 4, 5, 6, 7, 8, 9, 10 and 12 for S_{22}, S_{33}, S_{44}, M_{22}-(+), S_{55}, S_{66}, M_{33}-(+), S_{77} and M_{44}-(+), respectively.

Note 2: Transition energies of SWCNTs are referred to ref. 26.

One of the most important factors to explain the observed redshifts in transition energies is the environmental dielectric screening effect. In general, the transition energies of S_{ii} or M_{ii} (E_{ii}) can be represented as

$$E_{ii} = E_o + E_s - E_b \text{ (Eq. 8)},$$

where E_o, E_s and E_b respectively correspond to one-particle energy (single-particle bandgap), self-energy (electron-electron interaction) and exciton binding energy (electron-hole interaction) as shown in **Figure 16**. The term $E_s - E_b$ in (**Eq. 8**) corresponds to many-body Coulombic corrections to one-particle bandgap, which is inherently essential in one-dimensional systems such as CNTs[33-34]. By theory, self-energy E_s in CNTs is composed of two contributions: 1D long-range (length scale longer than the tube circumference), and 2D short-range (length scale shorter than the circumference) interactions[35]. The 1D
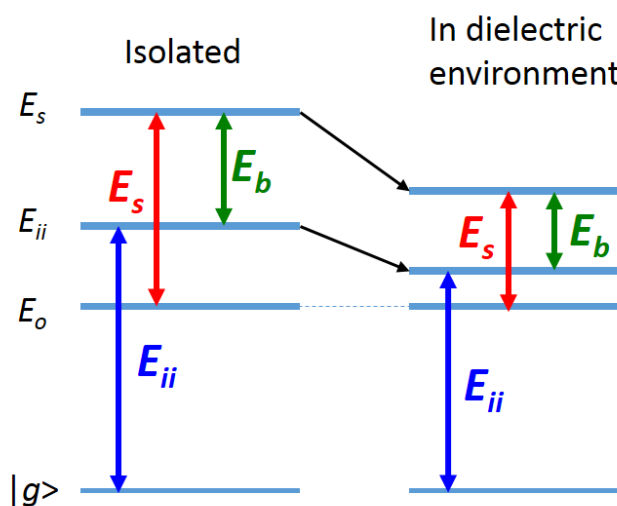
Figure 16. Schematic representation showing the relation between different parts of energy that determine optical transition energy E_{ii} in CNT, and the effect of dielectric screening on the E_s and E_b and thus the optical transition energy E_{ii}. The physical meaning of E_o, E_s, E_b, and E_{ii} are explained in the main text.

long-range contribution in E_s and exciton binding energy E_b, which is also a 1D long-range interaction, almost cancel each other, leading to a moderate enhancement of the optical transition energies[35-36]. The enhancement of the optical gap, therefore, predominantly arises from the 2D short-range interactions in E_s term, which has a positive value. As a result, the

measured optical transition energy E_{ii} in CNTs always show a positive shift relative to single-particle bandgap. The 2D short-range interactions can be reduced by dielectric media around CNTs due to dielectric screening effect of Coulomb interactions, leading to redshift in the exciton energy levels in CNTs. The observed redshifts in DWCNTs thus indicate that the interlayer dielectric screening of Coulomb interactions play an important role in optical transitions in DWCNTs. The importance of interlayer screening in optical transitions in DWCNTs has also been pointed out by a recent theoretical calculation based on a static screened Hartree-Fock approximation within a k·p scheme[37]. In **Fig. 14**, distinct Coulombic screening effect between metallic CNTs and semiconducting CNTs can clearly be seen. The redshifts of exciton energies in S@S are about 0.1 eV at largest, whereas redshifts of exciton energies for inner CNTs in S@M reach to 0.2 eV. Theoretical calculations based on the static screened Hartree-Fock approximation have shown that the interlayer Coulombic screening causes redshift on lowest-lying exciton energies in DWCNTs, where the redshifts in S_{11} and S_{22} transitions of inner CNTs have been calculated to be 0.015 ~ 0.02 eV for S@S, and 0.02 ~ 0.03 eV for S@M[37]. The larger redshift predicted in S@M arises from strong screening by free electrons in metallic outer CNT; this fact is qualitatively consistent with the observed large redshifts in transitions of inner CNTs in S@M.

The typical redshifts for S_{11} and S_{22} transitions in SWCNTs in various dielectric environments in previous studies were found in the range 0.01 ~ 0.05 eV[38-39]. We observed much larger ~ 0.2 eV redshifts in our study for high-order optical transitions (primary S_{33} and S_{44}) presumably due to the larger contribution of self-energy (E_s) to the high-order excitonic transition energies. One of the calculation works based on an extended-tight-binding model has shown that $E_s - E_b$ in SWCNTs with diameter of about 2 nm is 0.3 ~ 0.4 eV for S_{33} and S_{44}, that is much larger than the value of 0.1 ~ 0.2 eV for S_{11} and S_{22}[40]. The larger redshifts for high-order excitonic transitions found in DWCNTs are a direct consequence of larger reduction

of E_s against E_b because of the larger contribution of E_s to the optical transition energies. We also note that the redshifts observed in DWCNTs are also larger (averagely speaking) than those in SWCNT bundles (~ 0.05 eV), which can be ascribed to the more effectiveness of interlayer dielectric screening in DWCNTs over SWCNT bundles[41].

2.3.4 Further remarks on interlayer interactions in DWNCTs

Although the effect of interlayer dielectric screening reasonably explains the observed redshifts in optical transition energies in DWCNTs, occasionally, we also found blueshift in transition energies as already displayed in **Figs. 14** and **15**, as well as new optical transition peaks that are not belong to any of the original ones in SWCNTs in the chirality-identified Rayleigh spectra. The two situations are shown in **Figures 17a** and **17b**, respectively.
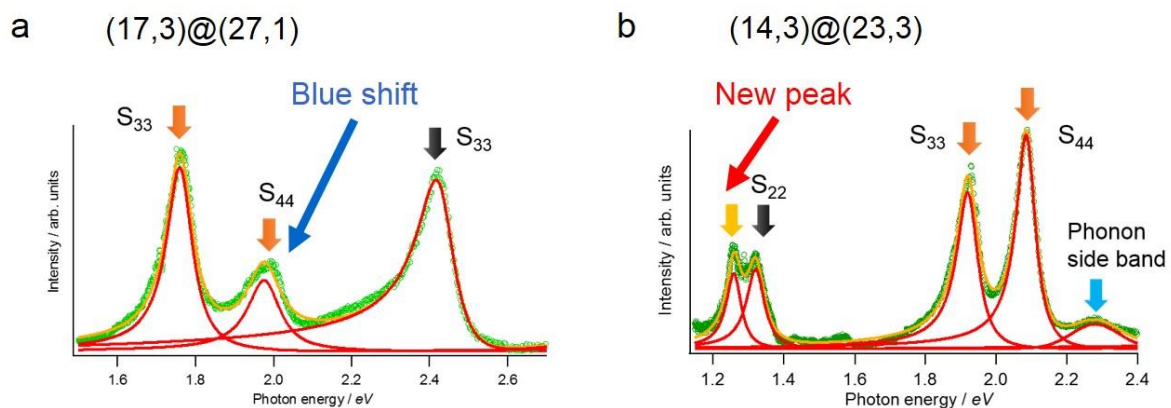
Figure 17. (a) Blueshift of S_{44} transition of outer tube in a (17,3)@(27,1) DWCNT. (b) New optical transition observed in a (14,3)@(23,3) DWCNT. In both figures, orange arrows mark transitions from outer tubes, and black arrows mark those from inner tubes.

Similar energy blueshifts (small probability with small shift values), were very recently observed by a Berkeley research group[42]. The energy blueshifts were explained as a consequence of a direct hybridization of electron wavefunctions between inner- and outer tubes, which demonstrates a strong chirality-dependence relying on the specific chirality combinations. Our data displayed in **Figure 17a** shows a blueshift of 0.04 eV in optical

transition energy for S_{44} for outer tube in a (17,3)@(27,1) DWCNT. The observations of blueshifts in optical transition energies in DWCNT systems have not been reported before.

Figure 17b shows one of the typical examples of presence of new optical transitions revealed in Rayleigh spectra as marked. The origin of this new peak must arise from radically strong interlayer interaction between two tubes that are both near-zigzag tubes. Our experimental observation is consistent with a recent calculation work in which a spectacular electronic structure variations in 1D Moiré crystals formed by two rigid CNTs without commensurability were shown[43]. **Figure 18** shows one of the calculated results for a DWCNT (26,3)@(35,3) comprising two semiconducting near-zigzag tubes[43]. **Figure 18a** shows the calculated band structure of a (26,3)@(35,3) DWCNT without interlayer coupling, whereas **Figure 18b** shows the band structure with direct orbital coupling between tubes. As clearly seen, drastic band variations (formation of localized insulating states) were induced when the
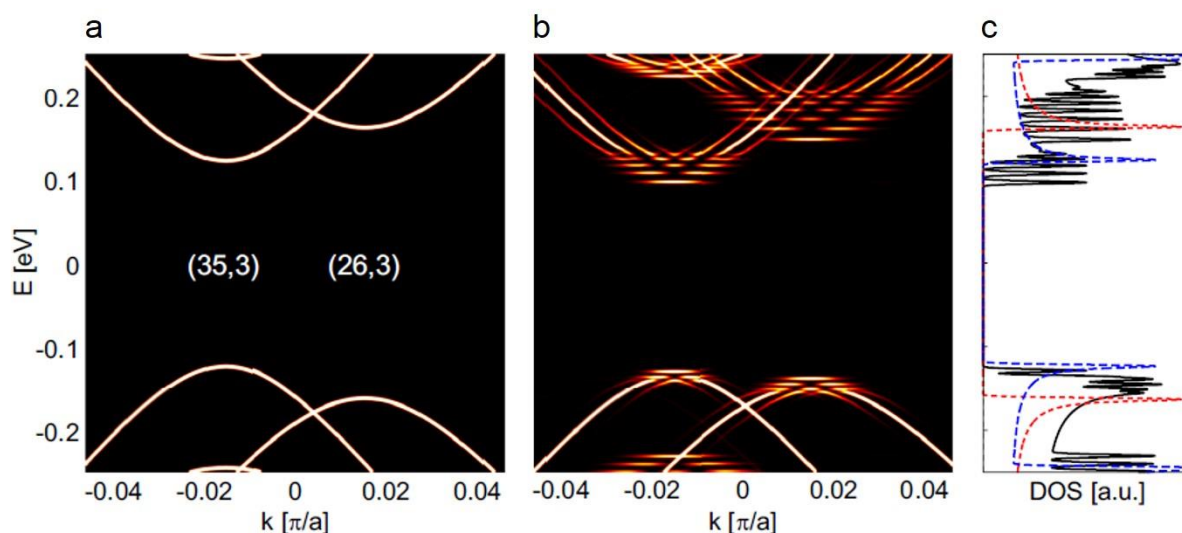
Figure 18. Calculation results of interlayer coupling effect on the electronic band structure in a DWCNT (26,3)@(35,3) (adapted from ref. 43). (a) Band structure for the decoupled DWCNT. (b) Band structure for the coupled case. (c) Calculated density of states (DOS). Black lines show the DOS for the coupled DWCNT; blue and red dashed lines show the corresponding DOS for plain outer (35,3) tube and inner (26,3) tube, respectively.

interlayer coupling is switched on. **Figure 18c** shows the calculated density of states (DOS) for the plain SWCNTs (blue and red dashed lines) and coupled DWCNT (black lines). The

study and understanding of effect of interlayer interactions on the electronic structures in 1D are still on the early stage[44], and we anticipate more efforts and works to be involved to address this interesting issue in near future.

2.4 Conclusions

A simultaneous Rayleigh scattering spectroscopy and electron microscopy have been developed and applied to probing the interlayer interactions in DWCNTs, a 1D van der Waals model system, prepared by CVD method. Optical transition energies in individual structure-defined DWCNTs were measured and directly compared to those in individual SWCNTs with the same chirality. We found that most of the optical transitions in DWCNTs show redshifts in energies relative to SWCNTs. Energy redshifts were discussed and explained in the context of dielectric screening effect between inner- and outer tubes. In the S@M DWCNTs, the values of redshifts for semiconducting tubes are significant larger than those observed in S@S DCWNTs. We also emphasize the findings of energy blueshift and new optical transitions a few structure-defined DWCNTs, which may be due to the direct coupling of electron wavefunctions between two tubes. All the experimental results point to the conclusion that interlayer interactions in 1D van der Waals-coupled systems can be very strong to alter the electronic band structure (electronic and optical properties) of DWCNTs. As a result, a DWCNT should not be simply regarded as two plain SWCNTs in terms of electronic properties. More careful and systematic studies are needed to fully elucidate the interlayer interactions in 1D van der Waals-coupled systems.

2.5 References

1. Li, G. H. *et al.* Observation of van Hove singularities in twisted graphene layers. *Nature Phys.* *6,* 109-113 (2010).

2. Brihuega, I. *et al.* Unraveling the intrinsic and robust nature of van Hove singularities in twisted bilayer graphene by scanning tunneling microscopy and theoretical analysis. *Phys. Rev. Lett.* *109,* (2012).

3. Ponomarenko, L. A. *et al.* Cloning of Dirac fermions in graphene superlattices. *Nature* *497,* 594-597 (2013).

4. Dean, C. R. *et al.* Hofstadter's butterfly and the fractal quantum hall effect in moiré superlattices. *Nature* *497,* 598-602 (2013).

5. Mak, K. F. *et al.* Atomically thin MoS_2: A new direct-gap semiconductor. *Phys. Rev. Lett.* *105,* (2010).

6. Wang, Q. H. *et al.* Electronics and optoelectronics of two-dimensional transition metal dichalcogenides. *Nature Nanotech.* *7,* 699-712 (2012).

7. Geim, A. K. and Grigorieva, I. V. van der Waals heterostructures. *Nature* *499,* 419-425 (2013).

8. Andrews, R., Jacques, D., Qian, D. L., and Rantell, T. Multiwall carbon nanotubes: Synthesis and application. *Acc. Chem. Res.* *35,* 1008-1017 (2002).

9. Golberg, D. *et al.* Boron nitride nanotubes and nanosheets. *ACS Nano* *4,* 2979-2993 (2010).

10. Nath, M., Govindaraj, A., and Rao, C. N. R. Simple synthesis of MoS_2 and WS_2 nanotubes. *Adv. Mater.* *13,* 283-286 (2001).

11. Levshov, D. *et al.* Experimental evidence of a mechanical coupling between layers in an individual double-walled carbon nanotube. *Nano Lett.* *11,* 4800-4804 (2011).

12. Liu, K. H. *et al.* Quantum-coupled radial-breathing oscillations in double-walled carbon

nanotubes. *Nat. Commun.* *4,* (2013).

13. Endo, M. *et al.* 'Buckypaper' from coaxial nanotubes. *Nature 433,* 476-476 (2005).

14. Kociak, M. *et al.* Linking chiral indices and transport properties of double-walled carbon nanotubes. *Phys. Rev. Lett.* *89,* (2002).

15. Tison, Y. *et al.* The inner shell influence on the electronic structure of double-walled carbon nanotubes. *Adv. Mater.* *20,* 189-194 (2008).

16. Liu, K. H. *et al.* Chirality-dependent transport properties of double-walled nanotubes measured *in situ* on their field-effect transistors. *J. Am. Chem. Soc.* *131,* 62-63 (2009).

17. Qin, L. C. Electron diffraction from carbon nanotubes. *Rep. Prog. Phys.* *69,* 2761-2821 (2006).

18. Hirahara, K. *et al.* Chirality correlation in double-wall carbon nanotubes as studied by electron diffraction. *Phys. Rev. B 73,* (2006).

19. Jiang, H., Nasibulin, A. G., Brown, D. P., and Kauppinen, E. I. Unambiguous atomic structural determination of single-walled carbon nanotubes by electron diffraction. *Carbon 45,* 662-667 (2007).

20. Liu, K. H. *et al.* Direct determination of atomic structure of large-indexed carbon nanotubes by electron diffraction: Application to double-walled nanotubes. *J. Phys. D: Appl. Phys.* *42,* (2009).

21. Sfeir, M. Y. *et al.* Probing electronic transitions in individual carbon nanotubes by Rayleigh scattering. *Science 306,* 1540-1543 (2004).

22. Sfeir, M. Y. *et al.* Optical spectroscopy of individual single-walled carbon nanotubes of defined chiral structure. *Science 312,* 554-556 (2006).

23. Berciaud, S. *et al.* All-optical structure assignment of individual single-walled carbon nanotubes from Rayleigh and Raman scattering measurements. *Phys. Status Solidi B 249,* 2436-2441 (2012).

24. Berciaud, S. *et al.* Excitons and high-order optical transitions in individual carbon nanotubes: a Rayleigh scattering spectroscopy study. *Phys. Rev. B* **81,** (2010).

25. Saito, R., Dresselhaus, G., and Dresselhaus, M. S. Trigonal warping effect of carbon nanotubes. *Phys. Rev. B* **61,** 2981-2990 (2000).

26. Liu, K. H. *et al.* An atlas of carbon nanotube optical transitions. *Nature Nanotech.* **7,** 325-329 (2012).

27. Plentz, F. *et al.* Direct experimental evidence of exciton-phonon bound states in carbon nanotubes. *Phys. Rev. Lett.* **95,** (2005).

28. Lefebvre, J. and Finnie, P. Polarized photoluminescence excitation spectroscopy of single-walled carbon nanotubes. *Phys. Rev. Lett.* **98,** (2007).

29. Hertel, T. *et al.* Intersubband decay of 1-d exciton resonances in carbon nanotubes. *Nano Lett.* **8,** 87-91 (2008).

30. Lauret, J. S. *et al.* Ultrafast carrier dynamics in single-wall carbon nanotubes. *Phys. Rev. Lett.* **90,** (2003).

31. Koyama, T. *et al.* Ultrafast exciton energy transfer between nanoscale coaxial cylinders: intertube transfer and luminescence quenching in double-walled carbon nanotubes. *ACS Nano* **5,** 5881-5887 (2011).

32. Malic, E., Maultzsch, J., Reich, S., and Knorr, A. Excitonic Rayleigh scattering spectra of metallic single-walled carbon nanotubes. *Phys. Rev. B* **82,** (2010).

33. Spataru, C. D., Ismail-Beigi, S., Benedict, L. X., and Louie, S. G. Excitonic effects and optical spectra of single-walled carbon nanotubes. *Phys. Rev. Lett.* **92,** (2004).

34. Chang, E., Bussi, G., Ruini, A., and Molinari, E. Excitons in carbon nanotubes: An ab initio symmetry-based approach. *Phys. Rev. Lett.* **92,** (2004).

35. Kane, C. L. and Mele, E. J. Electron interactions and scaling relations for optical excitations in carbon nanotubes. *Phys. Rev. Lett.* **93,** (2004).

36. Luer, L. *et al.* Size and mobility of excitons in (6,5) carbon nanotubes. *Nature Phys.* **5,** 54-58 (2009).

37. Tomio, Y., Suzuura, H., and Ando, T. Interwall screening and excitons in double-wall carbon nanotubes. *Phys. Rev. B* **85,** (2012).

38. Ohno, Y. *et al.* Chirality-dependent environmental effects in photoluminescence of single-walled carbon nanotubes. *Phys. Rev. B* **73,** (2006).

39. Miyauchi, Y. *et al.* Dependence of exciton transition energy of single-walled carbon nanotubes on surrounding dielectric materials. *Chem. Phys. Lett.* **442,** 394-399 (2007).

40. Sato, K. *et al.* Discontinuity in the family pattern of single-wall carbon nanotubes. *Phys. Rev. B* **76,** (2007).

41. Wang, F. *et al.* Interactions between individual carbon nanotubes studied by Rayleigh scattering spectroscopy. *Phys. Rev. Lett.* **96,** (2006).

42. Liu, K. H. *et al.* van der Waals-coupled electronic states in incommensurate double-walled carbon nanotubes. *Nature Phys.* **10,** 737-742 (2014).

43. Koshino, M., Moon, P., and Son, Y. W. Incommensurate double-walled carbon nanotubes as one-dimensional moiré crystals. *Phys. Rev. B* **91,** (2015).

44. Moore, K. E., Tune, D. D., and Flavel, B. S. Double-walled carbon nanotube processing. *Adv. Mater.* **27,** 3105-3137 (2015).

Chapter 3 | Single- and few-layer metallic NbS$_2$: growth, optical identification and transport properties

3.1 Introduction

3.1.1 Superconductivity in 2D metals
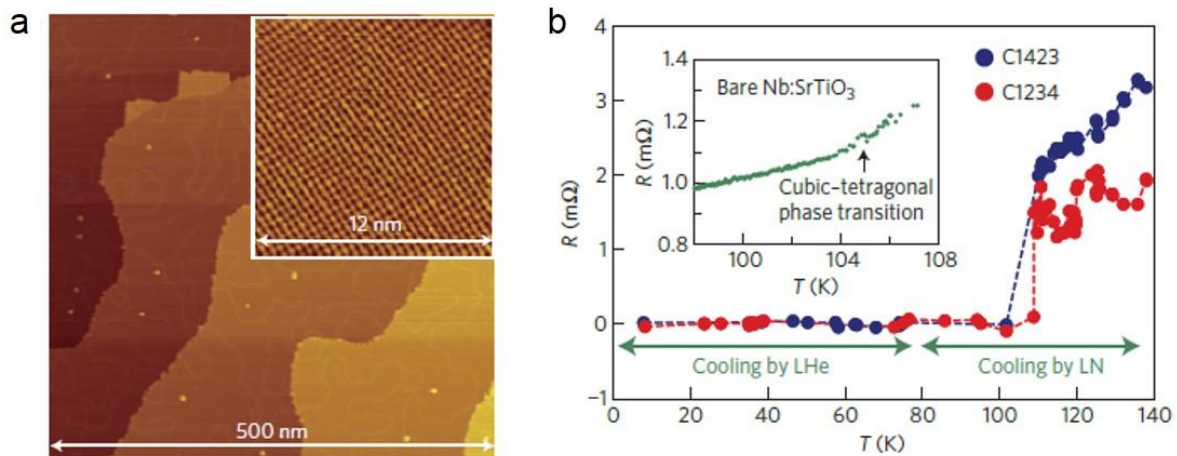
Figure 1. Superconductivity above 100 K of single-layer FeSe on doped SrTiO$_3$ substrate (adapted from ref.4). (a) Scanning tunneling microscope (STM) image of as-grown FeSe thin films on SrTiO$_3$ by molecular beam epitaxy (MBE). Inset shows a close-up view of single-layer FeSe. (b) Four-probe electrical measurement for a single-layer FeSe on SrTiO$_3$ showing a T_c that is higher than 100 K.

The recent discovery of superconductivity in two-dimensional (2D) systems has provided great research impacts in both communities of superconductivity and 2D materials[1-6]. The discovery has broken through the well-accepted idea that the 2D superconductivity has been considered to be susceptible to quantum fluctuations, expanding the research on superconductors to various 2D materials. In the case of 2D superconductors, the environmental effect is essential and the transition temperature T_c of 2D superconductors can be tuned via electrostatically gating the materials or by changing the underlying substrates[5-6], which enable one to achieve even higher T_c than that of bulk 3D materials. In fact, it has recently been reported that monolayer FeSe exhibits much higher T_c than that of the bulk

counterpart (**see Figure 1**), holding a great promise for pursuing high-temperature superconductivity in the realm of 2D layered materials[4].

3.1.2 Bottleneck: material preparation

The difficulty in sample preparation, however, has been a serious bottleneck for the studies of superconductivity in 2D systems. The exfoliation of metallic layered materials is the simplest and an important way to prepare 2D metallic materials. However, isolation of 2D metallic layers by the exfoliation has been limited to only a few reports[6-10]; the strong interlayer interaction that originates from metallic bonds is probably the reason for the difficulty in preparation of 2D metallic systems. This is in stark contrast to its successful applications to the preparation of various 2D semiconductors or insulators such as semiconducting transition metal dichalcogenides (TMDCs), black phosphorus, hexagonal boron nitride (hBN)[11-15]. A different preparation approach is, therefore, definitely required to extend the study of 2D superconductivity and to explore rich physics related to 2D superconductors.

3.1.3 Purpose of this work

The purpose of this work is to develop a controllable preparation method of 2D metallic layers. Our strategy to realize this is to use the bottom-up approach, *i.e.*, direct chemical vapor deposition (CVD) growth of 2D metallic layers. CVD has been demonstrated as a powerful methodology in preparation of semiconductor thin films and has been widely used to grow a wide variety of 2D layered materials and heterostructures in a controllable way[16-22]. One of the important characteristics of CVD growth is layer-number selectivity such that mono- to ultra-thin-layers of graphene[16], hBN[17], MoS_2[23], WS_2[24], *etc.* have successfully been grown by the CVD method. In contrast, the previous CVD syntheses of layered metallic materials are

limited, where the thickness of the materials grown is still large; 20 – 200 nm has been reported for NbS$_2$[25] and no successful growth of 2D metallic TMDCs (mono- to several-layer thickness) has been achieved so far.

3.2 Experimental
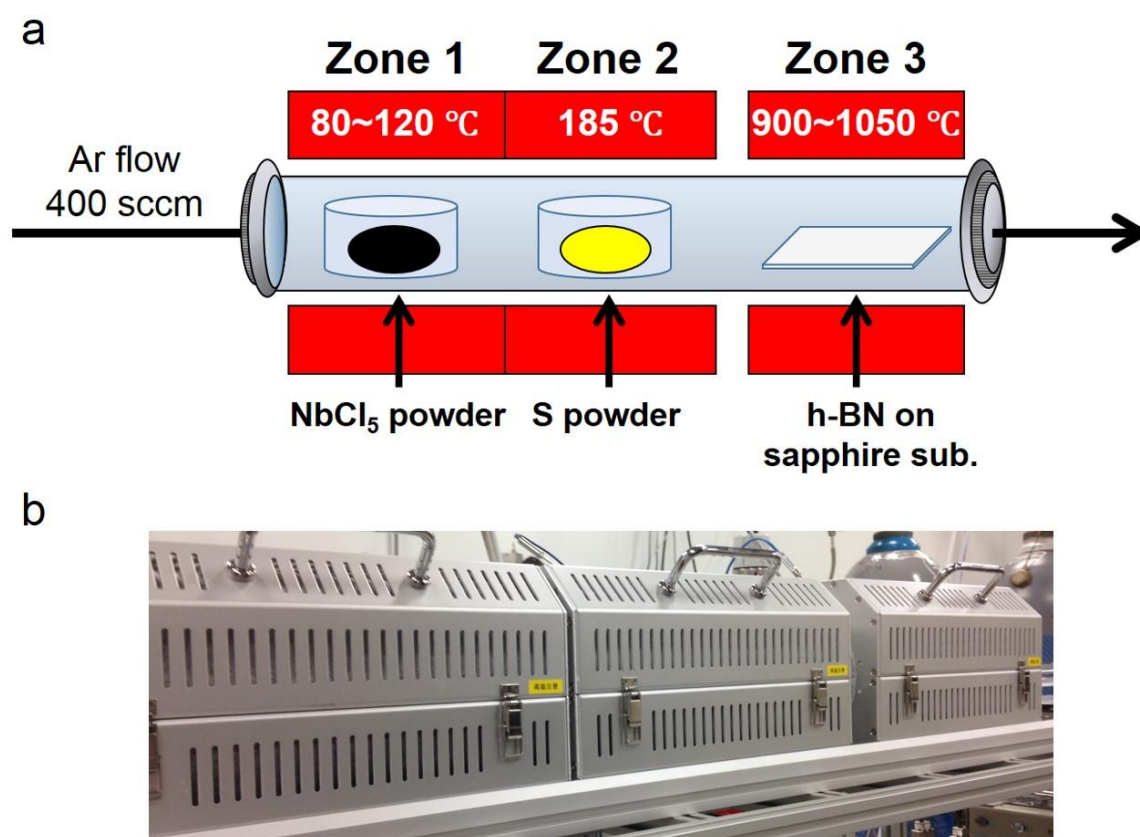
Figure 2. (a) Schematic for the triple-furnace CVD set-up. (b) A photo of the experimental set-up. Physical separation between zone 2 and hot zone 3 is kept to stabilize the central temperature in zone 2 (185 ℃) and thus the rate of sulfur supply.

Here, we have focused on CVD growth of NbS_2 atomic layers using the so-called triple (3)-furnace CVD method and hBN as substrates (**see figure 2**). NbS_2 is a member of layered metallic TMDCs, where Nb atoms are sandwiched by two layers of sulfur atoms showing trigonal prismatic structure. In-plane bonding between sulfur and Nb atoms is covalent in nature, whereas the interaction between adjacent layers (sulfur-sulfur) is non-covalent in nature. Superconductivity and charge-density-wave (CDW) phase have been found to exist in this material in bulk[26-27]. The 3-funace CVD method we developed enables us to control supply rate of Nb source and elemental sulfur independently, leading to achieve a fine tuning of reaction conditions to realize better control in the layer numbers of NbS_2[25]. Furthermore, the hBN substrate provides an atomically flat surface without dangling bonds, which facilitates

smooth diffusion of the sources to grow high quality NbS$_2$ flakes. In addition, hBN has proven to be one of the best substrates to investigate intrinsic properties of atomic layers[28-31], since extrinsic scatterings and unintentional doping are suppressed due to the hBN's atomically flat surface without dangling bonds and charged impurities.

3.3 Results

3.3.1 Successful growth of 2D NbS$_2$
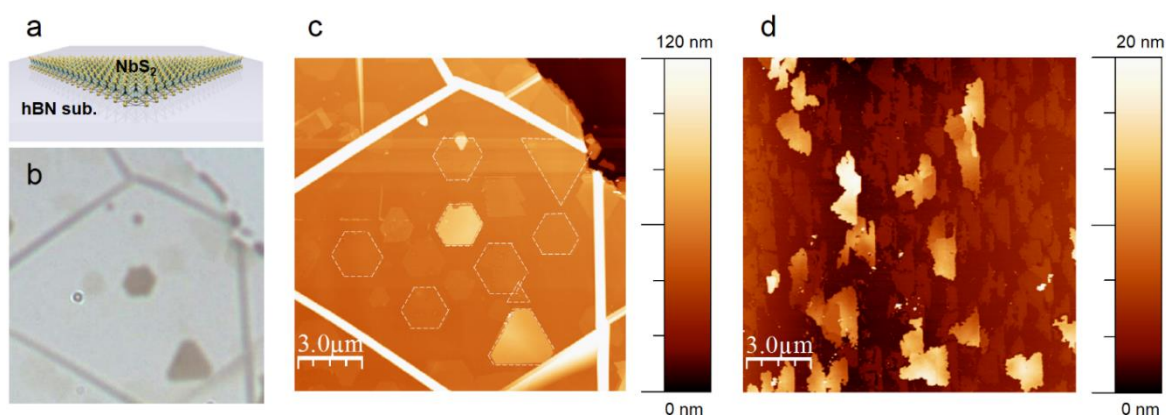
Figure 3. Direct growth of 2D NbS$_2$ atomic layers on top of hBN. (a) Structure schematic for NbS$_2$ atomic layers grown on hBN. (b) Optical transmission image of typical as-grown NbS$_2$ atomic layers on a hBN substrate deposited on a transparent sapphire substrate. (c) AFM topological image corresponding to the same place in (b). The contours of several NbS$_2$ samples are marked by white dashed lines for better eye identification of orientation matching between NbS$_2$ and underlying hBN. (d) Typical AFM topological image of as-grown NbS$_2$ flakes on top of sapphire for comparison with (c).

Figure 3a is a schematic of NbS$_2$ atomic layers grown on top of hBN substrates. The hBN substrates were prepared through the deposition of hBN flakes with the size typically of several tens of micrometers onto sapphire substrates by mechanical exfoliation. We adopted the 3-furnace CVD method where reaction precursors (NbCl$_5$ and elemental sulfur powders) and sapphire substrates are placed separately in each of the furnace along the direction of carrier gas flow (**see Figure 2a and see the growth details in the Methods**). The 3-furnace CVD method independently controls several growth parameters such as the supply rates of Nb and sulfur sources and growth temperature to achieve a better control in the growth of NbS$_2$. **Figures 3b** and **3c** show typical optical microscope and AFM topographical images, respectively, of as-grown NbS$_2$ atomic layers on top of a hBN substrate at low magnification. **Figure 3d** shows a typical AFM topographical image of NbS$_2$ grown directly on a sapphire substrate for comparison. The as-grown NbS$_2$ on top of hBN clearly shows well-faceted hexagonal or triangular shapes, whereas samples grown on sapphire possess irregular crystal

shapes; moreover, the typical domain size of individual NbS_2 flakes grown on hBN (2~3 μm) is much larger than those directly grown on sapphire due to a smaller nucleation density (**see Figure 3c and Figure 3d**). The observed substantial difference in crystal shapes clearly shows the importance of substrates in the CVD growth of NbS_2, which presumably originates from intrinsic surface properties of substrates[24-25].
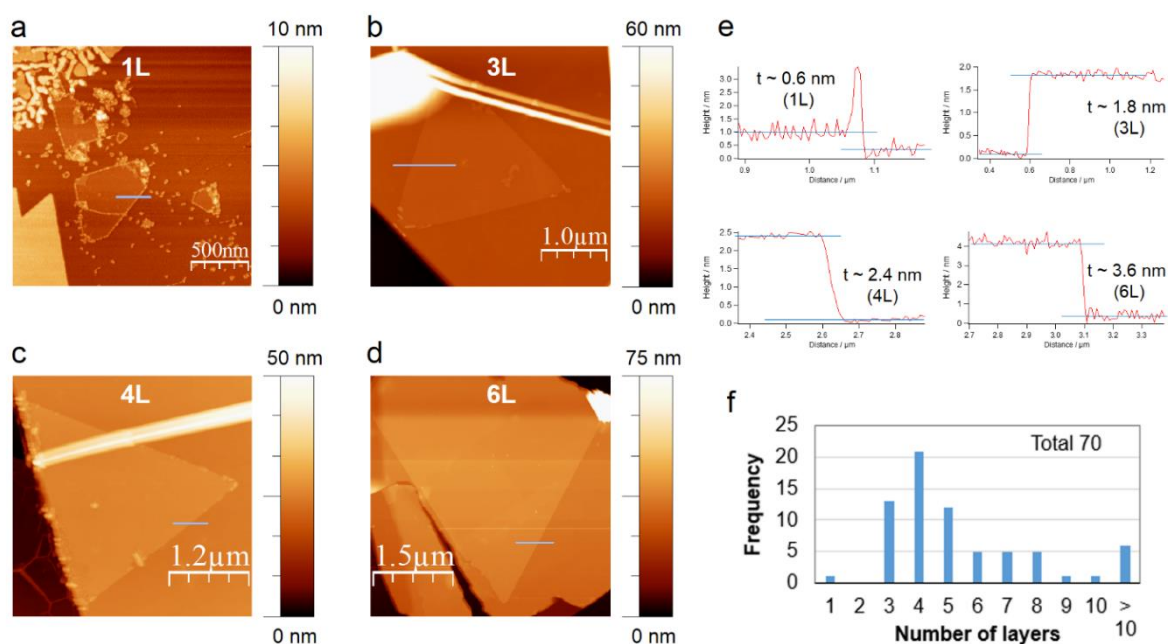
Figure 4. Representative AFM topological images of ultrathin individual NbS_2 atomic layers. (a-d) AFM topological images of monolayer, 3L, 4L and 6L NbS_2 samples, respectively. (e) Height profiles along the marked lines in the corresponding (a-d) in which ultraflat surface of NbS_2 originating from atomically-flat hBN substrate is clearly recognized. (f) Histogram of layer numbers of NbS_2 samples. Few-layer-thin samples (L ≤ 6) are preferentially grown (52/70).

Figures 4a-d show the representative AFM topographical images of individual NbS_2 flakes with different thickness. Very importantly, we have successfully achieved the growth of monolayer NbS_2 (**Figure 4a and see also Figure 5**); to the best of our knowledge, this is the first demonstration of the successful growth of monolayer metallic TMDCs based on bottom-up methodology. Four plots shown in **Figure 4e** correspond to the height profiles along the marked lines in **Figures 2a-d**, where ultra-flat surfaces of NbS_2 flakes are clearly recognized; the ultra-flat surface originates from the atomically-flat surface of hBN. Assuming
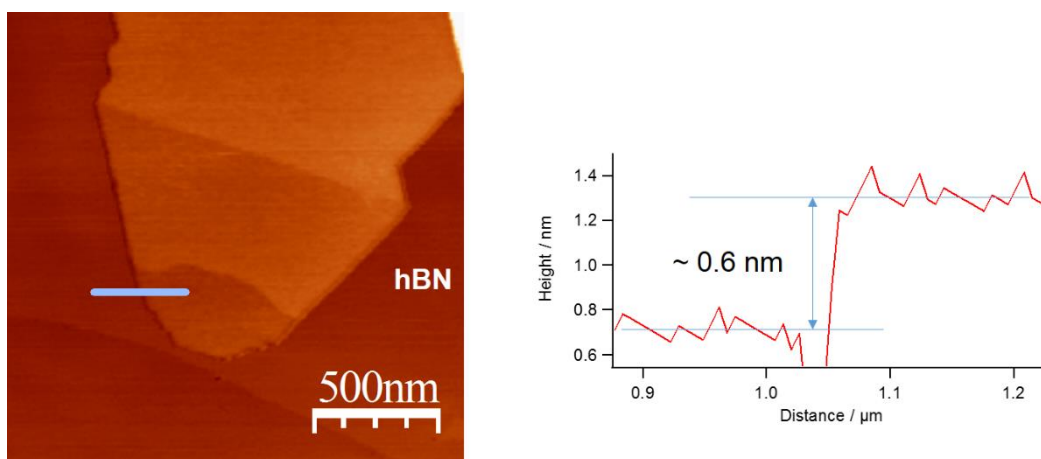
Figure 5. AFM image and height profile of monolayer NbS$_2$ grown by the developed CVD.

the interlayer distance is ca. 0.6 nm[25], we have unambiguously determined the layer numbers to be 1L, 3L, 4L and 6L for **Figures 4a-d**, respectively. **Figure 4f** shows a histogram of layer numbers of NbS$_2$ grown, which clearly indicates that few-layer-thin flakes (≤6) are preferentially grown (52/70) on hBN. Important to note is that no detectable chlorine is present in our as-grown samples as shown in our X-ray photoelectron spectroscopy (XPS) data in **Figure 6**, which indicates that all the chlorine is gone after high-temperature growth.
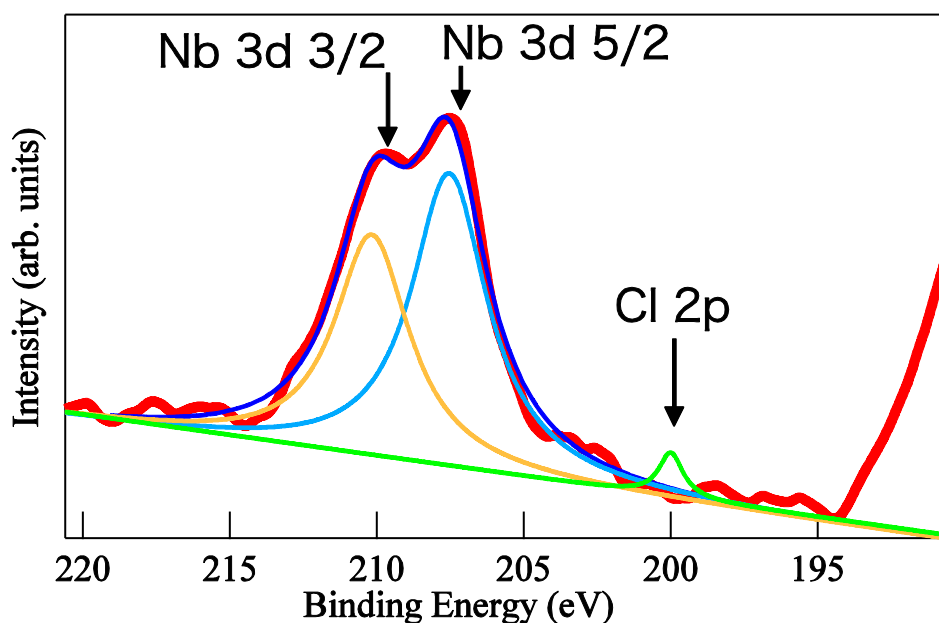
Figure 6. X-ray photoelectron spectroscopy (XPS) characterization on as-grown NbS$_2$ samples grown on hBN deposited on sapphire. No detectable chlorine (Cl 2p) is found meaning that no Cl-containing impurities remains in the samples.

It should be noted that we can grow not only individual crystals but also continuous films of NbS_2 by our CVD method (**see Figure 7**). In principle, individual crystals can grow to merge each other to form continuous films of NbS_2 under a proper growth condition. We have investigated several different growth conditions and successfully grown continuous films of NbS_2. The SEM images shown in **Figure 7** are continuous films of NbS_2, where a continuous NbS_2 gives the dark contrast on top of hBN. **Figure 7a** shows hBN flakes that are fully covered by NbS_2, and **Figure 7b** shows hBN flakes partially covered and fully covered by NbS_2. As shown in the images, the only limiting factor for the size of the continuous film is the size of underlying substrates, which clearly shows the possibility of growth of large-area NbS_2.
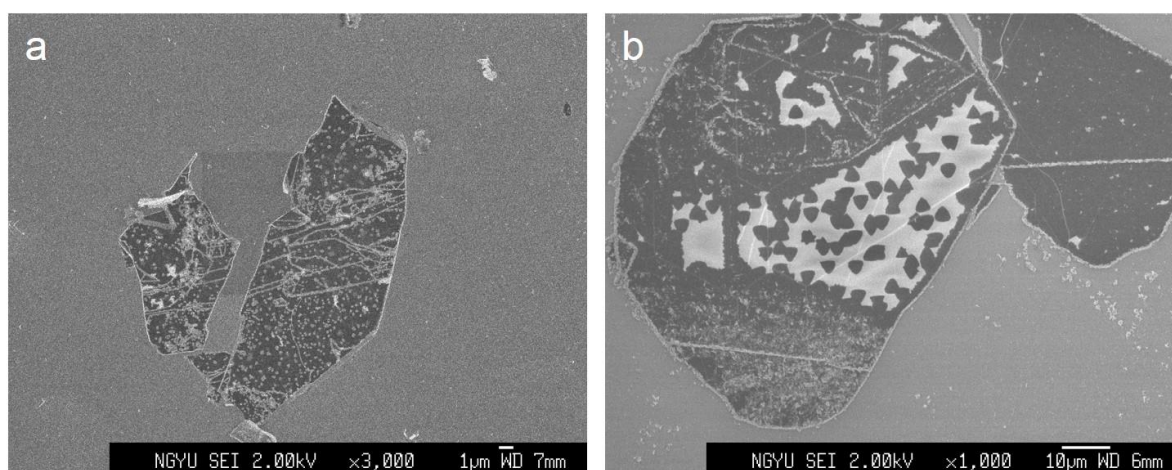
Figure 7. (a-b) SEM images showing the successful growth of NbS_2 continuous film by using the developed CVD under proper growth conditions.

3.3.2 TEM characterizations on as-grown NbS_2

Sample characterizations by transmission electron microscopy (TEM) could offer rich microscopic information on the structures and spectroscopic information on the material compositions compatible with high spatial resolution. We have directly transferred the NbS_2/hBN onto TEM-compatible grid (**see details in Methods**) prior to the TEM observations[32]. **Figures 8a-c** show the typical TEM images of our as-grown NbS_2 samples.
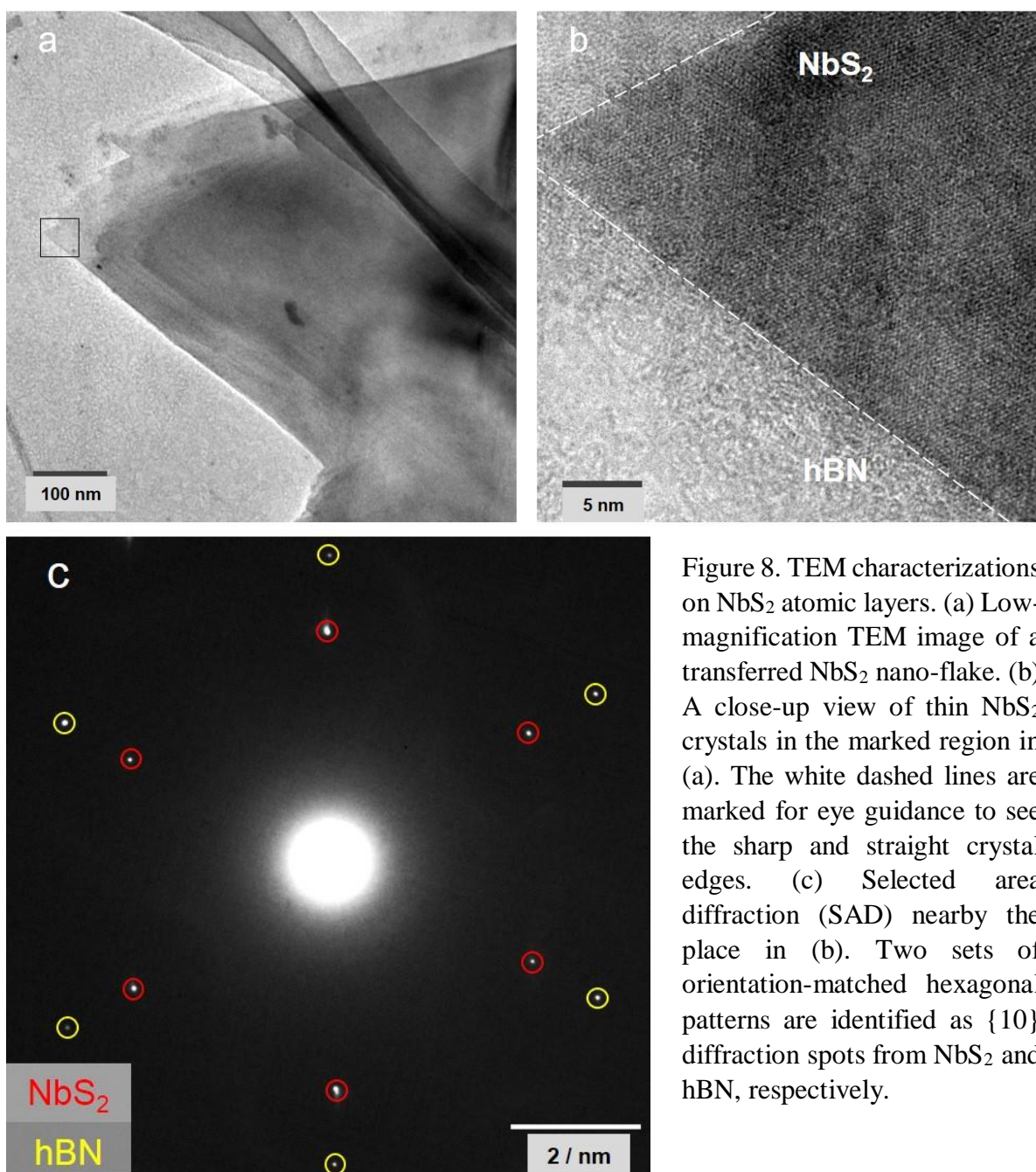
Figure 8. TEM characterizations on NbS_2 atomic layers. (a) Low-magnification TEM image of a transferred NbS_2 nano-flake. (b) A close-up view of thin NbS_2 crystals in the marked region in (a). The white dashed lines are marked for eye guidance to see the sharp and straight crystal edges. (c) Selected area diffraction (SAD) nearby the place in (b). Two sets of orientation-matched hexagonal patterns are identified as {10} diffraction spots from NbS_2 and hBN, respectively.

Figure 8b is a close-up image of marked region in **Figure 8a**, where the NbS_2 samples show sharp liner edges indicated by the white dashed lines. **Figure 8c** shows the selected area diffraction (SAD) pattern nearby place in **Figure 8b**. The electron diffraction pattern clearly shows two sets of orientation-matched hexagonal patterns, which arise from NbS_2 and hBN, respectively (diffraction spots originating from {10} planes of hBN and NbS_2 are marked by circles in the figure).
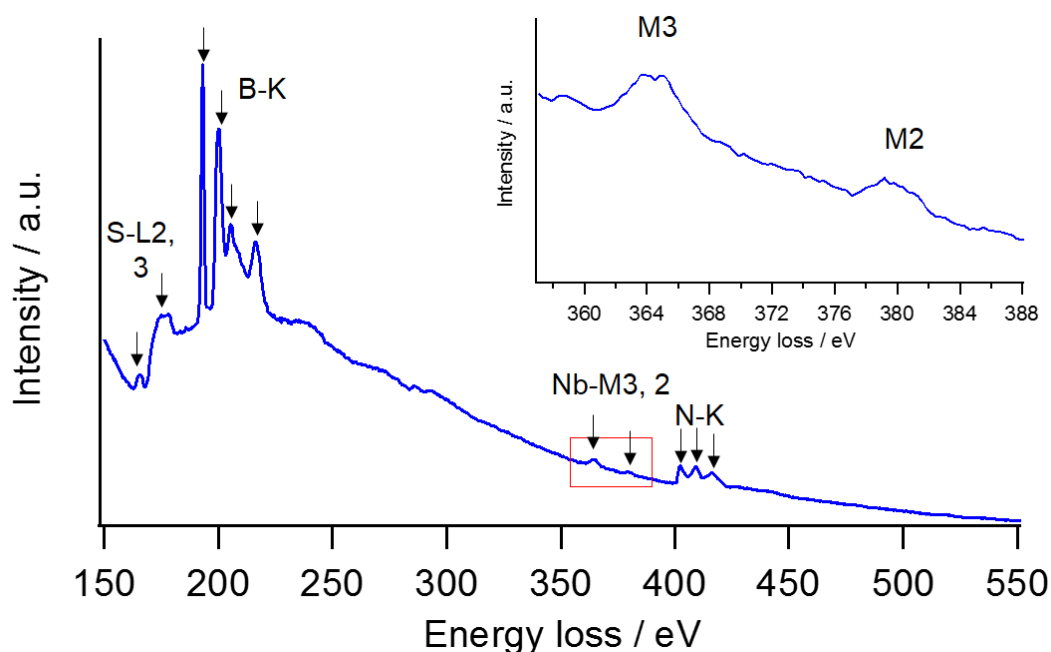
Figure 9. EELS spectrum at the same place where the SAD diffraction pattern was taken (shown in Figure 8c). Sharp peaks from boron, nitogen, niobium and sulfur are identified and donated. Inset shows the close-up spctrum at the spectral region marked by the red rectangular frame.

Figure 9 shows the corresponding electron energy loss spectroscopy (EELS) spectrum, where sharp peaks from boron, nitrogen, niobium and sulfur are clearly identified. More data pertaining to TEM characterizations are displayed in **Figure 10**.
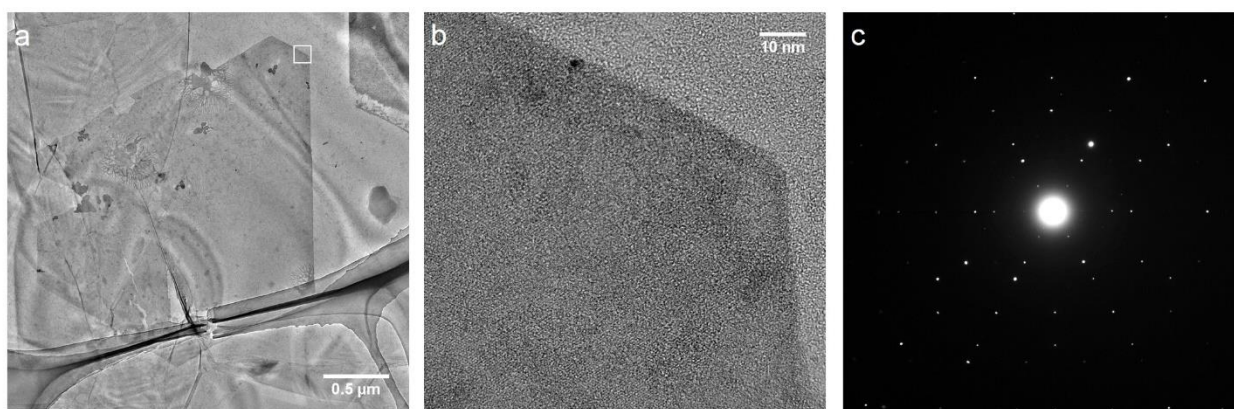
Figure 10. More data pertaining to TEM characterizations on NbS_2 atomic layers. (b) is a close-up view of marked region in (a). (c) shows the corresponding SAD pattern nearby the place in (b).

3.3.3 Thickness identification by optical transmission
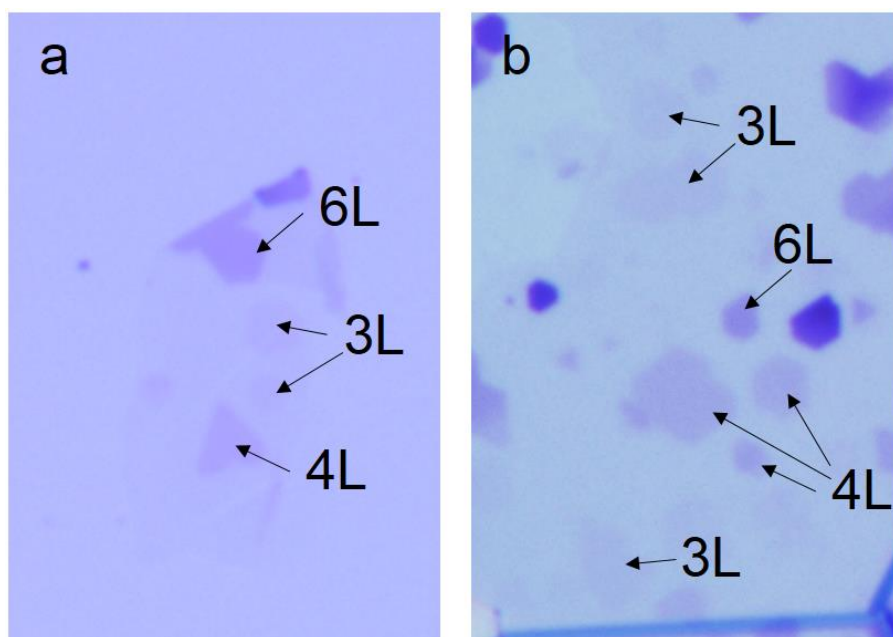
Figure 11. Facile method for layer-number-characterization of NbS_2 atomic layers using optical transmission microscopy. (a) and (b) are two typical optical transmission images of as-grown NbS_2 samples on hBN deposited on sapphire substrates. A shortpass edge filter (< 575nm) is employed to collect transmitted light to form optical images. Layer numbers indicated in the figures are observed by AFM.

We have developed a facile layer-number-characterization method using optical microscopy. Owing to the strong light-matter interaction in TMDC atomic layers, optical absorption at visible range is huge[33-35]; the absorption coefficient for both semiconducting TMDCs and metallic TMDCs are found to be in the order of 10^8 m^{-1} in the visible range (frequency-dependence)[33-34]. TMDC atomic layers should, therefore, show strong layer-number dependence in optical contrast in optical transmission images, which can be directly correlated to sample thickness[8].

Figures 11a and **11b** are two typical optical transmission images of as-grown NbS_2 samples on top of hBN deposited on sapphire substrates; the number of layers shown in the figures is determined by AFM observations. We use broadband white light to illuminate NbS_2 samples from the backside of underlying sapphire substrates, and the transmitted light with wavelength shorter than 575 nm is used to form the optical contrasts (**see details in the**

Methods). NbS$_2$ has strong light absorption at the blue visible region[36], and using the wavelength shorter than 575 nm contributes to the improvement of optical contrasts. Since both the sapphire and hBN substrates are transparent over the whole visible range, optical contrasts obtained mainly originate from the optical absorption of NbS$_2$ flakes. The straightforward relation between optical contrasts and absorption of NbS$_2$ leads to simpler interpretation for distinguishing flakes with differing thickness as compared to previous work using reflected light from samples deposited on opaque SiO$_2$/Si substrates[8]. As shown in **Figs. 11a** and **11b**, optical contrasts of NbS$_2$ in optical transmission images indeed show a strong layer-number dependence, that is, with increasing layer number NbS$_2$ absorbs more light (< 575 nm) and thus gives darker contrasts. As shown in the images, ultrathin NbS$_2$ atomic layers down to 3L have been successfully virtualized using this simple technique. Contrasts from NbS$_2$ atomic layers with same thickness are almost identical, which provides a rapid and reliable optical method for thickness identification of ultra-thin NbS$_2$.

3.3.4 Layer-number-dependent Raman spectroscopy

The present NbS$_2$ atomic layers (except for the monolayer) are all in the 3R-phase as shown by Raman spectroscopy in **Figure 12**. Raman spectroscopy has been regarded as a reliable technique to identify NbS$_2$ bulk samples and their phases (2H or 3R)[37]. Except for the layer-number dependent shifts in the observed Raman bands, the general features of Raman spectra of the current samples are in excellent agreement with the previous 3R-NbS$_2$ spectra of bulk samples[25,37]. All of the four first-order Raman-active vibrational modes E_1, E_2, A_1 and A_2 together with the two pronounced peaks between $100 \sim 200\ cm^{-1}$ appear at expected frequencies in the samples regardless of layer numbers. Based on the group theory point of view, the first-order (zone center phonon) Raman-active modes in 3R-phase (space group C_{3v}^5) are E_1, E_2, A_1
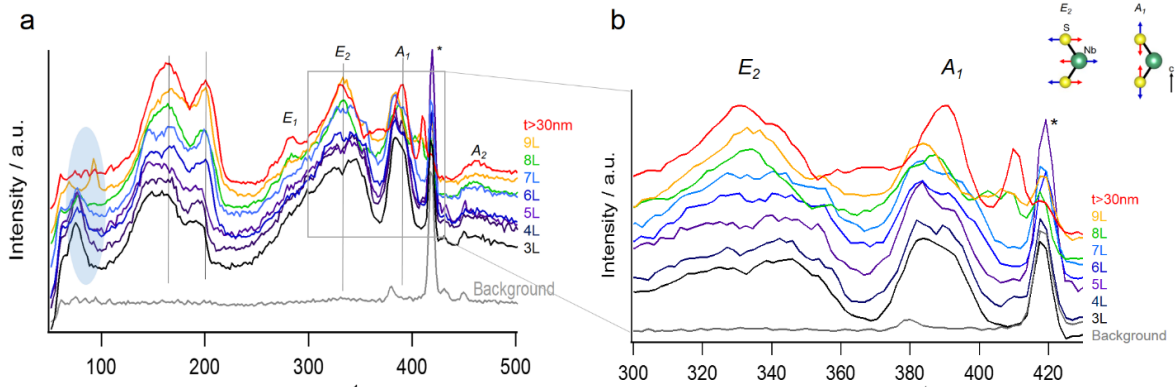
Figure 12. Layer-number dependent Raman spectra of NbS_2 atomic layers. (a) Layer-number dependent Raman spectra of NbS_2 samples over 50 cm^{-1} to 500 cm^{-1}. All the Raman spectra are normalized to yield the same intensity for peaks locating at $\sim$ 160 cm^{-1} and vertical shifts are made for ease of comparison. Grey spectrum shows the sapphire background under the same measuring condition in which * mark one of its strongest peaks. Vertical lines are shown for the identification of the peak shifts. E_1, E_2, A_1 and A_2 are the four first-order Raman vibrational modes for $3R$-NbS_2. Peaks locating at $\sim$ 160 cm^{-1} and $\sim$ 200 cm^{-1} originate from two-phonon scattering processes. Shading area shows the presence of new peaks at low frequency region that are absent in bulk samples. (b) A close-up view of Raman spectra for the framed region in (a). Spectra are normalized to yield the same intensity for the peak tops of E_2. Inset is a schematic illustration of E_2 (in-plane) and A_1 (out-of-plane) vibrational modes.

and A_2 vibration modes, which serves as the unique identity for $3R$-NbS_2 that is distinct from that in $2H$-NbS_2 in the characterization by Raman spectroscopy. In the present study, one of the thinnest $3R$-NbS_2, *i.e.*, 3L $3R$-NbS_2, has been synthesized, exhibiting strong Raman signals for the first time (**see Figure 4b and corresponding height profile in Figure 4e**). Monolayer sample in **Figs. 4a** and **5**, however, did not show any Raman signals possibly due to oxidation-induced sample degradations.

Figure 12a shows the layer-number dependent Raman spectra of NbS_2 samples. All the spectra are normalized to yield the same intensity for the peaks at $\sim$ 160 cm^{-1} and the spectra are also vertically shifted for the clarity of comparison. Inset in **Figure 12b** shows the schematic illustration of two of the four Raman-active vibration modes in $3R$-NbS_2, E_2 and A_1, which are associated with the in-plane and out-of-plane vibrations, respectively. **Figure 12b** shows a close-up view of Raman spectra in the framed region in **Figure 12a**, in which spectra

are normalized to yield the same intensity for peak tops of E_2 mode. As seen in **Figure 12b**, the E_2 and A_1 modes in 3R-NbS$_2$ exhibits respective phonon softening and stiffening upon increasing layer numbers, which are similar to the reported peak evolution of E^1_{2g} and A_{1g} in semiconducting TMDCs[38-39]; the peak shifts are caused by the influence of adjacent layers on the effective restoring forces, and also by the increase in dielectric screening of long-range Coulomb interactions upon adding more layers[40].
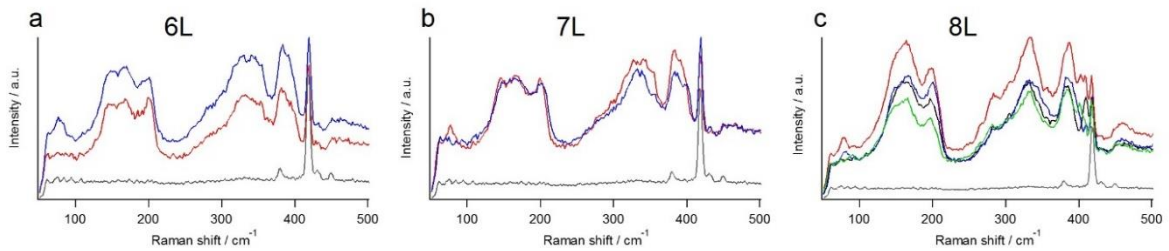
Figure 13. Identical Raman spectra for NbS$_2$ atomic layers with different thickness (6L in (a), 7L in (b) and 8L in (c)), demonstrating good reproducibility in the growth and optical characterizations.

In addition to the first-order Raman process (Γ phonons), the two pronounced peaks at ~160 cm^{-1} and ~ 200 cm^{-1} also show strong layer-number dependence. For thin samples (< 10L), we have observed strong peaks locating between 50 cm^{-1} and 100 cm^{-1} (**see Figure 12a**), which have never been observed in bulk 3R-NbS$_2$ (see the red spectrum and refs. 25 and 37). The Raman spectra obtained for different NbS$_2$ atomic layers with same thickness are almost identical, confirming good reproducibility in the growth and optical characterizations (**see Figure 13**).

3.4 Discussion

3.4.1 NbS$_2$ growth: substrate effect and mechanism

Substrate effect is essential for the successful growth of monolayer and ultra-thin NbS$_2$. As clearly shown in **Figures 3c** and **3d**, there is a significant difference in size, shape and thickness between NbS$_2$ grown on hBN and sapphire; ultra-thin NbS$_2$ with well-defined shape forms only on hBN. Evidently, the choice of the substrate plays an important role in the successful growth of ultrathin NbS$_2$, suggesting that ultrathin NbS$_2$ on hBN grows through a different growth mechanism from NbS$_2$ on sapphire.

The growth of NbS$_2$ on hBN is most probably subject to the Frank van der Merwe (FM) mechanism, in which small ultrathin nuclei form first followed by further growth of ultrathin NbS$_2$ via in-plane growth[41] (**see schematic in Figure 14**). The growth of 2D crystals via the FM mechanism appears when the lattice mismatch between a 2D crystal and a substrate is small, which is not the case for the

Figure 14. Representative schematics showing the growth mode of 2D NbS$_2$ following the Frank van der Merwe (FM) mechanism.

NbS$_2$ growth onto hBN (lattice constants of NbS$_2$ and hBN are 3.33 and 2.51 angstrom, respectively). The FM mechanism is, however, possible in our case because interaction between NbS$_2$ and hBN originates from van der Waals force (not via chemical bonding), which does not require the small lattice mismatch. The formation of ultrathin NbS$_2$ via the FM mode is promoted by rapid supply of Nb and sulfur atoms to bare edges of NbS$_2$ nuclei, and the rapid

diffusion of Nb and sulfur atoms is realized by the ultraflat surface of hBN. The surface of the current hBN (prepared by mechanical exfoliation of single crystals) is atomically flat and does not have any serious dangling bonds, which ensures a small energy barrier for surface diffusion. When the surface diffusion of Nb and sulfur is fast enough, the rate-determining step in NbS_2 growth would be the reaction at edges of nuclei, which results in formation of well-faceted ultrathin NbS_2 crystals (**as shown in Figure 3c and Figures 4a-d**).

In contrast, surface roughness and dangling bonds of sapphire cause large diffusion barrier, which leads to slower diffusion of Nb and sulfur; this results in the formation of NbS_2 with disordered shapes via vertical growths rather than the in-plane growth. Nucleation density should be suppressed in growth on hBN as compared with that on sapphire, resulting in a larger NbS_2 domain size (**Figs. 3c and 3d**). As clearly seen in **Figs 3b** and **3c**, NbS_2 atomic layers grown on hBN show orientational ordering (contours of several NbS_2 atomic layers are displayed in **Fig. 3c**). The observation of the orientational ordering strongly suggests that there is a relation in crystallographic orientation between NbS_2 grown and underlying hBN, indicating an epitaxial growth similar to the reported direct growth of graphene and monolayer WS_2 on hBN[42,43]. We have confirmed the epitaxial growth by electron diffraction (**Figs. 8c and 10c**). The orientations of the two hexagonal patterns perfectly match each other, showing the strict relation in crystallographic orientation between NbS_2 and hBN, namely the epitaxial growth. The observed epitaxial growth clearly demonstrates that NbS_2 crystals feel "potential" of hBN, and the interface between NbS_2 and hBN should be very clean.

3.4.2 Raman spectra

Successful growth of ultrathin NbS_2 enables us to investigate their optical and electronic properties. As shown in **Figure 12a**, layer-number dependence in Raman shift of

E_2 mode ($\sim$ 10 cm^{-1}) is larger than those found in semiconducting TMDCs (*e.g.*, MoS$_2$[38] and WS$_2$[39]) in which the E^1_{2g} Raman mode softens by $\sim$ 2 cm^{-1} with increasing the number of layers. Similarly large shift of E^1_{2g} Raman mode was also reported for metallic 2H-NbSe$_2$ prepared by mechanical exfoliation technique, being consistent with our results[44]. We think that the larger dielectric screening
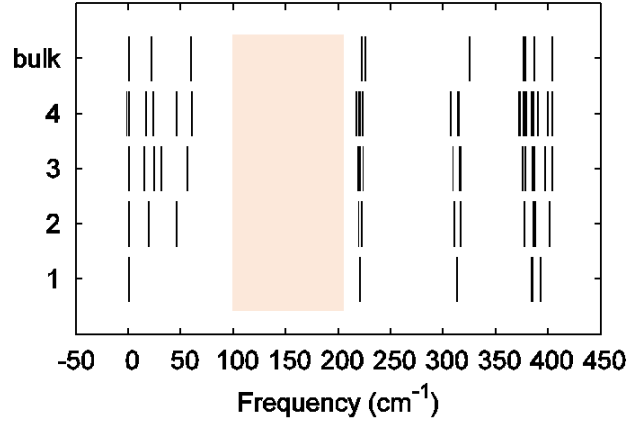
Figure 15. Calculated frequency for zone-center (Γ) phonons. There are no Raman bands between 100 cm^{-1} and 200 cm^{-1}, confirming that the two prominent Raman bands at $\sim$ 160 cm^{-1} and $\sim$ 200 cm^{-1} are from high-order Raman processes.

(larger dielectric tensors) of long-range Coulomb interactions present in metallic NbS$_2$ is the origin of this large layer-number-dependent shift[38]. The origin of Raman bands at $\sim$ 160 cm^{-1} and $\sim$ 200 cm^{-1} has been tentatively identified as two-phonon scattering processes[35]. Our theoretical calculation results (**see Figure 15 and the calculation details in Methods**) of
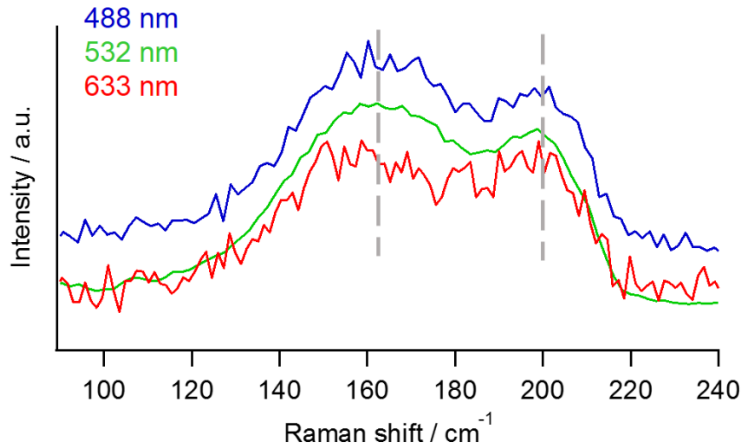
Figure 16. Investigation on the origin of the two strong peaks at 160 cm^{-1} and 200 cm^{-1} by Raman spectroscopy by using different laser excitations. Samples are thick NbS$_2$ prepared by mechanical exfoliation. We do not observe peak shifts for spectra excited by lasers with different energies (eye guidance by the dashed grey lines).

phonon frequencies at Γ point for 3R-NbS$_2$ show that these two pronounced peaks are not from first-order (Γ phonons) Raman process, regardless of layer numbers. This implies that those peaks should result from higher-order Raman processes, for example, double-resonant Raman scatterings. For linear electronic and phonon dispersion, Raman peaks shift in line with the

increase or decrease of the laser excitation energies. However, we do not observe such peak shifts (**see Figure 16**) in NbS$_2$ bulk samples where electronic and phonon dispersion are more complicated. The physical origin of those two pronounced peaks present in 3R-NbS$_2$ is still not very clear.

3.4.3 Electrical transport properties
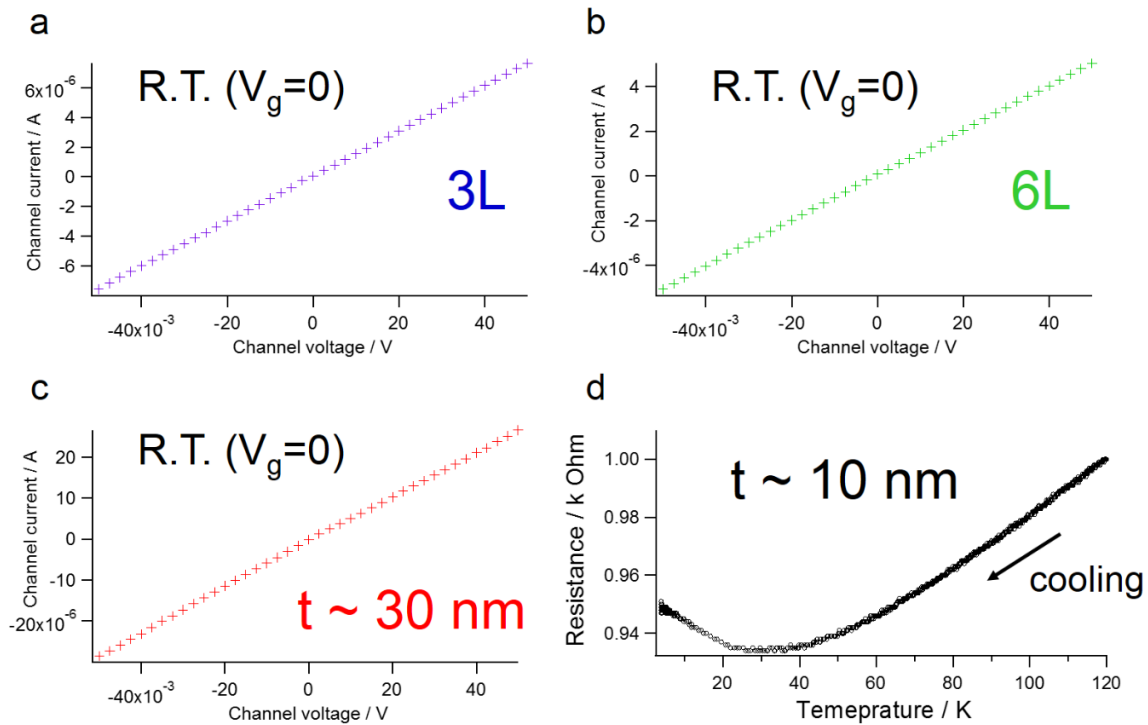
Figure 17. Transport properties of 3R-NbS$_2$ atomic layers. (a-c) *I/V* characteristics for 3L, 6L and ~ 30 nm NbS$_2$ samples measured at room temperature at 0 backgate voltage. Linear curves shown in all the three devices demonstrate the Ohmic-type contacts formed and the metallic channels of NbS$_2$ atomic layers. (d) Temperature dependence in resistance for a 10 nm NbS$_2$ sample. Linear decrease in resistance with decrease in temperature indicates a phonon-limited metallic transport behavior. Interestingly, a resistivity minimum at ~ 30K is observed showing a much higher transition temperature than that reported in bulk 3R-NbS$_2$. This enhancement in transition temperature is presumably due to enhanced electron-electron interaction in low-dimensional systems.

Two-probe microscopic devices are fabricated by the standard electron beam lithography (EBL) followed by subsequent metal electrode deposition of Cr and Au (**see details**

in Methods). **Figures 17a-c** shows the respective *I/V* characteristics of 3L, 6L and t ~ 30 nm

as-grown NbS_2 samples measured at room temperature (cf. the corresponding AFM

topographical images, Raman spectra and optical images of fabricated devices in **Figure 18**).

As clearly demonstrated, all *I/V* curves are linear, meaning that all NbS_2 devices (3, 6 layers
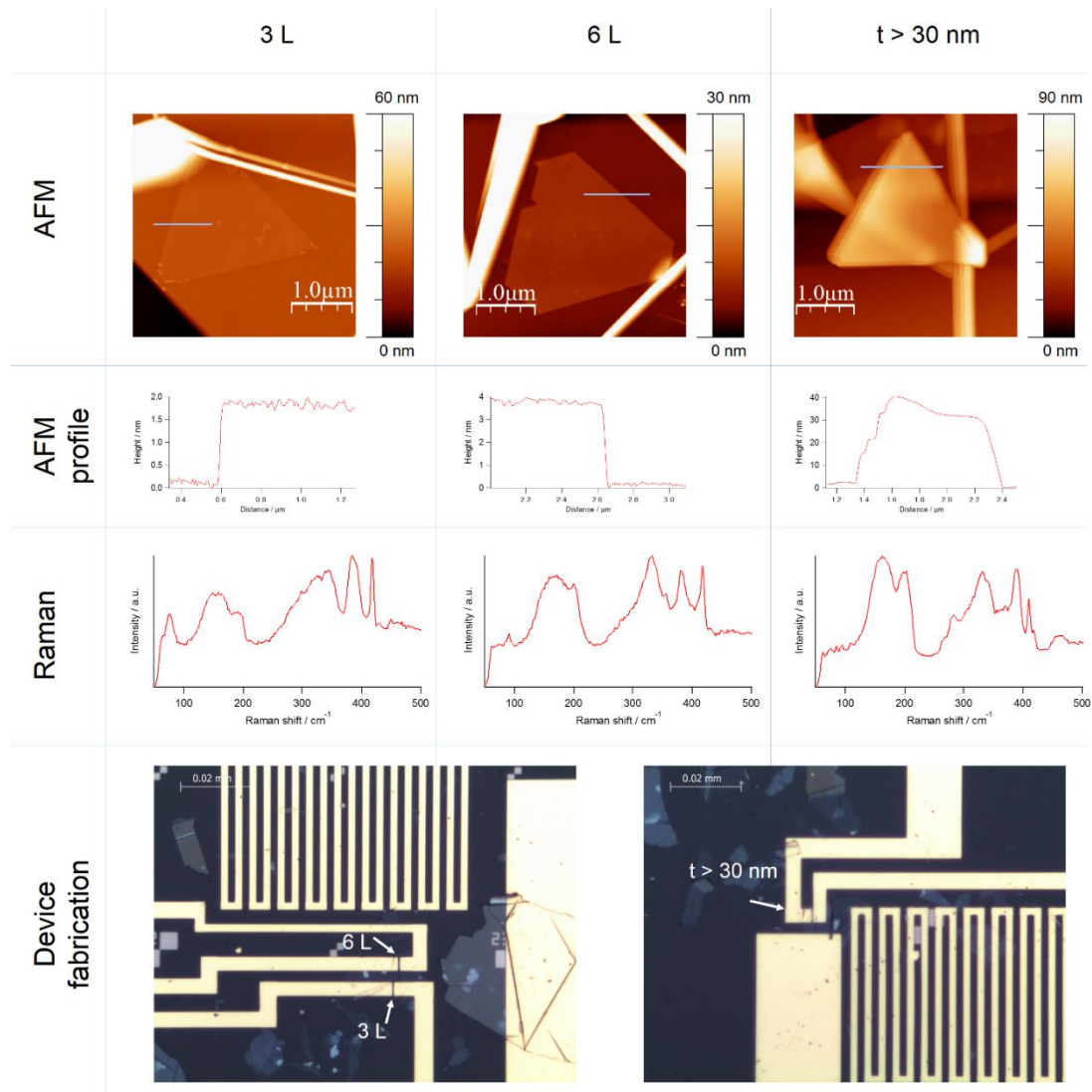
Figure 18. Corresponding AFM topographical images, Raman spectra and optical images of fabricated devices shown in Figs. 17.

and 30 nm-thick NbS_2) have Ohmic contacts with metallic channels. This is consistent with

the metallic ground state of NbS_2 as shown by a DFT calculation[45]. The conductivity calculated

from the corresponding *I/V* curves, and from the detailed device geometry for the three devices

are all around 100 $\Omega^{-1} \cdot cm^{-1}$ (168, 58 and 61 $\Omega^{-1} \cdot cm^{-1}$, respectively) similar to the reported thick

NbS$_2$ flakes (> 100 nm) prepared by mechanical exfoliation[46]. The metallic nature of few-layer-thin 3R-NbS$_2$ is also supported by no detectable photoluminescence (**see Figure 19 for 4L, 6L and 8L NbS$_2$**).
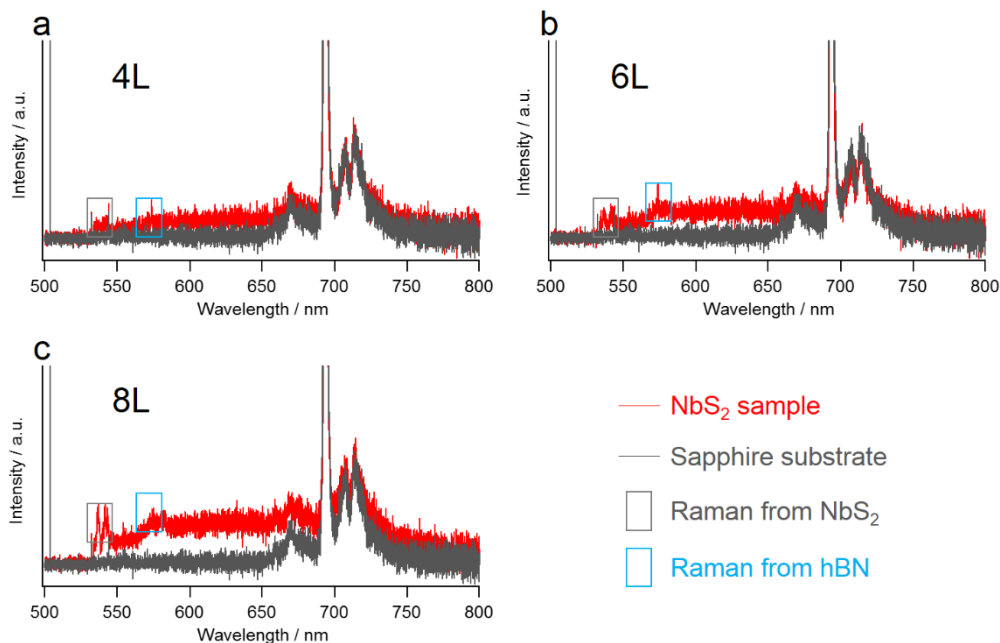
Figure 19. Photoluminescence measurements on 4L, 6L and 8L NbS$_2$ nanoflakes. As shown in the figures, no photoluminescence was observed in all these NbS$_2$ atomic layers over 500 nm ~ 800 nm, further supporting the metallic nature of NbS$_2$. Peaks present in the spectra can be identified as sapphire background, Raman peaks from NbS$_2$ and Raman peaks from hBN as donated.

The metallic behavior of ultrathin NbS$_2$ shown here is different from the previous work reporting that thin NbS$_2$ nanoflakes are semiconductor, where the presence of defects and trap surface states are believed to be the reasons for the semiconducting behavior[46]. The precise evaluation of quality (number of defects, trap surface states) is not straightforward, and it is, in principle, possible that the trap surface states lower down the electron concentration and conductivity. A large amount of the trap surface state, however, is needed to practically lower down electron density to affect conductivity because NbS$_2$ possesses a large amount of free carriers (1 electron / unit cell, much larger amount than that of doped-semiconductors); the large number of free carriers can be confirmed by our gate-dependent transfer data (as shown in **Figure 20**), where the gate-voltage independence of electrical conductivity shows the

characteristic metallic behavior with large number of free carriers. The preparation of the high-quality NbS_2 samples realized by the controllable CVD method with the 3-furnace set-up, together with the usage of the high-quality hBN substrates, can lead us to the successful observation of the intrinsic metallic nature of ultrathin NbS_2.
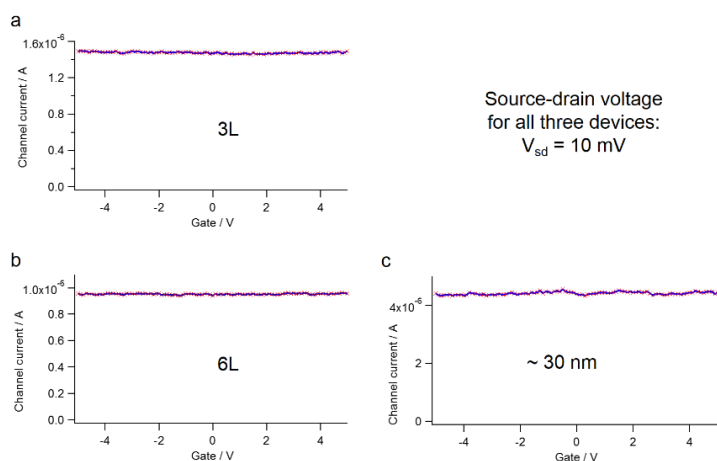
Figure 20. Transfer data (gate-voltage dependence) for 3L (a), 6L (b) and ~ 30 nm (c) NbS_2 nanoflakes measured at room temperature. The gate-independence results confirmed the typical metallic transport characteristics, that is, the existence of large amount of carriers near Fermi level.

Figure 17d shows the temperature dependence in resistance of NbS_2 with a thickness of 10 nm. As seen in **Figure 17d**, in the temperature range above ~ 30 K, the decrease in resistivity is linearly proportional to the decrease in temperature, indicative of a phonon-limited metallic transport. Interestingly, we observed a resistivity minimum T_m at ~ 30 K, which is much higher than what has been observed in bulk 3R-NbS_2 samples[47]. The higher T_m observed in the thin NbS_2 is presumably due to the electron-electron interaction enhanced in low-dimensional systems[48]. Other probable origins accounting for the resistivity minimum in 3R-NbS_2 are the Kondo effect[49] and weak localization[50]. Further detailed studies including magneto-transport experiments are needed to address these interesting issues.

3.5 Conclusions

To conclude, we have developed a CVD methodology for controllable growth of ultrathin metallic 3R-NbS$_2$, which is the first successful demonstration of growth of 2D metallic TMDCs. The key to the successful growth of ultrathin NbS$_2$ can be summarized by the following two factors: (1) the precise tuning of growth conditions using the 3-funace CVD method and (2) the utilization of atomically flat hBN as growth substrates. Using the CVD technique, the monolayer NbS$_2$ and thinnest 3R-NbS$_2$ (3L) have been synthesized for the first time. Raman spectroscopy and optical transmission imaging are performed for the detailed optical characterization of 2D NbS$_2$, providing the basis for layer-number-dependent structure identification. The crystallographic orientation matching between NbS$_2$ and hBN substrates revealed from electron diffraction patterns clearly shows an epitaxial growth mechanism for 2D NbS$_2$ growth on hBN with a very clean interface. The transport measurements on thin-layered 3R-NbS$_2$ with different thickness show that 3R-NbS$_2$ with thickness down to 2D limit is still metal, being consistent with DFT-based calculations. The synthetic methodology developed here can also be applied to the growth of many other 2D layered metallic systems, and thus offers new fundamental and technological pathways for the research of metallic 2D systems, which may lead to finding novel 2D superconductors.

3.6 Methods

Growth of NbS$_2$ atomic layers

hBN substrates were deposited onto clean sapphire substrate by mechanical exfoliation using Nitto tape 31B[51]. Prior to the CVD growth, sapphire substrates with deposited hBN were annealed in air at 700 ^{0}C for 30 min to remove tape residues. Three-furnace CVD approach was adopted where Nb source (NbCl$_5$ powders, Alfa Aesaer, purity 99.95 %), elementary sulfur (powders, Aldrich, purity 99.98 %) and sapphire substrates lined up themselves in each furnaces along the direction of the carrier gas flow (Supplementary Fig. 1). The growth temperature was 1050 ^{0}C with flowing 400 sccm Ar carrier gas. Typical growth time was 10 min and the reaction was terminated by pulling the Nb source outside the hot furnace. The substrates were cooled down naturally to below 500 ^{0}C with keeping flowing sulfur vapors to suppress the sulfur vacancies[52].

Optical transmission imaging

Optical transmission images were taken with a light microscope (Nikon NI-U) equipped with a digital camera (Canon EOS 6D). In brief, we used white light LED source to illuminate NbS$_2$ samples from backside of sapphire substrate. Transmitted light was collected by an objective lens (100x/0.80NA) to form optical transmission images. A shortpass edge filter allowing < 575 nm wavelength light to pass through was inserted in the optical pathway to increase optical contrasts of ultrathin NbS$_2$.

AFM observations and Raman spectroscopy

AFM topological images were obtained by using an atomic force microscope (Bruker Dimension FastScan) operated in tapping mode with probe scanning rate of 1 ~ 10 Hz. Raw AFM images were analyzed with the WSxM 5.0[53]. We have measured Raman spectra by

confocal Raman microscope (Renishaw invia) with 532 nm laser as an excitation source. In all measurements, we used laser power of 0.225 mW (figure 4) to avoid possible laser-induced damages. The Raman signal collected and filtered with an objective lens (100x/0.85NA) and Notch filter was detected by a spectrometer equipped with charge-coupled device (CCD). The typical size of laser spot is around ~ 1 μm, which ensures that all Raman signals originate from individual NbS_2 domains.

Calculation of Γ phonon frequencies in 3R-NbS₂

Phonon frequencies in 3R-NbS₂ were calculated within the density functional perturbation theory[54,55]. We use the local-density approximation[56], the ultrasoft pseudopotentials[57], the plane-wave basis set with cutoff energies of 50 Ry for wavefunctions and 400 Ry for charge densities, and 12 x 12 x 4 grid of k-points. The unit cell and the atomic positions were fully relaxed and the obtained lattice parameters (a=3.274Å and c=17.529Å) agree well with the experiments.

Device fabrication and transport measurements

Standard electron-beam lithography (EBL) processing was carried out to fabricate devices used in this study. Electrode contacts consisting of Cr/Au (5nm/95nm) were made by vacuum evaporation. Prior to measurements, devices were annealed at 120 ^{0}C for ca. 20 hours in high vacuum (10^{-6} Torr) to improve the contact quality[58]. We also performed local in-situ heating in cryostat chamber to clean samples. Room temperature measurements were performed with a semiconductor parameter analyzer (Keithley Model 4200-SCS). Temperature dependence of resistivity was measured by using a current source (Keithley Model 6221) and a voltmeter (Keithley Model 2182A); delta mode measurements were used to remove the contribution from thermal electromotive force. The moving filter was used to improve signal-to-noise ratio.

Sample transfer for TEM characterizations

NbS$_2$ samples grown on hBN were transferred onto TEM-compatible grid by solution etching process (2M Sodium Hydroxide in hot water bath 90 ^{0}C)[32]. First, polystyrene (PS) (50 mg/mL in toluene) was spin-coated onto the target sapphire substrates (3000 rpm for 45 s). Then PS at the substrate edges was carefully removed to get the sapphire surface exposed. After the etching process (ca. 20 min in the hot base solution), the floating PS film was fished out and washed with distilled water several times before transferring it onto TEM-compatible copper grid. After that, TEM grid (with PS film) was heated at 115 ^{0}C in vacuum for 30 min to remove water. Then PS film was dissolve in toluene and heated at 120 ^{0}C for another 1 hour prior to the TEM observations.

3.7 Acknowledgements

3.8 References

1. Qin, S., Kim, J., Niu, Q. & Shih, C.K. Superconductivity at the two-dimensional limit. *Science* **324,** 1314-1317 (2009).

2. Zhang, T. *et al.* Superconductivity in one-atomic-layer metal films grown on Si(111). *Nature Phys.* **6,** 104-108 (2010).

3. Brun, C. *et al.* Remarkable effects of disorder on superconductivity of single atomic layers of lead on silicon. *Nature Phys.* **10,** 444-450 (2014).

4. Ge, J. *et al.* Superconductivity above 100 K in single-layer FeSe films on doped $SrTiO_3$. *Nature Mater.* **14,** 285-289 (2015).

5. Ye, J. *et al.* Superconducting dome in a gate-tuned band insulator. *Science* **338,** 1193-1196 (2012).

6. Yu, Y. *et al.* Gate-tunable phase transitions in thin flakes of $1T$-TaS_2. *Nature Nanotech.* **10,** 270-276 (2015).

7. Novoselov, K.S. *et al.* Two-dimensional atomic crystals. *Proc. Natl. Acad. Sci. U.S.A.* **30,** 10451–10453 (2005)

8. Benameur, M.M. *et al.* Visibility of dichalcogenide nanolayers. *Nanotechnology* **22,** 125706 (2011).

9. Yoshida, M. *et al.* Controlling charge-density-wave states in nano-thick crystals of $1T$-TaS_2. *Sci. Rep.* **4,** 7302 (2014).

10. Hajiyev, P., Cong, C.X., Qiu, C.Y. & Yu, T. Contrast and Raman spectroscopy study of single- and few-layered charge density wave material: $2H$-$TaSe_2$. *Sci. Rep.* **3,** 2593 (2013).

11. Mak, K.F. *et al.* Atomically thin MoS_2: A new direct-gap semiconductor. *Phys. Rev. Lett.* **105,** 136805 (2010).

12. Splendiani, A. *et al.* Emerging photoluminescence in monolayer MoS$_2$. *Nano Lett.* **10,** 1271-1275 (2010).

13. Ruppert, C., Aslan, O.B. & Heinz, T.F. Optical properties and band gap of single-and few-layer MoTe$_2$ crystals. *Nano Lett.* **14,** 6231-6236 (2014).

14. Gorbachev, R.V. *et al.* Hunting for monolayer boron nitride: Optical and Raman signatures. *Small* **7,** 465-468 (2011).

15. Castellanos-Gomez, A. *et al.* Isolation and characterization of few-layer black phosphorus. *2D Materials* **1,** 025001 (2014)

16. Li, X. *et al.* Large-area synthesis of high-quality and uniform graphene films on copper foils. *Science* **324,** 1312-1314 (2009).

17. Kim, K.K. *et al.* Synthesis of monolayer hexagonal boron nitride on Cu foil using chemical vapor deposition. *Nano Lett.* **12,** 161-166 (2012).

18. Ji, Q., Zhang, Y., Zhang, Y. & Liu, Z. Chemical vapour deposition of group-VIB metal dichalcogenide monolayers: engineered substrates from amorphous to single crystalline. *Chem. Soc. Rev.* **44,** 2587-2602 (2015)

19. Shi, Y., Li, H. & Li, L.-J. Recent advances in controlled synthesis of two-dimensional transition metal dichalcogenides via vapour deposition techniques *Chem. Soc. Rev.* **44,** 2744-2756 (2015)

20. Xu, S. *et al.* van der Waals epitaxial growth of atomically thin Bi$_2$Se$_3$ and thickness-dependent topological phase transition. *Nano Lett.* **15,** 2645-2651 (2015).

21. Gong, Y. *et al.* Vertical and in-plane heterostructures from WS$_2$/MoS$_2$ monolayers. *Nature Mater.* **13,** 1135-1142 (2014).

22. Duan, X. *et al.* Lateral epitaxial growth of two-dimensional layered semiconductor heterojunctions. *Nature Nanotech.* **9,** 1024-1030 (2014).

23. Lee, Y.-H. *et al.* Synthesis of large-area MoS_2 atomic layers with chemical vapor deposition. *Adv. Mater.* **24,** 2320-2325 (2012).

24. Zhang, Y. *et al.* Controlled growth of high-quality monolayer WS_2 layers on sapphire and imaging its grain boundary. *ACS Nano* **7,** 8963-8971 (2013).

25. Ge, W., Kawahara, K., Tsuji, M. & Ago, H. Large-scale synthesis of NbS_2 nanosheets with controlled orientation on graphene by ambient pressure CVD. *Nanoscale* **5,** 5773-5778 (2013).

26. Wilson, J.A. & Yoffe, A.D. Transition metal dichalcogenides discussion and interpretation of observed optical, electrical and structural properties. *Adv. Phys.* **18,** 193-& (1969).

27. Guillamon, I. *et al.* Superconducting density of states and vortex cores of 2H-NbS_2. *Phys. Rev. Lett.* **101,** 166407 (2008).

28. Dean, C.R. *et al.* Boron nitride substrates for high-quality graphene electronics. *Nature Nanotech.* **5,** 722-726 (2010).

29. Cui, X. *et al.* Multi-terminal transport measurements of MoS_2using a van der Waals heterostructure device platform. *Nature Nanotech.* (2015) doi:10.1038/nnano.2015.70.

30. Doganov, A.R. *et al.* Transport properties of pristine few-layer black phosphorus by van der Waals passivation in an inert atmosphere. *Nature Commun.* **6,** 6647 (2015)

31. Wood, J.D. *et al.* Effective passivation of exfoliated black phosphorus transistors against ambient degradation. *Nano Lett.* **14,** 6964-6970 (2014).

32. Xu, Z. Q. *et al.* Synthesis and transfer of large-area monolayer WS_2 crystals: Moving toward the recyclable use of sapphire substrates. *ACS Nano* **9,** 6178-6187 (2015).

33. Beal, A.R., Hughes, H.P. & Liang, W.Y. Reflectivity spectra of some group VA transition-metal dichalcogenides. *J. Phys. C.* **8,** 4236-4248 (1975).

34. Beal, A.R. & Hughes, H.P. Kramers-Kronig analysis of the reflectivity spectra of 2H-MoS_2, 2H-$MoSe_2$ and 2H-$MoTe_2$. *J. Phys. C.* **12,** 881-890 (1979).

35. Bernardi, M., Palummo, M. & Grossman, J.C. Extraordinary sunlight absorption and one nanometer thick photovoltaics using two-dimensional monolayer materials. *Nano Lett.* **13,** 3664-3670 (2013).

36. Bachmann, R., Kirsch, H.C., and Geballe, T.H. Optical properties and superconductivity of $NbSe_2$. *Solid State Commun.* **9,** 57-60 (1971).

37. McMullan, W.G. & Irwin, J.C. Raman-scattering from 2H-NbS_2 and 3R-NbS_2. *Solid State Commun.* **45,** 557-560 (1983).

38. Lee, C. *et al.* Anomalous lattice vibrations of single- and few-layer MoS_2. *ACS Nano* **4,** 2695-2700 (2010).

39. Berkdemir, A. *et al.* Identification of individual and few layers of WS_2 using Raman spectroscopy. *Sci. Rep.* **3,** 1755 (2013).

40. Molina-Sanchez, A. & Wirtz, L. Phonons in single-layer and few-layer MoS_2 and WS_2. *Phys. Rev. B* **84,** 155413 (2011).

41. Ayers, J.E. Heteroepitaxy of Semiconductors: Theory, Growth, and Characterization. CRC Press (2007)

42. Yang, W. *et al.* Epitaxial growth of single-domain graphene on hexagonal boron nitride. *Nature Mater.* **12,** 792-797 (2013).

43. Okada, M. *et al.* Direct chemical vapor deposition growth of WS_2 atomic layers on hexagonal boron nitride. *ACS Nano* **8,** 8273-8277 (2014).

44. Staley, N.E. *et al.* Electric field effect on superconductivity in atomically thin flakes of $NbSe_2$. *Phys. Rev. B* **80,** 184505 (2009).

45. Kuc, A., Zibouche, N. & Heine, T. Influence of quantum confinement on the electronic structure of the transition metal sulfide TS_2. *Phys. Rev. B* **83,** 155413 (2011).

46. Huang, Y. *et al.* Transport properties in semiconducting NbS_2 nanoflakes. *Appl. Phys. Lett.* *105,* 093106 (2014).

47. Niazi, A. & Rastogi, A.K. Low-temperature resistance minimum in non-superconducting $3R-Nb_{1+x}S_2$ and $3R-Ga_xNbS_2$. *J. Phys.: Condens. Matter* *13,* 6787-6796 (2001).

48. Hu, J. *et al.* Enhanced electron coherence in atomically thin Nb_3SiTe_6. *Nature Phys.* (2015) doi:10.1038/nphys3321

49. Andrei, N., Furuya, K. & Lowenstein, J. H. Solution of the Kondo problem. *Rev. Mod. Phys.* *55,* 331-402 (1983).

50. Lee, P. A. & Ramakrishnan, T. V. Disordered electronic systems. *Rev. Mod. Phys.* *57,* 287-337 (1985).

51. Taniguchi, T. & Watanabe, K. Synthesis of high-purity boron nitride single crystals under high pressure by using Ba-BN solvent. *J. Crystal Growth* *303,* 525-529 (2007).

52. Ji, Q. *et al.* Epitaxial monolayer MoS_2 on mica with novel photoluminescence. *Nano Lett.* *13,* 3870-3877 (2013).

53. Horcas, I. *et al.* Wsxm: A software for scanning probe microscopy and a tool for nanotechnology. *Rev. Sci. Instrum.* *78,* 013705 (2007).

54. Baroni, S., de Gironcoli, S., dal Corso, A. & Giannozzi, P. Phonons and related crystal properties from density-functional perturbation theory. *Rev. of Mod. Phys.,* *73,* 515 (2001).

55. Giannozzi, P. *et al.* QUANTUM ESPRESSO: A modular and open-source software project for quantum simulations of materials. *J. Phys.: Condens. Matter* *21,* 395502 (2009).

56. Perdew, J. P., & Zunger, A. Self-interaction correction to density-functional approximations for many-electron systems. *Phys. Rev. B,* *23,* 5048 (1981).

57. Vanderbilt, D. Soft self-consistent pseudopotentials in a generalized eigenvalue formalism. *Phys. Rev. B*, *41,* 7892 (1990).

58. Ovchinnikov, D. *et al.* Electrical transport properties of single-layer WS$_2$. *ACS Nano* *8,* 8174-8181 (2014).

Chapter 4 | Preparation for measurement of valley transport in transition metal dichalcogenide monolayers

4.1 Introduction to valley transport in TMDCs

4.1.1 Physics of valley transport in individual TMDC monolayers

TMDC monolayers (*e.g.*, MoS$_2$, WS$_2$, MoSe$_2$, and WSe$_2$) provide a new medium for studying the interplay between different degrees of freedom for carrier transport because information pertaining to coupled spin and valley indices can be obtained. Accordingly, there is now considerable research interest for studying spintronics and valleytronics applicable to the 2D limit[1]. Following the group point of view, valley-contrasting physics at Brillouin zone (BZ) corners K and −K, such as the circularly polarized optical selection rule[2-3] and valley-contrasting Berry curvature[4-5], emerge owing to the inversion symmetry breaking in the TMDC monolayers. Physically observable quantities $\boldsymbol{\Omega}$ (Berry curvature and orbital magnetic moment) in K and −K valleys are transformed by time reversal symmetry (TRS) such that

$$\boldsymbol{\Omega}\,(K)\;=\;-\boldsymbol{\Omega}\,(-K)\;(\textbf{Eq. 1}).$$

If spatial inversion symmetry is preserved in these crystals, then

$$\boldsymbol{\Omega}\,(\mathrm{K})\;=\;\boldsymbol{\Omega}\,(-K)\;(\textbf{Eq. 2})$$

holds true, indicating that

$$\boldsymbol{\Omega}\,(K)=\;\boldsymbol{\Omega}\,(-K)=0\;(\textbf{Eq. 3}).$$

Therefore, inversion symmetry breaking is a required condition for the emergence of valley-related physics, in which case, $\boldsymbol{\Omega}$ in K and −K can assume finite values with opposite signs.

Figure 1a shows the calculated Berry curvature, which can be naively regarded as an effective magnetic field defined in k-space perpendicular to the monolayer plane, over the

entire first BZ for TMDC monolayers[4]. The calculation revealed equal magnitude but opposite
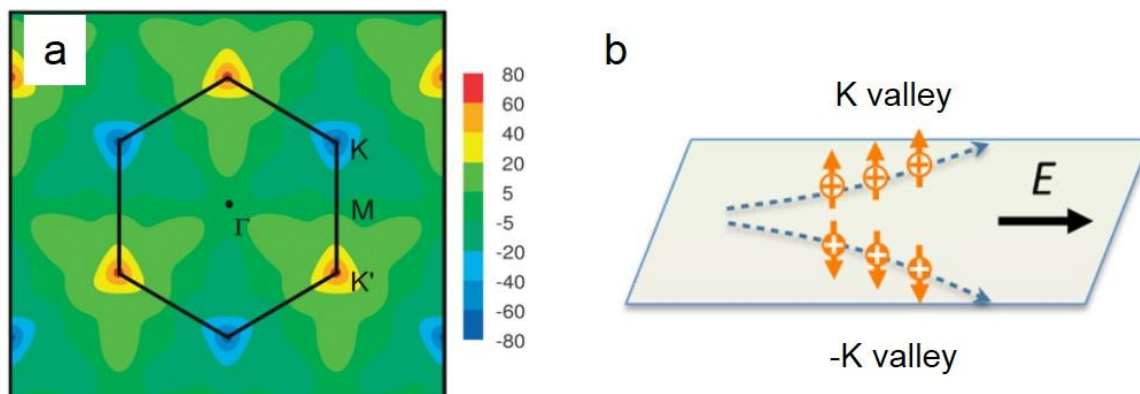
Figure 1. (a) Calculated Berry curvature over the whole first BZ for a monolayer TMDC (adapted from ref. 4). The calculated Berry curvature (or effective magnetic field) at K and −K valleys is same in magnitude but opposite in sign, giving rise to the valley-contrasting transport properties. (b) Illustration of VHE in the hole-doped monolayer TMDC (adapted from ref.6). Holes from K and −K are endowed with velocities, driven by Berry curvature, in opposite directions that are perpendicular to the applied E field.

sign Berry curvature for K and −K valleys. Because of the reverse Berry curvature (opposite effective magnetic fields), in the presence of an in-plane electrical field, carriers in different valleys will be endowed with opposite "anomalous" velocities that are perpendicular to the applied electrical (E) field as indicated in

$$v_\perp \ = \ \frac{e}{\hbar} E \ \times \ \boldsymbol{\Omega} \ (k) \ (\textbf{Eq. 4}),$$

where e is the electric charge and $\hbar$ is the reduced Planck's constant. This outcome gives rise to the valley-Hall effect (VHE) in these systems[6]. **Figure 1b** shows a schematic of VHE in hole-doped systems, in which holes at different valleys move and accumulate at opposite edges in monolayer crystals.

Figure 2 shows the first report of experimental observation of the predicted VHE in a model MoS$_2$ monolayer device prepared by mechanical exfoliation[7]. The MoS$_2$ monolayer sample was excited by a circularly polarized 1.9 eV laser to selectively generate photoexcited electron–hole pairs from one specific valley (K or −K). Because so-generated electrons and holes possess charges that are opposite in sign, the Berry curvature drives them to opposite

directions with a perpendicular velocity relative to the applied $\boldsymbol{E}$ field. Consequently, a voltage
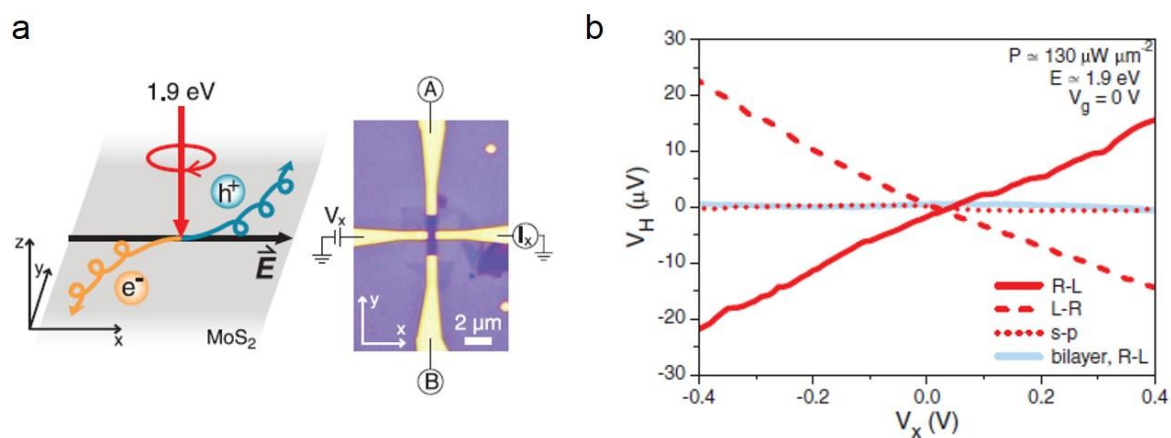
Figure 2. Experimental demonstration of VHE (ref.7). (a) Optical excitation and electrical detection of VHE for a monolayer MoS_2 device. (b) Hall voltage as a function of a voltage bias that is applied perpendicularly. Red dot line shows the result for a monolayer samples excited by a linearly polarized laser, and blue line show that for a bilayer sample excited by a circularly polarized laser. In both cases, zero Hall voltage was observed. The solid and dashed red lines show results for a monolayer sample excited by circularly polarized laser with opposite handness.

drop (V_H) is expected to be measured between probes A and B. **Figure 2b** shows the measured Hall voltage as a function of the applied $\boldsymbol{E}$ field (potential difference). With either left-handed or right-handed circularly polarized light excitation, the Hall voltage shows a linear dependence to the applied $\boldsymbol{E}$ field, demonstrating the VHE in the monolayer MoS_2 sample. However, both linearly polarized light excitation on the monolayer sample and circularly polarized light excitation on a bilayer sample show zero Hall voltage as control experiments.

4.1.2 TMDC monolayer heterostructures

Stacking different TMDC monolayers together as schematically shown in **Figure 3a** causes interesting phenomena to occur in TMDC heterostructures. These monolayers will generally form type-II band alignment as shown in **Figure 3a**, which illustrates model monolayer WX_2 and MoX_2 systems (MoX_2/WX_2)[8-10]. In this type of band alignment, photoexcited electrons or holes at band edges will transfer from one layer to the other, thereby

forming the charge transfer (CT) excitons or interlayer excitons. This charge separation process is extremely fast, with a time constant of ~150 fs; moreover, it is much shorter than that of a pristine exciton life time[8]. These interlayer excitons are bright (**Figure 3b**) and have been observed to have very long lifetimes on the scale of nanoseconds[9].
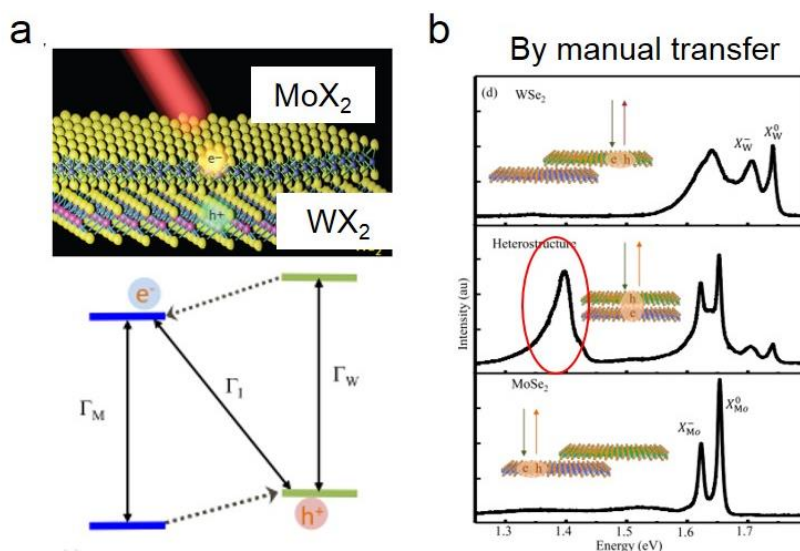
Figure 3. (a) Interlayer exactions formed in the TMDC monolayer heterostructures (MoX_2/WX_2) with a type II band alignment (adapted from ref. 8). The process of the charge separation is extremely fast ~150 fs. (b) Interlayer exciton in the PL spectrum (indicated by the red circle) in $MoSe_2$/WSe_2 heterostructures that are prepared by manual transfer of each monolayers (adapted from ref. 9).

More investigations are needed to demonstrate valley injection and valley transport in TMDC heterostructures (see an example in **Figure 4**)[10-12]. To date, studies have been limited to TMDC heterostructures that are manually stacked, which results in a random crystalline orientation between the two layers; this lack of orientation control hampers the observation and detection of valley injection and transport in TMDC heterostructures. We propose a direct bottom-up synthesis of TMDC heterostructures in which the orientation are expected to be controlled via epitaxial growth mechanism. We are currently using a newly introduced molecular beam epitaxy (MBE) apparatus to control the growth of TMDC heterostructures (apparatus shown in **Figure 5**). The precise control of the metal and chalcogen atom supply
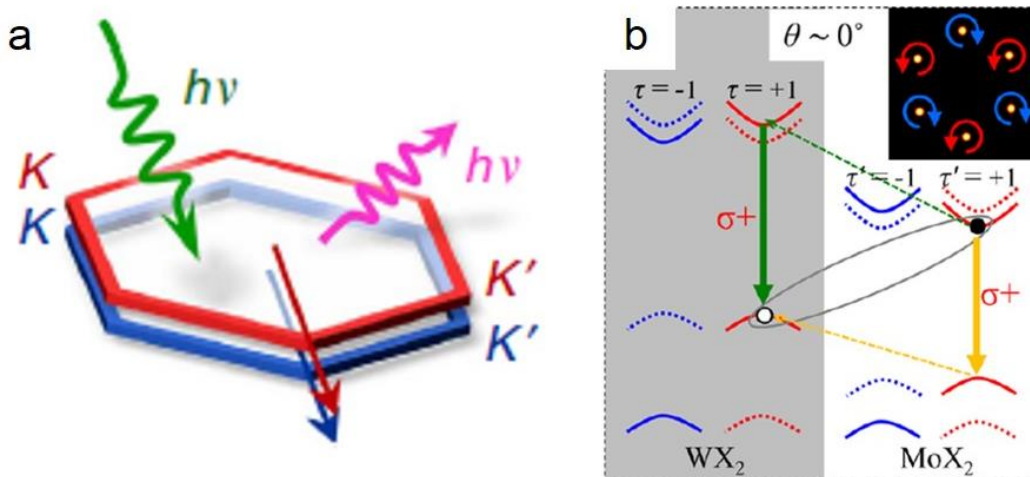
Figure 4. Valley-polarized interlayer excitons that are expected and predicted in crystallographic orientation-matched TMDC monolayer heterostructures (MoX_2/WX_2). (a) is adapted from ref. 10, and (b) is adapted from ref. 11.

should lead to the successful growth of TMDC heterostructures with high crystalline quality

and matching orientations.
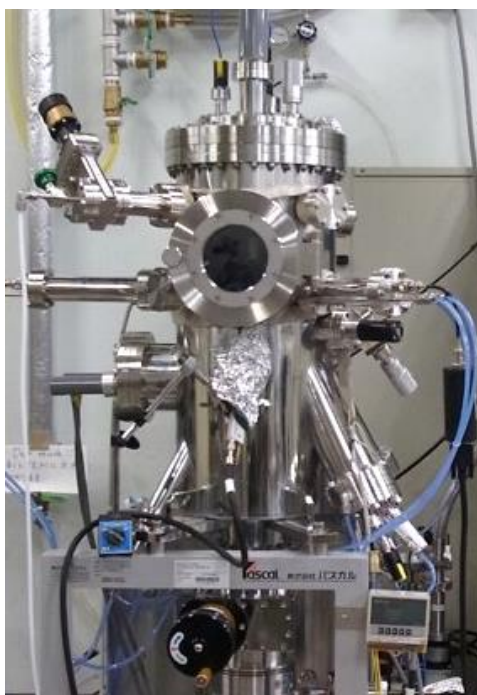
Figure 5. A photo of MBE set-up that is newly introduced for the growth of TMDC monolayer heterostructures.

4.2 Experimental

Figure 6. A set of photos displaying the instrumental set-up used in the measurement of valley transport.

A set of photos displaying the instrumental set-up used in the measurement of valley transport is shown in **Figure 6**. Briefly, the set-up is composed of an illumination system (633 nm circularly polarized laser), an electrical measuring system (lock-in amplifier), a cryostat sample stage, and pumping and cooling systems. This set-up enables us to measure the valley transport in monolayer TMDCs and TMDC heterostructures at liquid N_2 temperature with circularly polarized laser excitation.

A schematic of optical excitation and electrical signal detection is shown in **Figure 7**. A continuous wave single-frequency laser (633 nm) passes a mechanical chopper running at a specified frequency (for example, ~10 kHz). The light is vertically linearly polarized after passing it through the polarizer and half-plate. Then, a quarter-plate is combined with the half-
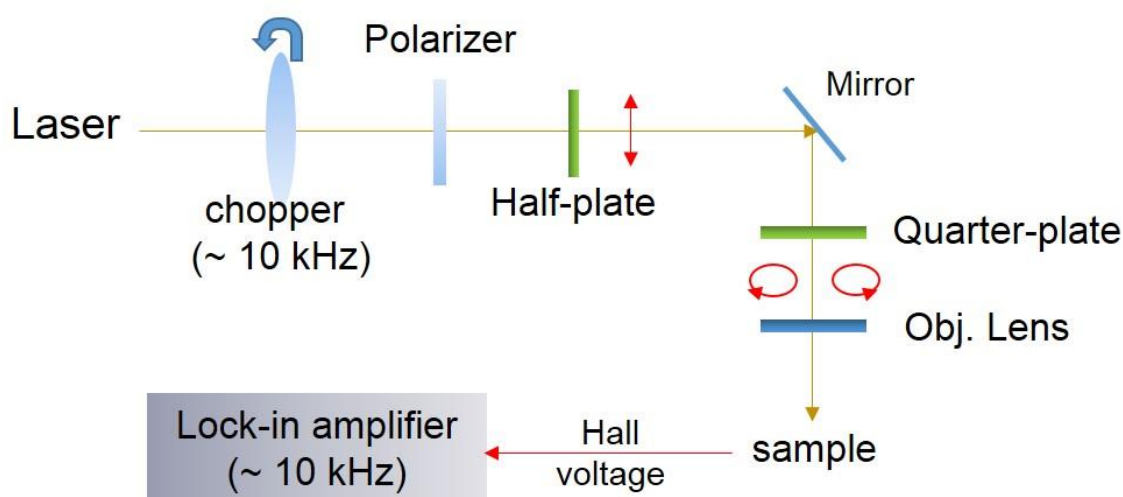
Figure 7. Schematic representation for the optical excitation and electrical signal detection used in the measurement of valley transport.

plate to change the linearly polarized light to circularly polarized light (left-handed or right-handed). The circularly polarized light is subsequently focused onto samples by an objective lens. The resultant electrical signal occurring upon laser excitation (~10 kHz) is selectively detected and measured using a lock-in amplifier.
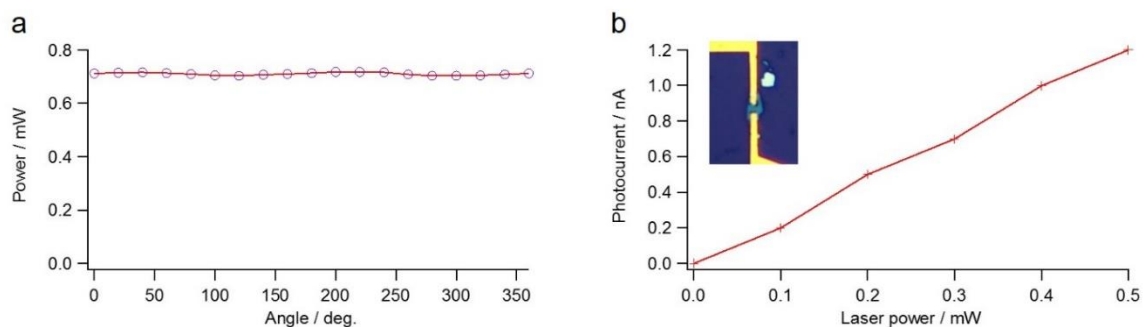
Figure 8. (a) Examination of purity of circularly polarized light. The nearly constant power output with changing the direction of a polarizer indicates high purity of circularly polarized light. (b) Linear response of photocurrent with increasing laser power for a multilayer MoS_2 device. All these test experiments demonstrated that our prepared set-up can properly excite materials with high purity of circularly polarized laser light, and can correctly detect the electrical signals.

Prior to each measurement, the purity of the generated circular polarization was examined. One of the typical results is shown in **Figure 8a**. Nearly constant light power upon the rotation of a polarizer placed in front of a power meter clearly showed that our optical set-

up is able to excite samples with high purity circularly polarized laser light. **Figure 8b** shows a photocurrent measurement of a thin multi-layer MoS$_2$ device prepared by mechanical exfoliation. The linear response of photocurrent upon the increase of laser excitation power indicates that our instrumental set-up can correctly measure the electrical signal.

4.3 Progress and results

Preliminary results were obtained after we confirmed that the set-up could correctly measure the electrical signal output. **Figure 9a** shows the photoluminescence (PL) microscopy image (obtained by a digital camera without a spectrometer) of thin-layered MoS2 synthesized on hBN by CVD (Courtesy of Mr. Yusuke Kureishi, an M1 student in Professor Shinohara's research group). By determining the PL strength, we were able to roughly examine the presence of monolayer samples and their formation quality on a micrometer size scale, thereby offering a rapid and noninvasive optical method to determine high-quality monolayer samples for further device processing. For example, the bright sample indicated by a white arrow in **Figure 9a** was examined by AFM as shown in **Figures 9b** and **9c**. AFM images confirmed that this sample was monolayer and had a very clean surface. Suitable monolayer samples
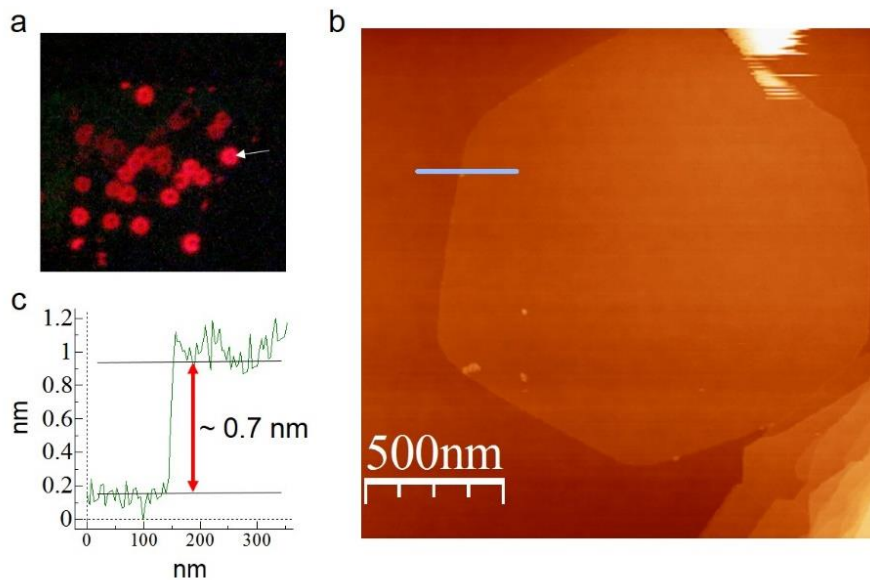
Figure 9. (a) PL microscopy image of CVD-synthezied monolayer MoS_2 grown on hBN. The arrow indicates a monolayer sample shown in (b). (b) AFM image of a monolayer MoS_2 sample indicated by the white arrow shown in (a). (c) Height profile of the monolayer MoS_2 along the line in (b).

were identified by utilizing this developed PL imaging technique, and electron beam lithography (EBL) was used for micro-sized device fabrication.
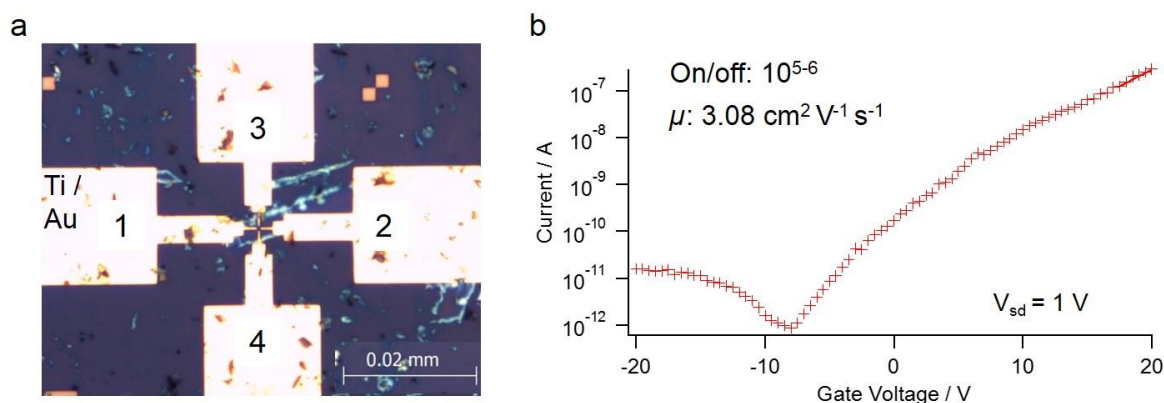
Figure 10. (a) Optical image of a CVD-syntehsized monolayer MoS_2 device compatible with Hall measurement. (b) Electrical characteristics (transfer curve) for the same device shown in (a); data are collected from measurement via probes 1-2 at room temperature. Carrier mobility, μ, at the electron side (positive gate voltage) is estimated to be 3.08 cm^2 V^{-1} s^{-1}, and the on/off ratio is about 10^5–10^6, which are reasonable results for a two-probe measurement geometry.

We prepared CVD-synthesized MoS_2 monolayer devices for valley-Hall experiments by combining PL imaging and EBL techniques. One of the devices is shown in **Figure 10a**, and its electrical characteristics (transfer curve) are shown in **Figure 10b**. The on/off ratio of this CVD-synthesized MoS_2 device is about 10^5–10^6 and the calculated mobility, μ, is about 3.08 cm^2 V^{-1} s^{-1} (data were measured using 1-2 probes). These were not considered to be poor measurements once the effect of contact resistance from the two-probe measurement geometry was considered.

The same sample was used for the valley-Hall measurement; it was excited by a 633 nm laser with high-purity circular polarization. A constant current was passed through 3-4 probes, while the ~10 kHz voltage signal (if any) between 1-2 probes was monitored by a lock-in amplifier as displayed in the inset of **Figure 11a. Figure 11a** shows the measured Hall voltage as a function of loading current. The linear response of the measured voltage is consistent with the relationship of the valley carriers' velocity with the applied *E* field (loading

current) as described in **Eq. 4**. **Figure 11b** shows the laser power-dependent Hall voltage. When the power of the excitation laser increased, the concentration of photoexcited carriers also increased, leading to increased Hall voltage. When we decreased the polarization degree of circularly polarized light, we observed a decrease in the Hall voltage, which is consistent with the prediction and expectation of the VHE. However, our samples had thick MoS_2 layers surrounding the edges of the underlying hBN substrate; this could have contributed to the measured Hall voltage and possibly explains the large Hall voltage in addition to the background voltage (non-zero voltage when extrapolating to the zero power in **Figure 11a**). Future work includes conducting the valley Hall transport measurements for the isolated CVD-synthesized MoS_2, WS_2 samples, and TMDCs heterostructures with matching orientations.
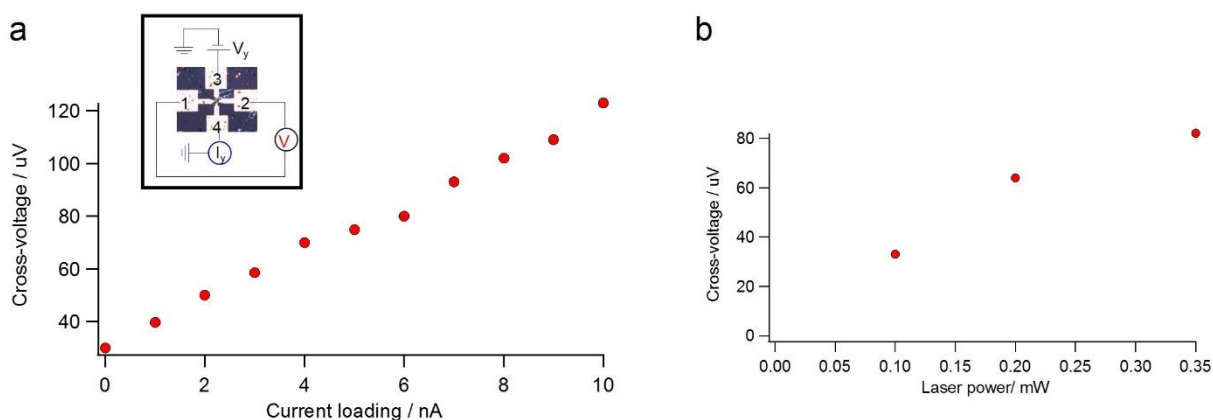
Figure 11. Valley-Hall measurement for a CVD-synthesized monolayer MoS_2. (a) Linear dependence of Hall voltage on current flowing through 3-4 probes. The inset displays the electrical measurement geometry. (b) Dependence of Hall voltage on the excitation laser power.

4.4 References

1. Xu, X. D., Yao, W., Xiao, D., and Heinz, T. F. Spin and pseudospins in layered transition metal dichalcogenides. *Nature Phys.* **10,** 343-350 (2014).

2. Zeng, H. L. *et al*. Valley polarization in MoS_2 monolayers by optical pumping. *Nature Nanotech.* **7,** 490-493 (2012).

3. Mak, K. F., He, K. L., Shan, J., and Heinz, T. F. Control of valley polarization in monolayer MoS_2 by optical helicity. *Nature Nanotech.* **7,** 494-498 (2012).

4. Feng, W. X. *et al*. Intrinsic spin Hall effect in monolayers of group-VI dichalcogenides: A first-principles study. *Phys. Rev. B* **86,** (2012).

5. Xiao, D., Chang, M. C., and Niu, Q. Berry phase effects on electronic properties. *Rev. Mod. Phys.* **82,** 1959-2007 (2010).

6. Xiao, D. *et al*. Coupled spin and valley physics in monolayers of MoS_2 and other group-VI dichalcogenides. *Phys. Rev. Lett.* **108,** (2012).

7. Mak, K. F., McGill, K. L., Park, J., and McEuen, P. L. The valley Hall effect in MoS_2 transistors. *Science* **344,** 1489-1492 (2014).

8. Hong, X. P. *et al*. Ultrafast charge transfer in atomically thin MoS_2/WS_2 heterostructures. *Nature Nanotech.* **9,** 682-686 (2014).

9. Rivera, P. *et al*. Observation of long-lived interlayer excitons in monolayer $MoSe_2$-WSe_2 heterostructures. *Nat. Commun.* **6,** (2015).

10. Heo, H. *et al*. Rotation-misfit-free heteroepitaxial stacking and stitching growth of hexagonal transition-metal dichalcogenide monolayers by nucleation kinetics controls. *Adv. Mater.* **27,** 3803-3810 (2015).

11. Yu, H. Y., Wang, Y., Tong, Q. J. and Xu, X. D. Anomalous light cones and valley optical selection rules of interlayer excitons in twisted heterobilayers. arXiv:1504.01215

12. Xia, F. N. *et al*. Two-dimensional material nanophotonics. *Nature Photon.* **8,** 899-907

(2014).